

C.1

GEODETIC STRAIN MEASUREMENTS  
IN CENTRAL VANCOUVER ISLAND

By

MICHAEL LISOWSKI

B.A., The University of California at Berkeley, 1972

A THESIS SUBMITTED IN PARTIAL FULFILLMENT OF  
THE REQUIREMENTS FOR THE DEGREE OF  
MASTER OF SCIENCE

in

THE FACULTY OF GRADUATE STUDIES

Department of Geological Sciences

We accept this thesis as conforming  
to the required standard

THE UNIVERSITY OF BRITISH COLUMBIA

October 1985

©Michael Lisowski, 1985

In presenting this thesis in partial fulfilment of the requirements for an advanced degree at the University of British Columbia, I agree that the Library shall make it freely available for reference and study. I further agree that permission for extensive copying of this thesis for scholarly purposes may be granted by the head of my department or by his or her representatives. It is understood that copying or publication of this thesis for financial gain shall not be allowed without my written permission.

Department of Geology

The University of British Columbia  
1956 Main Mall  
Vancouver, Canada  
V6T 1Y3

Date March 09, 1986

## Abstract

A 1982 trilateration network and a 1947 triangulation network located in central Vancouver Island were studied to determine measurement precision and horizontal strain accumulation. The 1982 trilateration network was comprised of 23 distance measurements (average length 24 km), which covered a 30 km by 50 km area near the town of Gold River, east of Nootka Sound. Atmospheric refractivity corrections to the Rangemaster III measured distances were derived from end-point air pressures and aircraft-flown temperature and humidity profiles taken at the time of rangings. The standard error in a distance  $L$  (m) was estimated to be  $\sigma = (a^2 + b^2 L^2)^{1/2}$ ; where  $a = 0.0057\text{m}$  and  $b = 0.2 \times 10^{-6}$  for distances reduced using the USGS probe temperatures and humidities or  $b \approx 0.26 \times 10^{-6}$  using the CGS probe. There were 54 angle measurements common to the 1947 and 1982 networks. The standard error in a 1947 angle measurement was  $2.3''$ , and the estimated standard error in a 1947 to 1982 angle change was  $2.4''$ . Assuming uniform strain, the average rate of shear strain accumulation between 1947 to 1982 was  $0.23 \pm 0.12 \mu\text{rad/yr}$  with the axis of maximum contraction bearing  $N56^\circ E \pm 12^\circ$ . The accumulation of strain in the Gold River area was found to be similar in orientation and average rate to that observed in western Washington. The northeast orientation of the maximum compressive strain found in the geodetic networks could be reproduced with a two-dimensional, elastic dislocation model of the Cascadia subduction zone by locking the shallow interface to a depth of about 20 km. The model could not account for some details of the vertical deformation and it was not consistent with the north-south compressive stress indicated by shallow earthquake focal mechanisms. Although the possibility of a large, shallow, thrust earthquake is inferred from the strain data, the uncertainty in the strain accumulation and the tectonic complexity of the area make such a conclusion speculative.

## TABLE OF CONTENTS

1. Introduction . . . . .	1
1.1. Historic earthquakes and present tectonic setting . . . . .	2
1.2. Contemporary Surface Deformation . . . . .	7
2. The 1982 Gold River Trilateration Survey . . . . .	10
2.1. The 1982 Measurements . . . . .	10
2.2. Instruments and Procedures . . . . .	16
2.2.1. Distance meter . . . . .	16
2.2.1.1. Modulation frequency stability . . . . .	16
2.2.1.2. Pointing error . . . . .	17
2.2.1.6. Zero error . . . . .	18
2.2.1.6. Cyclic error . . . . .	18
2.2.1.7. Receiver noise . . . . .	19
2.2.1.7. Return signal strength . . . . .	19
2.2.1.7. Instrument constant for Rangemaster III # 8016 . . . . .	19
2.3. Aircraft Probes . . . . .	22
2.3.1. Temperature measurements in fast airflows . . . . .	24
2.3.3. Physical description of the probes . . . . .	27
2.3.3. Averages from temperature-humidity profiles . . . . .	28
2.3.4. Static calibrations . . . . .	31
2.3.5. Dynamic air temperature tests . . . . .	34
2.4. Pressure . . . . .	37
2.5. The Accuracy and Precision of a Distance . . . . .	40
2.5.2. Constant error . . . . .	41
2.5.2. Scale error . . . . .	41

2.6. Recommendations . . . . .	43
2.6.1. Distance meter . . . . .	43
2.6.2. Probes . . . . .	44
2.7.0. Pressure . . . . .	45
2.7. Strain Resolution . . . . .	46
3. 1947 Triangulation . . . . .	48
4. Horizontal Deformation in the Gold River Network . . . . .	57
4.1. Calculation of shear strain from angle changes . . . . .	58
4.2. Shear strain accumulation between 1947 and 1982 . . . . .	60
5. Surface Deformation from Subduction Zone Models . . . . .	69
5.1. Subduction zone geometry . . . . .	72
5.2. Subduction Models . . . . .	75
6. Summary of Conclusions . . . . .	83
References . . . . .	86
Appendix A. General Theory of EDM measurements . . . . .	91
Appendix B. Calculation of the Average Index of Refraction . . . . .	95

## **Acknowledgements**

I thank Bill Slawson of U.B.C. and Herb Draggert of P.G.C. for their help throughout this project and for the opportunity to study the the neo-tectonics of Vancouver Island. George Houston, Byron Bresee, and Robert Duval of the Canadian Geodetic Survey deserve recognition for their careful survey measurements and cooperation in providing field notes and test data. Jim Savage and Will Prescott of the U.S.G.S. provided instrumentation, advice, and analysis programs and allowed me to take two years of leave from my work with the Crustal Strain project to attend U.B.C. Nancy King and Karen Wendt of the U.S.G.S. helped with the processing of the field measurements. This research was supported by a grant from the Department of Energy, Mines, and Resources.

## 1. INTRODUCTION

Repeated geodetic surveys reveal the contemporary surface deformation in tectonically active areas. The sense, rate, and spatial distribution of the movements define the regional deformation pattern. Together with studies of seismicity and regional tectonics, surface deformation studies can aid in the assessment of seismic risk [Thatcher, 1981].

The cyclic pattern of strain accumulation and release around active faults was first documented by Reid [1910] on the basis repeated triangulation surveys around the rupture zone of the 1906 San Francisco earthquake. Studies since that time have shown that the “ultimate strain” drop during large earthquakes averages around 50  $\mu$ strain (ppm) with values occasionally as large as 180  $\mu$ strain [Rikitake, 1982]. These large coseismic strain changes are easily detected with standard geodetic surveys, which can obtain a strain resolution of about 2  $\mu$ strain. Interseismic deformation, which appears to average between 0.1 and 0.6  $\mu$ strain/yr [Savage, 1983; Nakana, 1973], is more difficult to measure. A period of a decade or more is often required for strain to accumulate to a level that can be measured with standard geodetic techniques.

The measurement of horizontal and vertical deformation require distinctly different techniques and instrumentation. Studies of vertical deformation rely on spirit leveling and tide gauge records, measurement systems that have changed very little in the past century. Since about 1970 trilateration has supplanted triangulation for measurements of horizontal deformation. Using special techniques, trilateration can obtain measurement precision about 10 times greater than triangulation, allowing a strain resolution of about 0.2  $\mu$ strain. In addition, the distance changes between repeated surveys provide both extensional and shear strain accumulation, whereas angle changes only determine the shear strain accumulation.

This thesis documents the first high-precision trilateration survey made in western

Canada, the 1982 survey of the Gold River network in central Vancouver Island (see Figure 1.1). The observations and measurement system are discussed in Chapter 2. The distances measured during the 1982 survey provide the baseline for comparison with future surveys and the discussion is focused on possible errors in the measurements. In the third chapter a 1947 triangulation survey is analyzed. Strain accumulation calculated from angles changes between 1947 and 1982 is given in the fourth chapter, deformation models are discussed in the fifth chapter, and the conclusions are summarized in the sixth chapter. Future surveys of the Gold River network may aid in unraveling the tectonic interactions in this complex and seismically active area.

## 1.1. HISTORIC EARTHQUAKES AND PRESENT TECTONIC SETTING

The region around the Gold River network in central Vancouver Island has experienced one moderate (1957  $M=6.0$  [*Tobin and Sykes*, 1968]) and two large (1918  $M=7.0$  [*Gutenberg and Richter*, 1954]; 1946  $M=7.3$  [*Rogers and Hasegawa*, 1978]) earthquakes (Figure 1.2). No surface rupture was reported for any of these events, even though all are believed to have focal depths of 30 km or less. The nodal planes from the focal mechanism solutions for the 1946 and 1957 events are not uniquely defined: the preferred solutions show predominately strike slip faulting with either dextral slip on a northwest striking plane or sinistral slip on a northeast striking plane, with the northwest plane preferred; the alternative solutions indicate a large component of normal faulting [*Rogers*, 1979]. A 1978 resurvey of a 1935 triangulation network around the epicentral area of the 1946 event shows angle changes that are best fit by oblique normal slip across the northwest trending Beaufort Range fault, although pure right-lateral slip is not excluded at the 90% confidence limit [*Slawson and Savage*, 1979]. Coseismic elevation changes derived from spirit level surveys adjacent to the epicenter show subsidence of about 10 cm over a broad area, a deformation pattern that is not typical of strike-slip faulting (see *Chinnery* [1961])



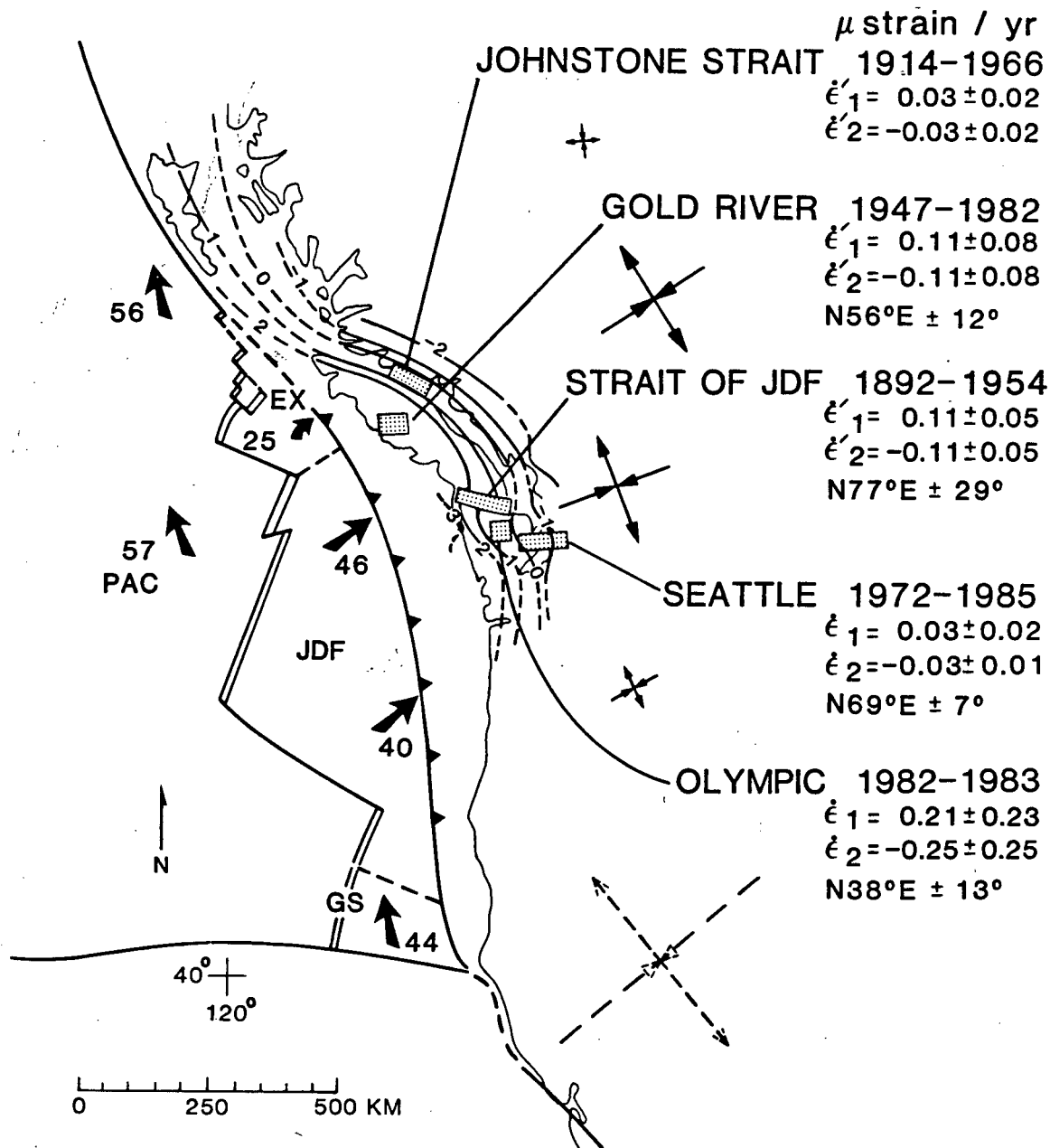


**Figure 1.1.** Map of the northwestern United States and southwestern Canada showing the tectonic setting, average rates of horizontal strain accumulation, and contemporary uplift rate contours. Velocity vectors in mm/yr relative to the North America plate are shown by the arrows on the Pacific (PAC), Explorer (EX), Juan de Fuca (JDF), and Gorda South (GS) plates [Riddihough, 1984]. The curved convergence vector on the Explorer plate indicates a nearby pole of rotation. Average uplift rate contours in mm/yr are from Ando and Balazs [1979] and Riddihough [1982]. Principal strain rates ( $\dot{\epsilon}_1, \dot{\epsilon}_2$ ; where  $\dot{\epsilon}_1$  is the maximum extensional strain) and principal deviatoric strain rates ( $\dot{\epsilon}'_1, \dot{\epsilon}'_2$ ) are in  $\mu$ strain/yr. The strain rates and their uncertainty ( $\pm 1\sigma$ ) are shown below the network name and are an average value for the indicated period within the area shown in the stippled box. The direction of the maximum compressional strain is given below the strain values. Sources for the strain rates are given in the text.

for examples). The tectonic stress system responsible for these earthquakes is not clearly understood.

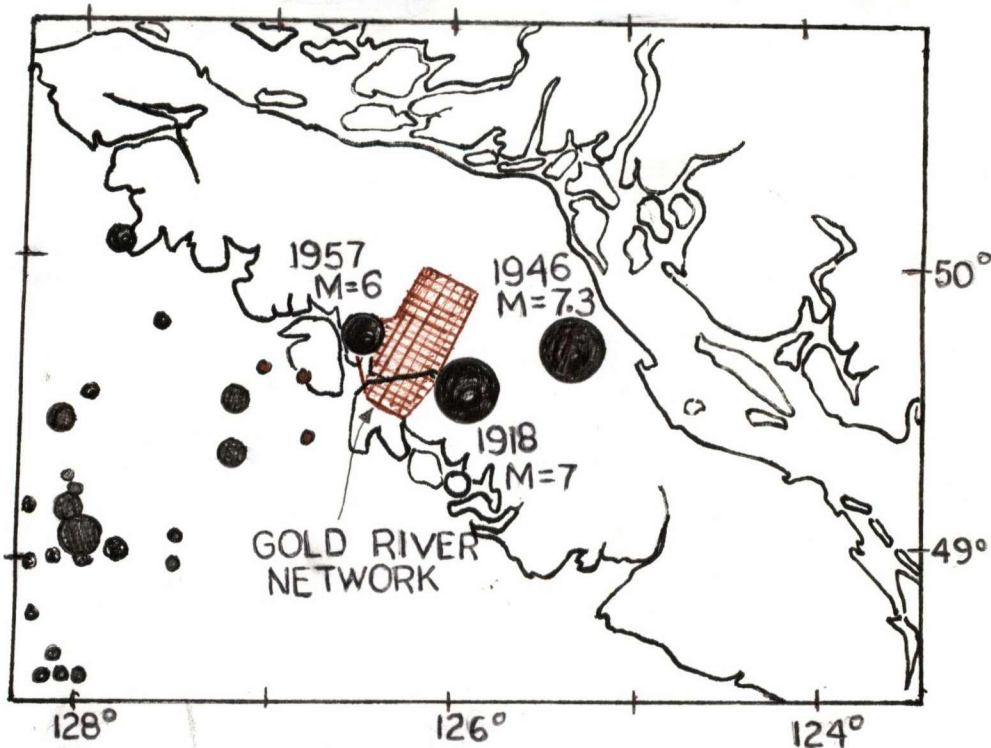


**Figure 1.2.** Map of Vancouver Island showing the locations of the large earthquakes of central Vancouver Island relative to the Gold River network (modified from *Rogers* [1983b]). The northeast trend of the Nootka fault zone is indicated by the epicenters plotted offshore of Vancouver Island.

The tectonics along the northwestern margin of North America is controlled by the interaction of the Pacific, North American, and the Juan de Fuca plates (Figure 1.1) [Atwater, 1970]. Active deformation along the transform margin between the Pacific and North America plates is well-documented by historic earthquakes. The convergent margin between the Juan de Fuca-North and North America plates, however, is nearly aseismic. Lacking are the shallow thrust earthquakes that usually identify subduction zones. Deep, Benioff-zone earthquakes in the subducted slab are rare, with only a few large, historic events in the Puget Lowlands in Washington. Other, less direct evidence for the case of subduction is necessary.

Ongoing subduction of the Juan de Fuca plate beneath the America plate in the Cascadia subduction zone off the coast of Oregon, Washington, and Vancouver Island is supported by a variety of geophysical and geological evidence [*Riddihough and Hyndman, 1976; Keen and Hyndman, 1979; Hyndman and Weichert, 1983; Riddihough et al., 1983; Taber and Smith, 1984*]. Many of the arguments favoring contemporary subduction assume the continuation of processes known to be active in the recent geologic past.

The lack of seismicity along the shallow interface between the Juan de Fuca plate system and the America plate has generally been interpreted as evidence for aseismic subduction (*e.g., Hyndman and Weichert [1983]*). Others (*e.g., Heaton and Kanamori [1985]*) have taken the opposite viewpoint, suggesting that the area may be a seismic gap. The seismic gap viewpoint is based on the observation of *Lay et al. [1982]* that the subduction of young, bouyant lithosphere is usually accompanied by large magnitude earthquakes. The subducting lithosphere of the Juan de Fuca plate is among the youngest in the world [*Heaton and Kanamori, 1985*]. Coupling between the subducting and overriding plates appears to be greatest when young oceanic lithosphere is being subducted (*e.g., the southern end of the Nazca plate in Chile*), and the least when old oceanic lithosphere is being subducted (*e.g., the Pacific plate in the Mariana trench*). *Peterson and Seno [1984]* found the seismic moment release rate to be correlated with the lithospheric age and absolute velocity of the upper plate. Moment release rates increased where young oceanic lithosphere was being subducted, but the relation was not simple. Seismic moment release rates along the convergent margins of the large Pacific plate were several times greater than the corresponding rates along the convergent margins of smaller oceanic plates. Subduction zones where the upper plate was overriding the subducting plate tended to be the most seismically active. Seismic moment release rates did not appear to be correlated with the rate of convergence [*Peterson and Seno, 1984*], but the largest magnitude events occur in seismic subduction zones with the highest convergence

rates [Lay *et al.*, 1982].

Models of contemporary plate interactions in the Cascadia subduction zone are complicated by possible differential motions between subplates within the Juan de Fuca plate. *Riddihough* [1977; 1984] has subdivided the Juan de Fuca plate into the Explorer, Juan de Fuca, and Gorda South plates on the basis of ridge orientation and spreading rates. His plate motion vector analysis shows the Juan de Fuca plate converging obliquely with the North America plate at an average rate of between 4 and 5 cm/yr over the last 0.5 Ma (Figure 1.1). *Nishimura et al.* [1984] give essentially the same rate using a slightly different model to account for reorientation of the Juan de Fuca ridge during the last 20 Ma. Relative motion of the Explorer plate is not as well determined. *Riddihough* [1977] assumed that spreading across the Explorer ridge was normal to the ridge axis, resulting in oblique convergence of about 2.5 cm/yr that is uniform along the plate margin. *Riddihough* [1984] accounts for fanning in the magnetic anomalies by pinning the Explorer plate near the northern triple junction. In this latter model spreading rates vary along the ridge axis, and the ridge slowly pivots away from the subduction zone (*Menard's* [1978] "pivoting subduction"). Convergence between the Explorer and North America plates varies along the plate margin: the pinned northern end of the Explorer plate is being overridden by the North America plate at an average rate of about 2 cm/yr, while southern end is actually retreating away from the plate margin resulting in an even lower convergence rate.

Relative motion between the Juan de Fuca and Explorer plates may occur on the oceanic Nootka fault zone [Hyndman *et al.*, 1979]. The fault zone is believed to extend northeast from the junction of the Juan de Fuca Ridge and the Sovanco fracture zone. It is marked by a broad band of seismicity and deformed sea-floor sediments. *Hyndman et al.* [1979] suggest left-lateral slip across the fault zone, a hypothesis that is supported by *Riddihough's* [1977; 1984] plate motion model and some poorly determined focal mechanism solutions. The central Vancouver Island earthquakes are localized along the general

onland extension of the Nootka fault zone, and *Hyndman et al.* [1979] postulate that these continental plate earthquakes may be related to motion across Nootka fault zone in the oceanic lithosphere through some form of stress coupling. *Rogers* [1979; 1983] suggests that the earthquakes are related to increased coupling between Explorer and North America plates. Regardless of the mechanism responsible for the earthquakes, some type of surface deformation should result from the stress system that produce the earthquakes.

## 1.2. CONTEMPORARY SURFACE DEFORMATION

The general pattern of contemporary vertical deformation along the entire coastline adjacent to the Juan de Fuca plate system appears to be a gentle landward tilting. Repeated leveling surveys and tide gauge records from this century [*Ando and Balazs*, 1979; *Reilinger and Adams*, 1982; *Riddihough*, 1982] show that the outer coastal areas are being uplifted at an average rate of about 3 mm/yr and the inner coastal regions are subsiding at about 1 mm/yr (Figure 1.1). Detailed profiles of the elevation change are only available for the Olympic Peninsula and parts of Oregon. In these areas, the average vertical velocities show a gradual decrease from the coast to the inland areas [*Ando and Balazs*, 1979, Figure 2; *Holdahl and Hardy*, 1979, Figures 4 and 6, *Reilinger and Adams*, 1982, Figure 1]. The comparison of leveling and tide gauge records in the Olympic Peninsula shows a relative velocity misclosure of only 1.6 mm/yr from the Pacific Ocean to Puget Sound [*Ando and Balazs*, 1979]. This agreement between independent systems leaves little doubt about the relative vertical displacement rate between the two locations. The amount of absolute vertical motion is less certain, as it is determined solely from tide gauge data that contain a eustatic sea level correction (1 mm/yr) not much smaller than the maximum uplift rate.

Whether this landward tilt represents cyclic strain accumulation or long-term secular deformation along this convergent margin has not been established. *Adams* [1984] found

recent marine and river terraces tilted to at an average rate of about  $3 \times 10^{-8}$  rad/yr, a rate consistent with that observed in nearby level lines by *Reilinger and Adams* [1982]. The geologic indicators along the central Washington coast, however, show differential uplift [Adams, 1984]. *Riddihough* [1982] points out that uplift at the rate currently being observed would produce elevation changes an order of magnitude greater than those indicated by the integrated geologic uplift over the last 10 Ma.

In regions of great, shallow thrust earthquakes (*e.g.*, Alaska and Japan) the coastline typically subsides and the land tilts toward the sea in the intervals between great earthquakes, whereas the deformation is reversed at the time of a great earthquake. The net deformation over several earthquake cycles is typically coastal uplift and tilting away from the ocean. This secular deformation is thought to be associated with imbricate thrust faulting branching upward from the main thrust zone [Fukao, 1979; Yonekura and Shimazaki, 1980]. The similarity between the short-term deformation observed along the coasts of Washington and British Columbia and the *secular* deformation of some seismically active coasts caused *Ando and Balazs* [1979] and *Riddihough* [1982] to suggest that subduction of the Juan de Fuca plate might be aseismic.

Measurements of horizontal deformation have been given for only a few areas in Washington and Vancouver Island (Figure 1.1). The strain accumulation values in Figure 1.1 are computed from angle or distance changes assuming uniform strain in space and time. Within estimated measurement error, all areas appear to be consistent with spatially uniform strain accumulation. Possible temporal changes are only determined in the Seattle network. Principal strain rates ( $\dot{\epsilon}_1, \dot{\epsilon}_2$ ) are given in Figure 1.1 in networks where the deformation is deduced from distance changes, while principal deviatoric strain rates ( $\dot{\epsilon}'_i = \dot{\epsilon}_i - \dot{\Delta}/2$ ; where  $\dot{\Delta} = \text{dilatation} = \dot{\epsilon}_1 + \dot{\epsilon}_2$ ) are given where the deformation is calculated from angle changes. In the discussion the tensor strains ( $\epsilon_{11}, \epsilon_{12}, \epsilon_{22}$ ) and the principal strains ( $\epsilon_1, \epsilon_2$ ) are given in units of  $\mu\text{strain}$  (ppm) and the units of the total

engineering shear strain ( $\gamma = \epsilon_1 - \epsilon_2$ ) in units of  $\mu\text{rad}$ . Azimuths are in degrees from north.

On Vancouver Island, angle changes between triangulation surveys in 1914 and 1966 across the Johnstone Strait indicate shear strain accumulation at an average rate of  $0.06 \pm 0.03 \mu\text{rad/yr}$  with the direction of maximum compression almost north-south [Slawson and Savage, 1979]. Coseismic strain accumulation across the epicentral area of the 1946 Vancouver Island earthquake (not shown in Figure 1.1) also indicates maximum compression in a north-south direction [Slawson and Savage, Table 3, 1979].

The other measurements of horizontal deformation show an east-northeast direction of maximum contraction. Repeated trilateration surveys between 1972 and 1985 across the Puget Lowlands near Seattle show average principle strain rates of  $0.03 \pm 0.02 \mu\text{strain}$  N21°W and  $0.03 \pm 0.01 \mu\text{strain}$  N69°E [Lisowski and Savage, 1986]. This rate of deformation is much lower than that reported for the same network during the 1972 to 1979 interval [Savage et al. 1981]. Strain accumulation from a 1892 to 1954 composite of repeated triangulation surveys across the Strait of Juan de Fuca shows maximum shear of  $0.22 \pm 0.07 \mu\text{strain/yr}$  with a N77°E $\pm$ 29° direction of maximum contraction [Lisowski and Savage, 1986]. Distance changes in the Olympic trilateration network between 1982 and 1983 show shear of  $0.45 \pm 0.23 \mu\text{rad/yr}$  with the direction of maximum contraction being N47°E $\pm$ 13° [Lisowski and Savage, 1986]. The short time between the initial and final surveys makes the results from the Olympic network very uncertain. Also shown in Figure 1.1 is the the average rate of strain accumulation in the Gold River network from angle changes between 1947 and 1982: shear strain accumulated at an average rate of  $0.23 \pm 0.12 \mu\text{rad/yr}$  with the direction of maximum contraction N56°E $\pm$ 12°. This result is derived in Chapter 4. Individually, the average strain rates are only marginally significant, but the the similarity in the orientation of the axis of maximum contraction in all these areas could be accounted for by a common tectonic stress.

## **2. THE 1982 GOLD RIVER TRILATERATION SURVEY**

In 1982 a high precision trilateration network was established near the town of Gold River in central Vancouver Island. The network includes a portion of a triangulation network surveyed during 1946 and 1947. The primary goals of the project were to establish a network capable of resolving strain accumulation at the 0.3 ppm level and to tie this network into the existing triangulation network to determine strain accumulation between 1947 and 1982. Most of the ties to 1947 triangulation monuments were made during 1982, but ties to two important 1947 monuments were not made until 1983. In the discussion I will refer to the measurements made during 1982 and 1983 as the 1982 Gold River survey. Chapter 2 documents the measurements that were made, and the instruments and procedures used during the 1982 survey.

### **2.1. THE 1982 MEASUREMENTS**

Four types of measurements were made during the Gold River survey: distances corrected for refractivity with aircraft-flown meteorological profiles, distances corrected with end-point meteorological readings, horizontal angles, and simultaneous reciprocal vertical angles. The 1982 measurements were made by George Houston, Byron Bresee, and Robert Duval of the Surveys and Mapping Branch of the Department of Energy, Mines, and Resources who will be referred to as the Geodetic Survey of Canada (GSC). Assisting in 1982 were Herb Draggert from the Pacific Geoscience Center of the Department of Energy, Mines, and Resources and Bill Slawson and myself from the University of British Columbia. The 1983 measurements were made by Herb Draggert and Bill Slawson. The 1982 and 1983 measurements are summarized in the tables and figures of part 2.1.

The primary distance measurements are those with refractivity corrections computed from aircraft-flown, temperature-humidity profiles and end-point air pressures. The 23 lengths measured in 1982 are shown in Figure 2.1, and listed in Table 2.1. Ties to the 1947



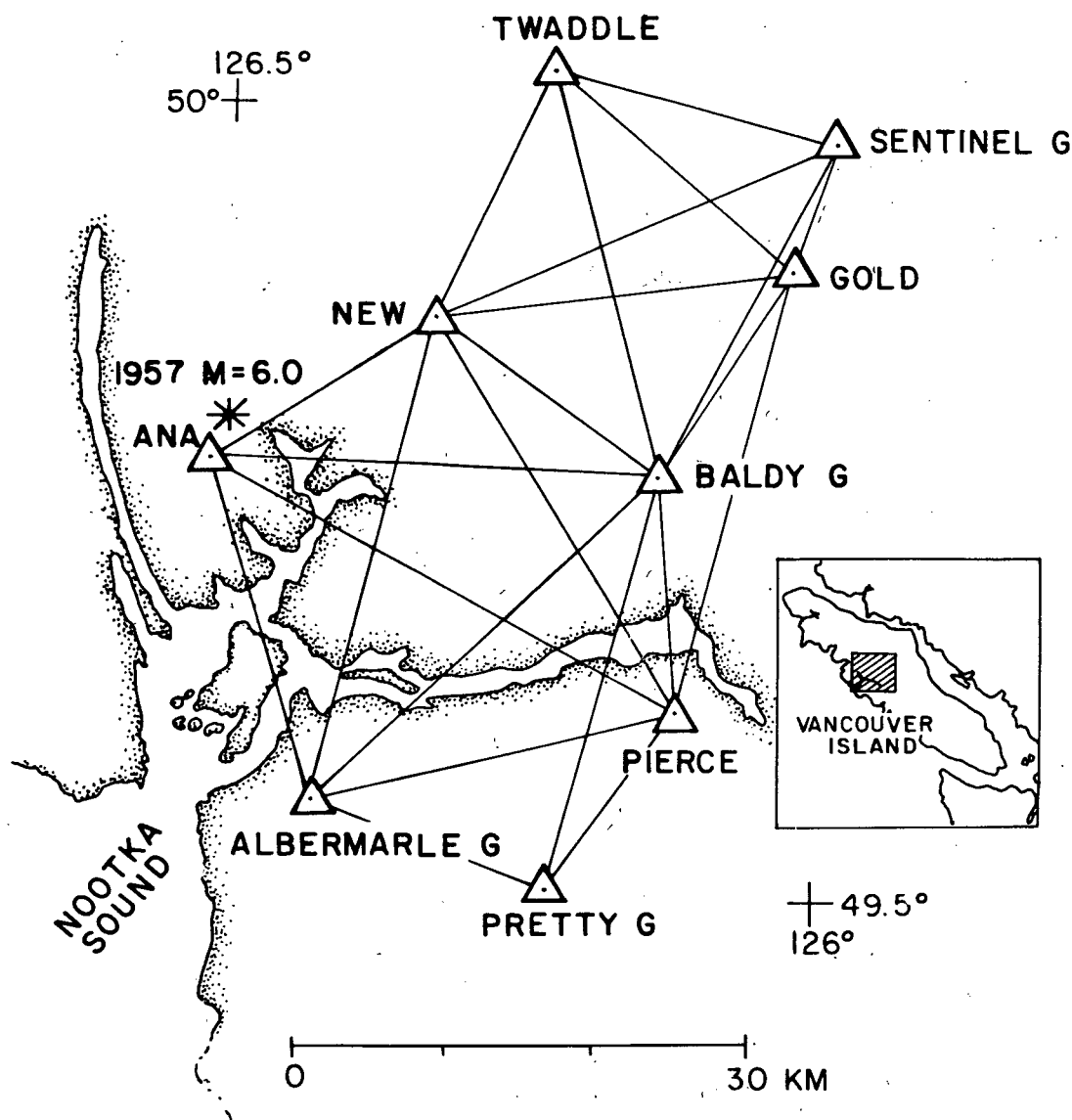


**Figure 2.1.** Map showing 1982 Gold River trilateration network. Inset shows the location of the network and the star marks the epicenter of the 1957 M=6.0 earthquake [Rogers, 1979]. The triangles mark the survey monuments and the lines represent measured distances. Only the distances with aircraft-flown meteorology are shown on this map.

stations were made with distance measurements corrected from end-point meteorological readings, and horizontal angles. These distances and angles are shown in Figure 2.2 and listed in Tables 2.1 and 2.2. The simultaneous, reciprocal vertical angles provide elevation control, which is particularly important in the adjustment of trilateration networks. The vertical angles measured are shown in Figure 2.3 and derived elevations (provided by the

**Table 2.1.** 1982 and 1983 Distances

Station 1	Station 2	Slope Distance (m)	Arc Distance* (m)
Complete Meteorology			
Albermarle Geod	Ana	23499.927	23495.845
	Baldy Geod	30811.412	30800.206
	New	32393.728	32385.591
	Pierce	24998.291	24991.146
	Pretty Geod	17239.587	17236.127
Ana	Baldy Geod	29940.256	29929.987
	New	17347.225	17341.366
	Pierce	36034.882	36026.707
	Gold	16210.979	16206.246
Baldy Geod	New	18531.153	18525.770
	Pierce	15771.634	15766.626
	Pretty Geod	28429.760	28420.447
	Sentinel	25197.822	25190.885
	Twaddle	28994.216	28986.213
Gold	New	23948.638	23940.614
	Pierce	30199.231	30190.044
	Sentinel	9173.344	9170.847
	Twaddle	21880.387	21874.411
New	Sentinel	29034.043	29025.073
	Pierce	31302.719	31295.846
	Twaddle	18533.580	18525.792
Pierce	Pretty Geod	14700.131	14695.518
Sentinel	Twaddle	20231.954	20227.427
End-point Meteorology			
Pretty Geod	Pretty	3.316	3.316
Albermarle Geod	Albermarle	1.045	1.045
Ana	Walker	4938.152	4937.163
Albermarle Geod	Pretty	17237.488	17234.002
Twaddle	Wanch	5097.872	5094.194
Baldy Geod	Baldy	28.448	27.916
New	Conuma†	4343.561	4341.999
Gold	Conuma†	22784.861	22777.772
Pierce	Conuma†	26977.224	26971.031
Pierce	Rufus†	17352.451	17346.938
Pretty Geod	Rufus†	12000.566	11998.290
Baldy Geod	Rufus†	24405.312	24395.561

\* Slope distance projected onto the 1866 Clarke spheroid with geoidal heights.

† Measurements made in July, 1983.

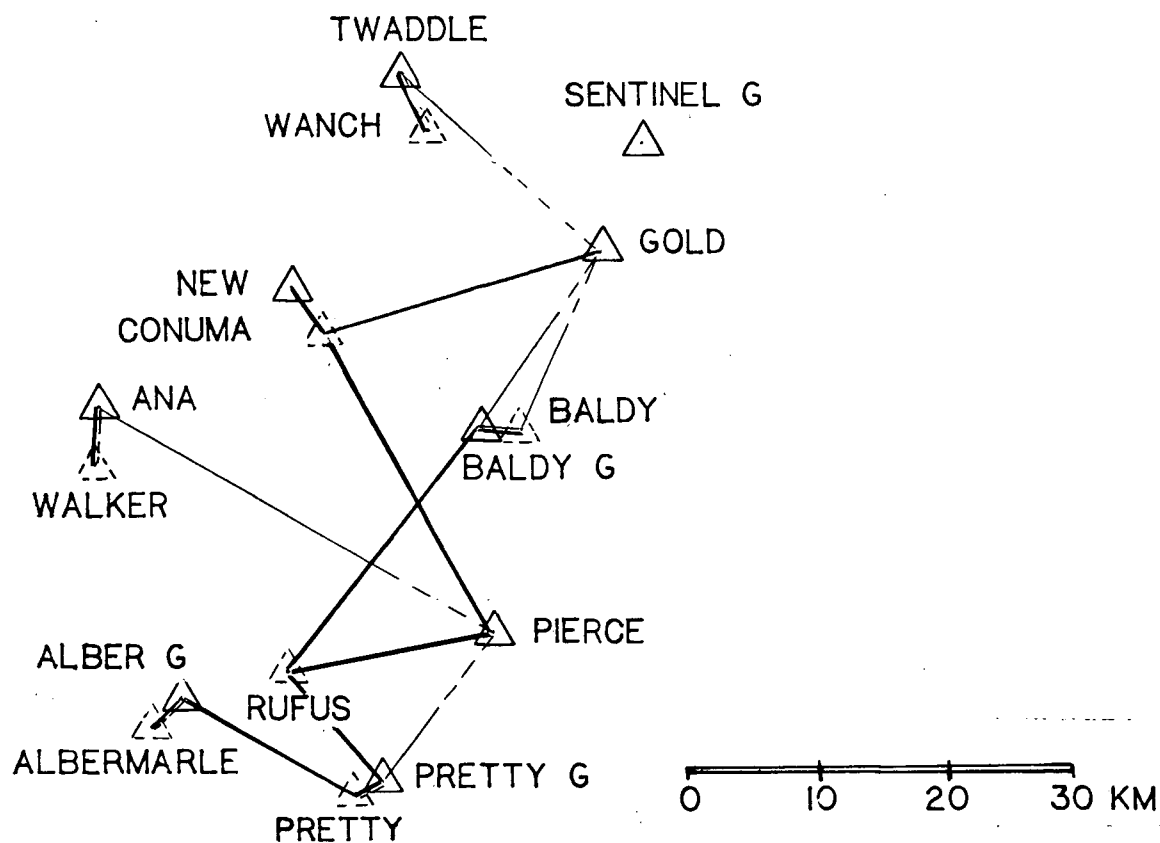


**Figure 2.2.** Sketch of the horizontal ties between 1947 and 1982 survey monuments. The 1982 survey monuments are marked by solid triangles and the 1947 survey monuments by dashed triangles. Gold, Pierce, and New are common to both surveys. Distances measurement are shown as solid heavy lines and horizontal angles by the thin lines with the dashed end indicating the station sighted. Stations Baldy and Baldy Geod, Albermarle and Albermarle Geod, and Pretty Girl and Pretty Geod are very close to one another.

**Table 2.2.** 1982 Horizontal Angles

Instrument Station	Initial Station	Target Station	Angle ° ' "
Baldy	Gold	Baldy Geod	240 49 07.67
Baldy Geod	Gold	Baldy	60 43 45.24
Twaddle	Gold	Wanch	16 55 58.52
Pretty Geod	Pierce	Pretty	207 11 08.25
Albermarle Geod	Pretty	Albermarle	99 00 22.75
Ana	Walker	Pierce	69 10 21.91

**Table 2.3.** 1982 Elevations, Latitudes, and Longitudes

Station	Elevation* (m)	Latitude			Longitude		
		°	'	"	°	'	"
Albermarle	1060.62	40	35	05.9885	126	27	43.7807
Albermarle G	1060.15	49	35	06.0162	126	27	43.7509
Ana	1120.25	49	47	21.1530	126	32	43.9345
Baldy	1609.87	49	45	38.5043	126	07	55.1204
Baldy G	1604.44	49	45	38.5996	126	07	56.5074
Gold	1731.60	49	52	46.3094	126	00	07.1901
New	1410.51	49	51	50.7839	126	20	02.9955
Pierce	1402.56	49	37	09.0340	126	07	13.6490
Pretty	1183.56	49	30	59.6042	126	14	54.5662
Pretty G	1183.11	49	30	59.6160	126	14	54.5830
Sentinel G	1737.73	49	57	23.4540	125	57	22.5948
Twaddle	1754.68	50	00	52.4932	126	13	24.7185
Walker	1152.90	49	44	44.1149	126	33	29.6111
Wanch	1600.83	49	58	29.3728	126	11	17.7400
Rufus	1134.2†	49	35	56.9338	126	21	29.2507
Conuma	1481.3†	49	49	43.2470	126	18	31.7172

\* Elevations provided by the GSC  
† Elevations from B.C. Ministry of Surveys based on 1947 vertical angles

GSC) are listed in Table 2.3.

The comparison of the 1947 angles with the 1982 distances and angles is made by inverting the corresponding angles from the adjusted positions for the 1982 survey. The adjustment requires converting the measured slope distances to distances on the surface of a particular spheroidal representation of the earth (the 1866 Clarke Spheroid was used). This projection requires the elevations of and approximate azimuths between the monuments (see *Bomford* [1980]). The elevations used in this computation are referenced to the geoid (an equipotential gravity surface) with no correction made for the difference between the geoid and the Clarke spheroid. The Clarke-arc distances and measured horizontal angles are then used to find the most probable station positions with a variation of coordinates adjustment [*Bomford*, 1980]. The position of Pierce and the azimuth to Gold

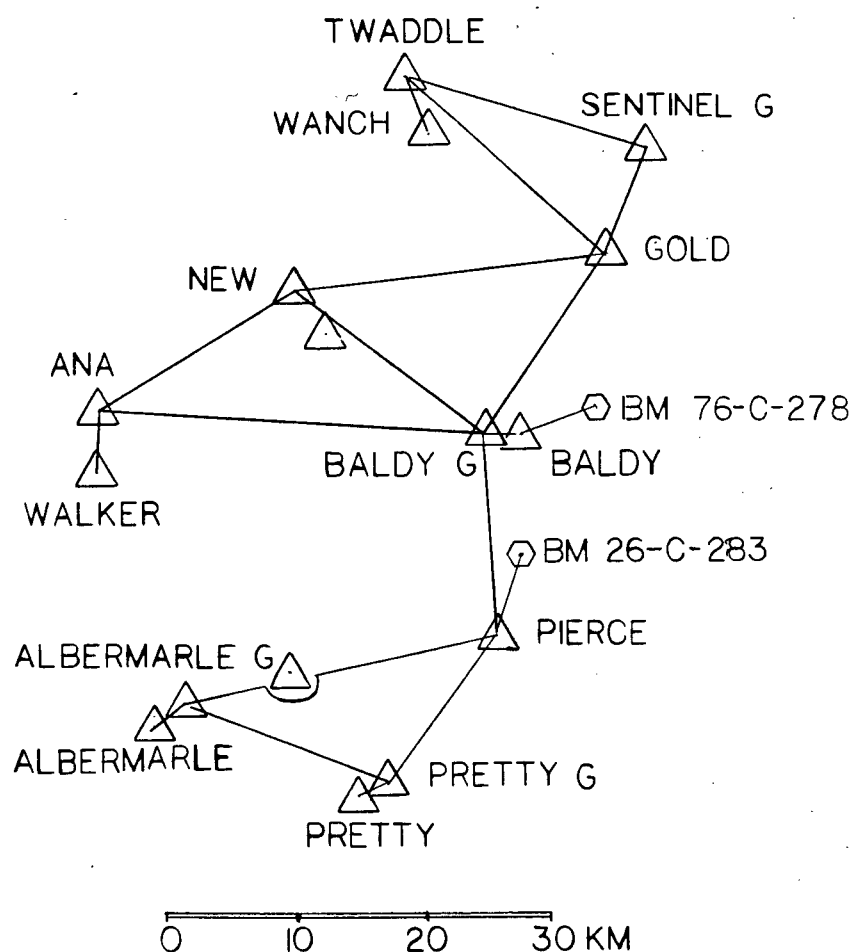


**Figure 2.3.** Map showing the simultaneous reciprocal vertical angles that were measured during the 1982 Gold River network survey. The hexagons are vertical control benchmarks.

were arbitrarily fixed to remove the translational and rotational ambiguities inherent in a solution for a network that is not fixed to an external reference. The derived latitudes and longitudes are from a local adjustment and are not suitable for horizontal control. The positions from this local adjustment are listed along with the elevations in Table 2.3.

## 2.2. INSTRUMENTS AND PROCEDURES

Of the four types of measurements made during the 1982 survey of the Gold River network, only the distance measurements that have been corrected for refractivity delays using aircraft-flown temperature and humidity profiles use non-standard surveying techniques. The following discussion concerning equipment and procedures is limited to these distance measurements. The discussion is divided into three areas; the distance meter and reflectors, the aircraft mounted temperature-humidity probes, and the pressure sensors. Appendix A contains a brief summary of the basic principles of electro-optical distance measurements.

### 2.2.1. DISTANCE METER

A Keuffel and Esser Rangemaster III was used to make all distance measurements. It is a long-range ( $> 40$  km maximum), electro-optical distance meter that has a 5 mW helium-neon laser (carrier wavelength of  $0.6328 \mu\text{m}$ ). The helium-neon laser is amplitude modulated at a nominal frequency of  $14,984,979.7$  Hz (assuming a nominal refractive index of  $1.000310$ ). The standard error in a measured distance  $L$  (m) is estimated in this section to be

$$\sigma(\text{m}) = \sqrt{(0.0057)^2 + (0.2 \times 10^{-6})^2 L^2}$$

or about 0.3 ppm for a 24,000 m distance. A discussion of the instrument design and the related measurement errors for a Rangemaster III may be found in *Berg et al.* [1981]. Summarizing their discussion and that of *Greene* [1977], the main sources of instrumental error are modulation frequency instability, pointing error, zero error, non-linearity in the phase detector, receiver noise, and error related to the amplitude of the return signal.

#### 2.2.1.1. Modulation frequency stability

The short-term stability of the modulation frequency was tested by the GSC over a temperature range of  $0^\circ$  to  $23^\circ\text{C}$ . After a 20 minute warm-up, drift in the modulation

frequency over a 7-hr period of continuous operation was less than 0.05 ppm. A plot of the frequency drift over time from these tests is shown in Figure 2.4.

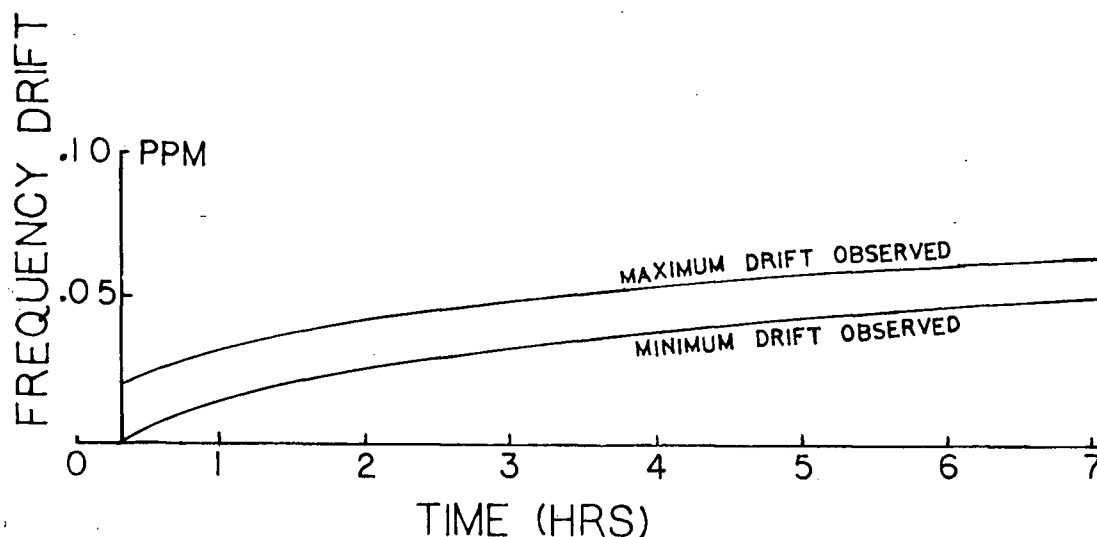


**Figure 2.4.** Plot of ppm drift in the modulation frequency as a function of operating time in hours. The envelope encloses the range of readings taken over 7 days at ambient temperatures from 0° to 23°C.

Possible long-term drift of the modulation frequency was checked during the Gold River survey by daily measurements with a portable frequency standard. These measurements showed an apparent variation of 0.05 ppm in the modulation frequency relative to the nominal value. A drift of 0.05 ppm would change the measured distance in the longest line (35 km) by less than 1.5 mm. The uncertainty in the time base of the portable frequency standard is about the same as the measured drift, and no correction is made to the measured distances.

#### 2.2.1.2. Pointing error

Pointing error may occur when the return beam does not illuminate the entire area of the receiver optics. Short measurements (< 300 m) to retro-reflector are particularly sensitive to pointing error. Pointing error may be assessed by noting the change in the measured distance produced by focusing the return beam on different parts of the receiving telescope. If the span of the distances measured with a Rangemaster III is greater than 10 mm it

indicates misalignment of the optics [Berg *et. al.*, 1981]. During long measurements, the random scattering of the beam tends to average out the pointing error.

#### **2.2.1.3. Zero error**

Constant error in a measured length results from the combination of errors in the instrument and reflector correction constants and the linearity of the phase detector. It is assumed that the instrument constant is independent of the length. Short term fluctuations in the electronic center of the Rangemaster III are automatically corrected during a distance measurement by alternating rangings with measurement of an internal fiber optics path. The small unknown phase shifts introduced by the electronic components are assumed to affect each measured length by the same amount. The displayed distance is the difference between the instrument-reflector distance and the internal path distance. The instrument constant corrects for this internal path length and any constant offset between the electro-optical and mechanical center of the instrument. The reflector constant corrects for the offset introduced by the reflector and its mount. The zero error is the combined error in the instrument constant and reflector constant. Some of the measurements used to determine the instrument constant are discussed in subsection 2.2.1.7.

#### **2.2.1.4. Cyclic error**

Non-linearity in the phase detector produces cyclic error that varies over one effective wavelength (10 m for the Rangemaster III). It is due to leakage (electrical or optical, or both) between the modulator and the receiver electronics or optics. This error tends to be sinusoidal over the effective wavelength (10 m) with a maximum amplitude of  $\pm 5\text{mm}$  for the Rangemaster III. No tests were made to determine the cyclic error.



#### **2.2.1.5. Receiver noise**

On long-range measurements where the return signal is relatively weak, noise in the photo-detector and receiver contribute to measurement error. Noise tests [*Berg et al.*, 1981, p 22] show that receiver noise can contribute 2 mm to the standard error in a distance measurement.

#### **2.2.1.6. Return signal strength**

The Rangemaster III acquires distance measurements only when the return signal strength is within a relatively narrow range. The return signal strength is adjusted by the operator by means of a grey wedge filter. On long lines or under turbulent conditions, the return signal strength varies considerably requiring frequent adjustment. Even though the allowable range of return signal is small, variations within this range may change the measured distance because the zero-crossing detector is sensitive to the return signal level. No tests were made to determine the magnitude of this error, but during the survey care was taken to keep the signal in the middle of the allowable limits.

#### **2.2.1.7. Instrument constant for Rangemaster III # 8016**

Measurements of the Victoria baseline were made before and after the Gold River survey to check the instrument constant. The 1.7 km Victoria baseline is comprised of a set of 6 piers with forced centering mounts. Reference baseline distances are derived from an adjustment of Mekometer surveys made in 1975, 1977, and 1978. The Mekometer is a high precision short-range distance meter with a precision of  $\pm 1$  ppm [*Rinner*, 1974].

Measurement of a distance of known length determines the total correction resulting from the sum of the instrument constant, reflector constant, and the non-linearity. Generally, short baselines are used to reduce refractivity related scale error. This is a compromise, however, because short distance measurements are most likely to be subject to pointing error (see 2.2.1.2).

**Table 2.4.** Victoria baseline measurements with Rangemaster III # 8016

Date	Inst. Station	Refl. Station	Slope Dist. (m)	Inst. constant	Refl. ID	Mount style
6 July 1982	Pier 2	Pier 5	1582.384	0.133	# 35	single
			1582.393	0.129	# 36	single
			1582.380	0.142	# 14, 15	16
			1582.380	0.142	# 2, 3	16
	Pier 2	Pier 4	953.618	0.134	# 36	single
			953.618	0.134	# 35	single
			953.614	0.140	# 2, 3	16
			953.615	0.137	# 14, 15	16
	Pier 2	Pier 0	230.031	0.141	# 35	single
			230.032	0.140	# 36	single
			230.030	0.142	# 14,15	16
			230.031	0.141	# 2, 3	16
24 July 1982	Pier 2	Pier 5	1582.383	0.139	# 35	single
			1582.385	0.137	# 2, 3	16
			1582.385	0.137	# 14, 15	16
	Pier 2	Pier 4	953.614	0.138	# 35	single
			953.617	0.135	# 14, 15	16
			953.616	0.136	# 2, 3	16
	Pier 2	Pier 0	230.027	0.145	# 35	single
			230.031	0.141	# 2, 3	16
			230.031	0.141	# 14, 15	16
Mean Values	Pier 2	Pier 5		0.137±0.005		
	Pier 2	Pier 4		0.136±0.002		
	Pier 2	Pier 0		0.142±0.002		
			mean	0.138±0.004		

The distance between 3 piers separated by 230, 953, and 1582 m were measured with the Rangemaster III # 8016 before and after the 1982 Gold River network survey. End-point meteorological readings were used to determine the refractivity correction to a measured length. Rangings at each distance were made to two different reflectors in a single mount and to two different pair of reflectors in the 16-reflector mount that was used for all the Gold River measurements. The vertical rotation axis of the square, 16-reflector

mount passes between the two central columns of reflectors and to assure symmetry about this axis the calibration measurements were made to a set of two reflectors. The derived instrument constant assumes a reflector constant of -0.030 m (specified by the GSC). The pier-to-pier distances and instrument constants are listed in Table 2.4. Each distance represents the average of about 20 readings. There does not appear to be any systematic difference between the single and 16-reflector mounts, or between the 6 July and 24 July 1982 surveys. The standard deviation of the instrument constant from the 7 measurements at each distance varies between 2 and 5 mm. The mean instrument constant from these tests is  $0.138 \pm 0.004$  m. The instrument constant used in the reduction of the distances measured in the Gold River survey is 0.140 m. This value was obtained by the GSC from baseline measurements in Ottawa taken before and after the Gold River survey.

The relative contribution of pointing error, meteorological error, non-linearity, and baseline error are not known. Pointing error is probably significant in only the 230 m distance, as the beam diverges enough to illuminate the entire receiving telescope at the 953 and 1582 m distances.

### 2.3. AIRCRAFT PROBES

During the 1982 trilateration survey of the Gold River network, simultaneous aircraft-flown temperature and humidity profiles were obtained with GSC and U.S. Geological Survey (USGS) sensor systems. The credibility of the GSC system was established by comparing its temperature and humidity measurements with those from the time-proven USGS system.

Temperature and humidity sensors for each system are installed within an open-ended, shielded, cylindrical enclosure. The unit made up of the sensors, protective shield, and radiation shield is called a probe. In the normal configuration a probe is placed on each side of the aircraft, mounted on a landing or wing strut, and orientated parallel to the long axis of the aircraft. Throughout the 1982 survey two probes from each system (a total of four) were attached to the aircraft.

The USGS probe will be used as the standard for comparison, except in tests where mercury thermometers are used. The precision of the USGS probe has been established by over 10 years of trilateration measurements. A description of the system and measurement precision may be found in *Savage and Prescott* [1973] and a discussion of possible related systematic error in a measured distance may be found in *Savage et al.* [1981b]. They estimate standard errors of  $\pm 0.1^{\circ}\text{C}$  and  $\pm 0.3\text{ kPa}$  for the mean temperature and water vapor pressure measured with the USGS probe.

Comparison of profiles flown during the 1982 survey show the GSC probes measuring systematically higher temperatures and lower humidities than the USGS probes. A change of about  $+0.2\text{ ppm}$  in a distance measurement would result from these differences. Some possible sources for this systematic difference are miscalibration of the sensors or an improper correction for the heating caused by the flow of air through the probe. Static and dynamic calibration tests were made following the 1982 survey, but the results are inconclusive.

During an EDM measurement the sensor equipped aircraft is directed along the optical path between the survey stations by observers at either end of the line. A data logger located within the aircraft periodically scans and records the sensor readings. The resulting temperature and humidity profiles along with end-point pressure readings are used to compute the refractive index, which provides a scale correction to a measured length. A discussion of the refractive index scale correction is given in Appendix A.

Accurate meteorological sensors are essential for a precise EDM distance measurements. This discussion will emphasize the assessment of temperature errors, because they are likely to contribute the greater part of the meteorological dependent error to a distance measurement. Error in the water vapor pressure, which is derived from the combination of humidity, temperature, and pressure readings, constitute a relatively smaller fraction of the total meteorological error budget (see Appendix A, equation A.12 for the ppm change for an increment of temperature, pressure, or water vapor pressure).

Temperature calibrations of the probes were attempted in static and dynamic airflows. The tests lacked a suitable reference thermometer, but comparison of the temperatures that were measured by the two different probe systems showed good agreement. Maximum airflow velocity in the dynamic calibration tests was about half of the velocity flown during a field measurement of a profile. Good agreement between the measurement systems in the static and low-speed air flows makes the air-flow-velocity temperature correction for the CGS probe the most likely source of the error in profile temperatures. The small differences observed in these tests are opposite in sign from those in the profiles, implying that the air-flow-velocity correction used was too small. Only one test was made in air flow velocities similar to those experienced during the measurement of a profile. The results from this test, however, were not internally consistent and indicated a velocity dependent correction for the CGS probe that would increase the temperature difference in the profiles to nearly  $1^{\circ}\text{C}$ .

### 2.3.1. TEMPERATURE MEASUREMENTS IN FAST AIRFLOWS

This discussion of possible errors in airborne temperature measurements is limited to evaluating instrumental error and the temperature rise experienced by a sensor within a probe placed in a fast air flow. The comparison of the two systems is not affected by path variations or by airspeed inaccuracy. The background material for this discussion is from a comprehensive review of airborne temperature measurements by *Trenkle and Reinhart* [1973].

Possible instrumental errors include sensor calibration and scale error, recording error, self-heating error, response-time error, and electric lead error. Sensor calibration and scale error may be assessed by laboratory comparisons of the sensor temperature readings with a temperature standard over the range of temperatures encountered under field conditions. Recording error may be evaluated by replacing the probe with a high stability circuit of known value. The self-heating error requires determining the current flow through the thermistor and the dissipation constant of the thermistor. The current causes Joule ( $i^2R$ ) heating within the thermistor, changing its temperature. The dissipation constant is defined as the amount of power required to raise the temperature of the thermistor  $1^\circ\text{C}$  above the ambient temperature. It varies with the surface area of the thermistor and the medium being measured. In a thermally conductive medium such as a fast airflow, the heat is rapidly dissipated and the dissipation constant is about 1/10 of the value in still air. For a bead thermistor in a 5 m/sec airflow the dissipation constant is about 8 mW/ $^\circ\text{C}$  [*Omega*, 1984]. No significant self heating will occur if the excitation current is small.

The response time for a thermistor in a thermally conductive media is about 10 s or less [*Omega*, 1984], making response-time error insignificant for the typical flown profile. The electric lead error is not generally considered important for high resistance thermistors.

The heating of the temperature sensor in a fast air flow is more difficult to assess. The physical characteristics of the sensor and probe determine the reduction in flow velocity

and thus the proportion of the kinetic energy of motion converted to molecular motion. Although physically impossible, the complete conversion of the energy of motion into thermal energy would result in the full adiabatic temperature rise,  $\Delta T_k$ .

Assuming no addition or dissipation of heat, the full adiabatic temperature rise is experienced by a thermometer in the center of a container open only in the direction of flow. The full adiabatic temperature rise is given by

$$\Delta T_k = \alpha V_t^2 \quad (2.1)$$

where  $V_t$  = true airspeed (m/s) and

$$\alpha = \frac{1}{gJC_p} = \frac{1}{1987} {}^\circ C \frac{s^2}{m^2} \quad (2.2)$$

with  $g$  = the gravitational acceleration of the earth,  $J$  = the mechanical equivalent of heat, and  $C_p$  = the specific heat of air [Trenkle and Reinhart, 1973, pg 33].

The true airspeed,  $V_t$ , differs from that indicated by the aircraft pitot tube,  $V_i$ , by a density correction factor, which varies with the air temperature and pressure. That is

$$V_t = V_i \frac{T}{288} \frac{101.3}{P} \quad (2.3)$$

where  $T$  = absolute air temperature and  $P$  = the total air pressure in kPa. Equation 2.3 assumes that the pitot tube is calibrated for no correction at 288 K and 101.3 kPa. Calculating the full adiabatic temperature rise requires use of the true airspeed because air is compressible.

To obtain the temperature of the unperturbed air, that is, the static temperature,  $T_s$ , the air temperature measured by the probe,  $T_m$ , is corrected by the proportion of the full adiabatic temperature rise recovered by the probe. The ratio of the probe temperature rise to the full adiabatic temperature rise is called the recovery factor,  $r$ , that is

$$r = \frac{\Delta T_{kr}}{T_k} \quad (2.4)$$

The desired relationship between the static air temperature and the measured air temperature is then

$$T_s = T_m - r\Delta T_k = T_m - r\alpha V_t^2 \quad (2.5)$$

Assuming that the probe and the pitot tube are subjected to the same air flow velocity, only the recovery factor needs to be determined to compute the static temperature from the measured temperature and the true airspeed. For some geometric shapes, such as flat plates,  $r$  is a constant, but for others  $r$  may vary with the velocity [Hinton, 1938]. It is assumed that  $r$  is approximately constant over the limited range of airspeeds used for the aircraft flights.

The recovery factor may be determined in the controlled conditions of a wind tunnel or by field tests. Effects due to variation in the location and orientation of the probe on the aircraft can only be checked in the field. The optimum tests, both in the wind tunnel and in the field, require a suitable reference thermometer. A total temperature probe, which is calibrated for recovery error, is recommended for calibration tests by *Trenkle and Rheinhardt* [1973]. With a well designed total temperature probe,  $r$  is very close to 1 and only the true airspeed needs to be measured to obtain the static temperature from the measured temperature [Stickney et al., 1981].

Lacking a suitable reference thermometer, the recovery factor may be estimated by comparing temperature readings taken in a range of velocities to the static air temperature from an independent source. The static air temperature may be approximated by assuming a linear change in the ambient temperature during the testing period.



### 2.3.2. PHYSICAL DESCRIPTION OF THE PROBES

The USGS probe contains two temperature-sensitive resistors (thermistors) wired in parallel and a carbon coated, humidity-sensitive resistor (hygristor) mounted within the inner of two open-ended, concentric cylindrical shields. The cylindrical shields measure 60 and 100 mm in diameter by 300 mm in height. The shields are phenolic plastic, chosen for its nonconducting and insulating properties. The thermistors and hygristors used in the probe are manufactured by Viz Manufacturing Co. The thermistors and hygristor are exposed to the direct air flow through the inner cylinder. The relation between the temperature and resistance of the thermistor is found by using three factory supplied calibration points to solve for the curve-fitting constants in the Steinhart-Hart equation

$$\frac{1}{T} = A + B \ln R + C \ln R^3 \quad (2.6)$$

where  $T$  is the absolute temperature,  $R$  the resistance of the thermistor at  $T$ , and  $A$ ,  $B$ , and  $C$  are curve fitting constants [Omega, 1984].

For the two Viz thermistors a change of  $+0.1^\circ$  at  $0^\circ\text{C}$  results in a  $40\Omega$  decrease and a change of  $+0.1^\circ$  at  $30^\circ\text{C}$  results in a  $15\Omega$  decrease. The sensitivity of the thermistor is, thus, lower at higher temperatures. The resistance of the wire connecting the thermistors to the ohm-meter is much less than  $5\Omega$  and will, therefore, not produce a significant error in the measured temperature.

The resistance of the hygristor increases with humidity, becoming very large in saturated conditions. The resistance in the circuit is limited with a  $20\text{k}\Omega$  resistor wired in parallel with the hygristor.

The GSC probe contains a Weathermeasure HT-100R temperature and humidity sensor. The rod shaped unit is mounted within the inner of two open-ended aluminum cylinders. The HT-100R contains a three thermistor composite and a wafer capacitive-type humidity element, both mounted on the tip of an 25 by 100 mm rod-shaped housing. The

sensors are protected by a screen with either 300 or 500 micron size openings. The filter cap is required in order to protect the humidity element from contamination by particulate matter. The separate, battery-powered readout unit has a switchable display and a linear 0 to 5 volt output corresponding to a temperature range of  $-5^{\circ}$  to  $45^{\circ}\text{C}$  and 0 to 100% relative humidity. The temperature ( $^{\circ}\text{C}$ ) and relative humidity are given by  $T = -5 + 10V_T$  and  $R.H. = 10V_H$ ,  $V_T$  is the temperature voltage and  $V_H$  is the humidity voltage. Specifications given by Weathermeasure for the HT-100R are: a temperature accuracy  $\pm 0.2^{\circ}\text{C}$  and a humidity accuracy of  $\pm 3\%$  at 0 to 80% relative humidity,  $\pm 5\%$  at 80 to 100% relative humidity.

### 2.3.3. AVERAGES FROM TEMPERATURE HUMIDITY PROFILES

Temperatures from the profiles recorded for the two systems contain no instrumental corrections. Factory provided calibration curves are used to convert sensor readings to temperature and humidity. The temperature readings for both types of probes are corrected for kinetic temperature rise using equation (2.5) and assuming a recovery factor of 0.6. This is the value empirically derived for the USGS probe [*Savage and Prescott, 1973*]. The recovery factor for the GSC probe is not known; my tests and those made by the GSC to determine the recovery factor for the GSC probe are inconclusive.

The average temperatures measured with the GSC probes were  $0.3^{\circ} \pm 0.04^{\circ}\text{C}$  higher than those measured with the USGS probes. Figure 2.5 shows the average profile temperature differences; the temperature differences are constant over the range of temperatures encountered during the survey. A temperature change of  $0.3^{\circ}\text{C}$  would alter the refractive index scale correction by 0.3 ppm.

The relative humidity averages from the simultaneous profiles differ by  $-11.1\% \pm 2.8\%$ . As shown in Figure 2.6, the humidity differences appear to increase linearly. The humidity, air temperature, and air pressure determine the partial pressure of water vapor. The water

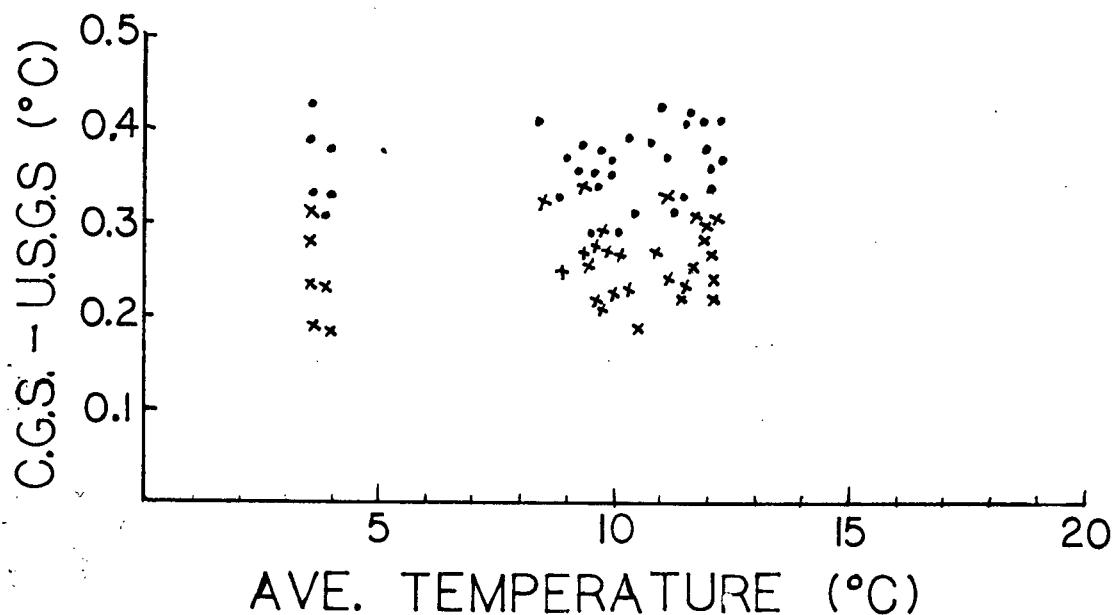


**Figure 2.5.** Plot of the temperature difference in  $^{\circ}\text{C}$  between averages obtained with the CGS and the USGS probes plotted relative to the USGS average temperature. Both systems are corrected for the kinetic temperature rise with a recovery factor of 0.6, the know value for the USGS probe; the recovery factor of the CGS probe is undetermined. The differences for the probes on the right side of the aircraft are shown with X's and dots are used for differences from probes on the left side. The probe ID'S are; USGS right 17, left 280; CGS right readout 1193, right probe 1851, left readout 1125, and left probe 1319.

vapor pressure is fundamental in the calculation of the refractive index (see Equation A.11). Comparison of the two systems, therefore, should be made between the calculated value of the water vapor pressure not relative humidity. A plot of the water vapor pressure difference as a function of the USGS water vapor pressure is shown in Figure 2.7. The ppm change in the refractive index scale correction is 0.4 that of the vapor pressure in kPa. For the low temperatures encountered in the Gold River survey, the observed humidity difference of 10% would change the refractive index less than  $-0.1$  ppm.

The net effect of the temperature and humidity differences is a relative change of  $+0.2$  ppm in the length of a line corrected with the temperatures and humidities measured with the GSC probe. Although the humidity difference was large, the low ambient temperatures encountered during the survey resulted in low water vapor pressures. The

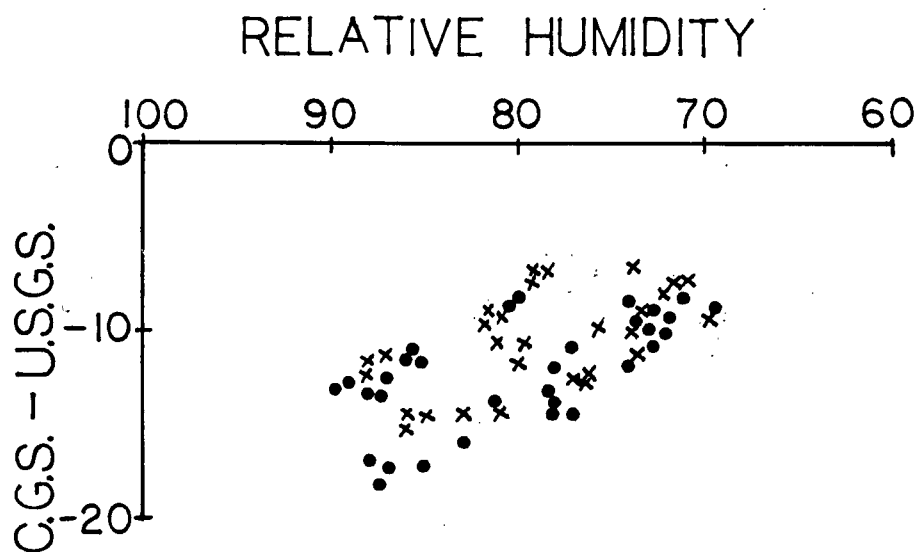


**Figure 2.6.** Relative humidity difference between averages obtained with the CGS and the USGS probes plotted relative to the USGS average relative humidity. X's are differences from the probes on the right side of the aircraft and dots are differences from the probes of the left side. Sensor ID's are the same as in Figure 2.5.

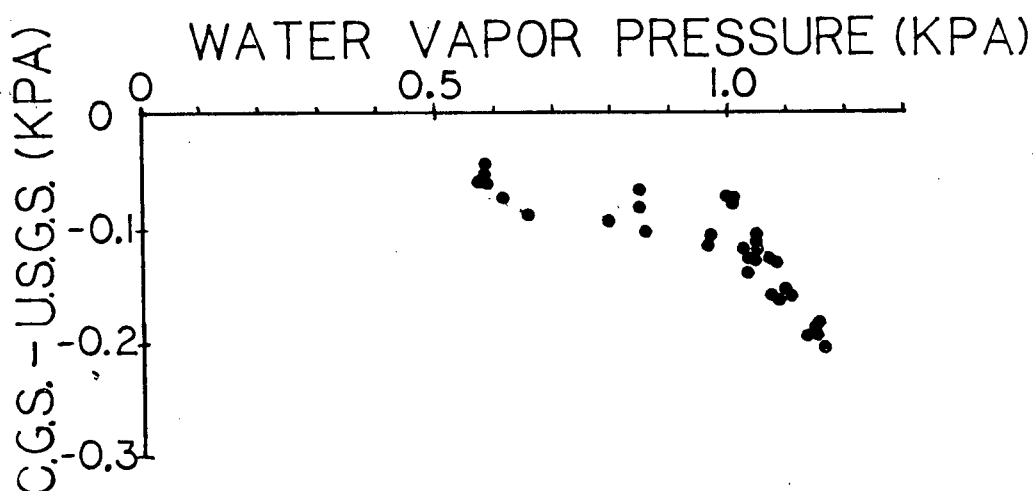


**Figure 2.7.** Computed water vapor pressure difference (kPa) between the GSC probes and the USGS probes relative to the average water vapor pressure measured by the USGS probes. The ppm change in the refractive index scale correction is 0.4 times the vapor pressure difference in kPa. Sensor ID's are the same as in Figure 2.5

same difference in the measured humidity at a higher ambient temperatures would produce a larger difference in the water vapor pressure. Nevertheless, even in conditions of high humidity and high temperature a 10% difference in the water vapor pressure would result

**Table 2.5. Laboratory Airbath Temperature Comparison**

Time	C1 (k $\Omega$ )	°C	Displ left*	Volts	°C	Displ right*	Volts	°C	Hg Therm
11:04	13.28	2.82	2.16	0.717	2.17	2.44	0.754	2.53	2.47
12:15	12.25	5.81	5.51	1.051	5.51	5.60	1.070	5.70	5.36
13:34	10.72	10.94	10.88	1.589	10.89	10.85	1.597	10.97	10.42
16:14	9.36	16.28	16.36	2.138	16.38	16.33	2.142	16.42	16.06
16:55	7.87	23.41	23.56	2.854	23.54	23.20	2.835	23.35	23.4
17:44	6.79	29.76	32.03	3.502	30.02	29.75	3.492	29.91	29.96
18:32	6.05	34.86	35.20	4.023	35.23	34.93	4.005	35.05	35.3
11:08	6.04	34.93	35.10	4.014	35.14	35.10	4.027	35.27	35.5
12:34	5.39	40.15	40.50	4.552	40.52	40.50	4.565	40.65	40.77
13:28	6.48	31.79	31.9	3.688	31.88	31.7	3.687	31.87	31.83
14:20	7.60	24.88	24.91	2.991	24.91	24.68	2.981	24.81	24.6
19:26	8.84	18.58	18.5	2.351	18.51	18.2	2.328	18.28	17.8

\* "left" is the combination of Weathermeasure readout 1125 and probe 1319;  
 "right" is the combination of readout 1193 and probe 1851.

in less than a 0.4 ppm change in a measured length.

#### 2.3.4. STATIC CALIBRATIONS

Temperature readings from the USGS and GSC temperature sensors were compared with an Hg thermometer in a temperature controlled airbath in an attempt to determine the scale and calibration error of the sensor. Although the temperatures from the probes agreed fairly well, they varied considerably from the temperatures measured by a mercury thermometer. Results from the tests are disappointing; their validity is questionable due to a possible temperature gradient within the enclosure containing the sensors.

For the tests the sensors were extracted from the probes and sealed into a brass enclosure, which was placed in a temperature controlled circulating water bath. The top surface of the enclosure was exposed to the air and an Hg thermometer was inserted into the enclosure from the top. Each time the temperature of the water bath was changed,

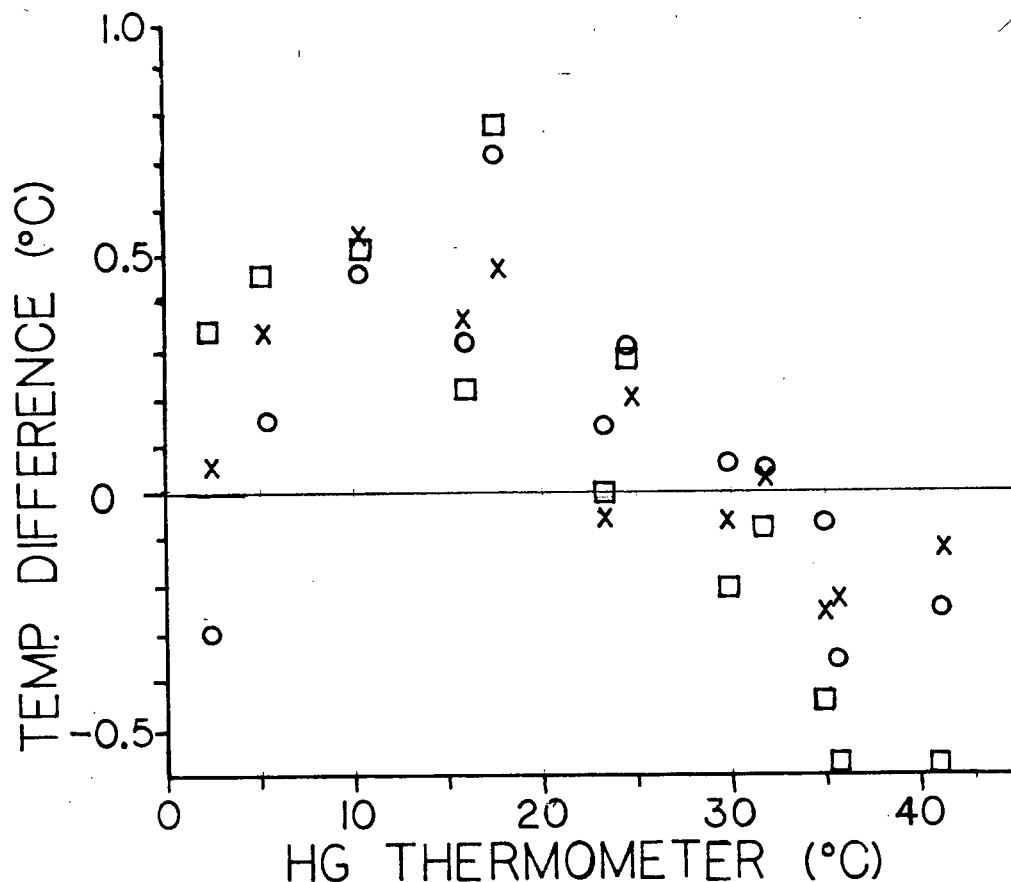


**Figure 2.8.** Air bath temperature differences between the probes' sensors and an Hg thermometer vs the Hg thermometer temperature. The square marks readings from USGS thermistor C1, the X's readings from the combination of CGS readout 1193 and probe 1851, and the O's readings from the combination of readout 1125 and probe 1319.

a minimum of 30 minutes was allowed for the temperature in the water bath and the air within the enclosure to stabilize. At each temperature, during a minimum time interval of 10 minutes, at least 3 readings of each sensor and the thermometer were made. The readings are listed in Table 2.5.

The temperature differences (Hg thermometer—probe sensor) are seen to be positive at low temperatures and negative at high temperatures with the crossover at about 30°C (Figure 2.8). The difference is as much as 0.5°C near 5° and 35°C. Repeated measurements at 15°, 25°, and 35°C show large variations with differences as large as 0.6°. The poor repeatability indicates some problem in the test procedures or in the equipment. The

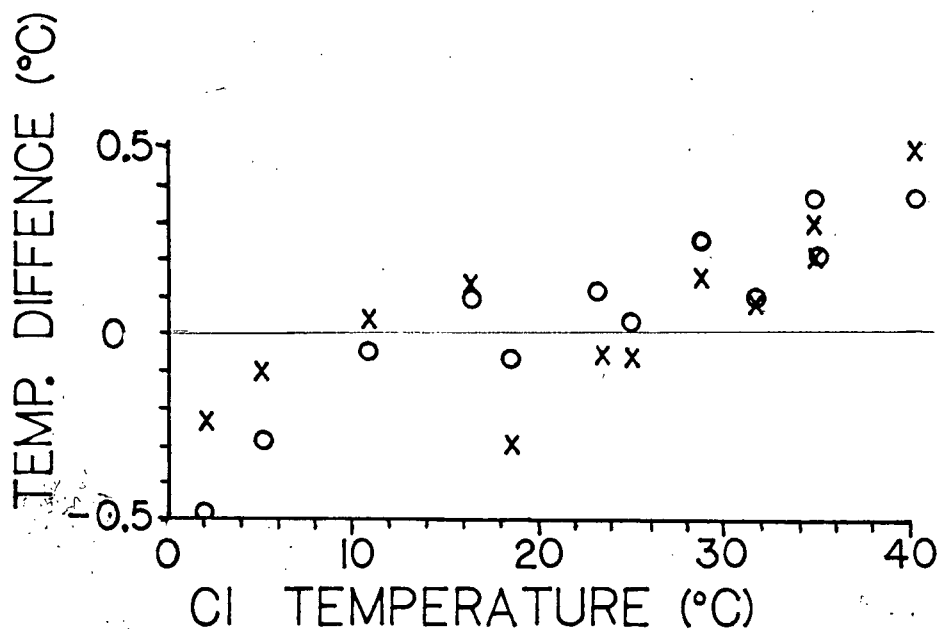


**Figure 2.9.** Air bath temperature differences between the CGS sensors and USGS thermistor CI. Symbols and ID's the same as in Figure 2.8.

consistent agreement between the USGS and GSC sensors makes the Hg thermometer temperatures suspect, however, plausible mechanisms, such as temperature gradient within the air bath or a stem correction for the exposed part of the thermometer stem, would only increase the temperature difference.

Discounting the Hg thermometer readings, the GSC sensors and the USGS thermistor are compared. This, of course, assumes that the sensors were not subject to the conditions that caused the Hg thermometer to err. Figure 2.9 shows the temperature difference plotted as a function of temperature. The plot shows a linearly increasing temperature difference. Some of the differences are erratic, but the agreement is within about  $\pm 0.2^\circ$  from  $5^\circ$  to  $35^\circ$ . Between  $4^\circ$  and  $10^\circ\text{C}$ , the range of temperatures which were recorded during the Gold River survey, the temperature difference is negative. This is opposite of the differences observed in the average temperatures from the flown profiles (See Figure 2.5).

The inconsistencies observed in the tests make the results unsuitable for determining

the calibration and scale errors for the probes. A positive result of the test is the agreement between the temperature displayed by the Weathermeasure readout unit and that derived from the voltage output of the unit. These two values are nearly the same for the left probe, and differ by  $-0.1^{\circ}\text{C}$  for the right probe.

### 2.3.5. DYNAMIC AIR TEMPERATURE TESTS

Wind tunnel tests and a field test were made in an attempt to determine the proportion of the full adiabatic temperature rise recovered by the GSC probe. The full adiabatic temperature rise is proportional to the square of the true airspeed (equation 2.15). A plot of the temperature rise as a function of true airspeed for recovery factors of 1.0 and 0.6 are shown in Figure 2.10.

To determine the recovery factor, both the temperature of the unperturbed air (*i.e.*, the static temperature) and the true airspeed must be known. Using a recovery factor of 0.6, the value empirically determined for the USGS probe, velocities greater than 15 m/s are needed to give a temperature rise of  $0.1^{\circ}\text{C}$ .

Tests in the wind tunnel at U.B.C. were limited to a maximum airspeed of 23 m/s. At this velocity the temperature rise in a probe with a recovery factor of 0.6 is  $0.15^{\circ}\text{C}$ . Thus, velocities are not adequate to determine the recovery factor, but they do provide another temperature comparison between the sensor systems and the Hg thermometer.

The tests were made in a wind tunnel with a cross sectional area of about  $16\text{ m}^2$ . A probe provided by the USGS and a GSC probe, a Hg thermometer, and a pitot tube were mounted near the center of the wind tunnel. The thermometer was placed on the insulated lee side of the mounting support for the probes and was read through a pair of binoculars. The true airspeed was calculated from manometer readings of the pitot tube. The test results are summarized in Figure 2.11 with plots of the difference between sensor recorded temperatures and Hg thermometer temperatures versus the true airspeed.



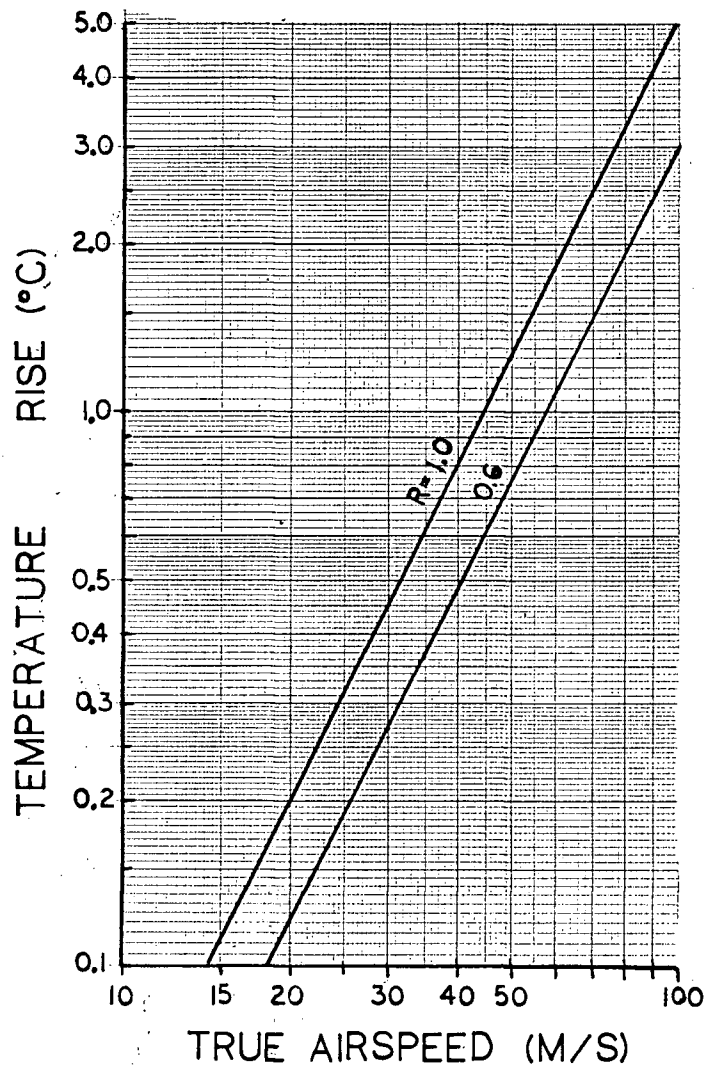


**Figure 2.10.** Kinetic temperature rise for recovery factors of 1.0 and 0.6 vs true airspeed in m/s.

Over the entire range of airspeeds there is good agreement between the sensors and the Hg thermometer. The sensors diverge from the theoretical temperature rise assuming a recovery factor of 0.6 at the higher velocities, but the difference is less than the possible reading error for the Hg thermometer. The recovery factor may vary at higher velocities if the flow regime changes from laminar to turbulent, because there would be extra dissipation of energy in a turbulent airflow [Hilton, 1938].

A field test was made to determine the recovery factor for the GSC probe. Wet and dry bulb temperature measurements were made on a lookout tower to provide the static

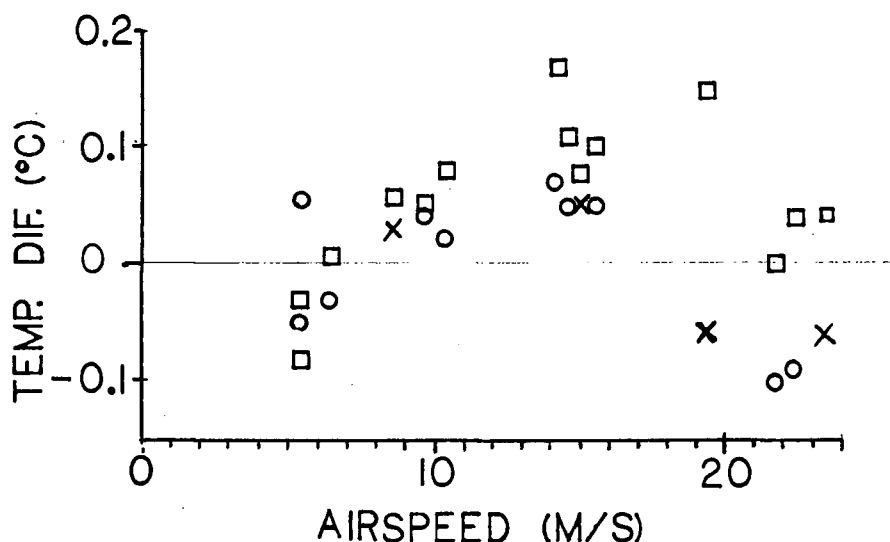


**Figure 2.11.** Temperature difference between probes and an Hg thermometer as a function of the airspeed in the UBC wind tunnel. Symbols and ID's are the same as in Figure 2.8.

air temperature, and temperature and humidity readings were made as a probe equipped helicopter flew over the tower. Only a limited range of airspeeds (41 to 54 m/s) were used during the test. Using equation (2.5) the recovery factor may be computed from the static temperature, probe temperature, and the true airspeed.

The recorded data and the corresponding computed recovery factors are listed in Table 2.6. The average value for the recovery factor from these tests is  $0.20 \pm 0.18^\circ \text{Cs}^2/\text{m}^2$ . For the GSC probe, any recovery factor lower than 0.6 will increase the temperature differences relative to the USGS probe recorded in the profiles (Figure 2.5). This fact along with the uncertainty of the calculated average recovery factor make the Metcalf tower test results suspect.

The humidity measurements, however, agree well with the differences observed in the profiles (Figure 2.6). During the tower tests the GSC probe consistently measured the humidity about 10% lower than the value calculated from the wet and dry bulb readings in the tower.

**Table 2.6.** Metcalf Tower tests of helicopter mounted CGS probe

Tower		Comp. Hum. %	Probe Temp. (°C)	Probe Hum. %	Airspeed (m/s)	Recovery Factor
Dry (°C)	Wet (°C)					
18.4			18.5		54	0.1
18.9			18.8		54	0.1
18.9			18.7		51	0.2
18.5			18.8		53	0.2
18.1			18.6		54	0.3
18.4			18.8		54	0.3
18.7			18.6		49	-0.1
18.7			18.6		49	-0.1
18.5	16.8	84	18.6	71	49	0.1
18.8	16.8	82	18.8	72	41	0.0
18.3	16.5	83	18.8	72	50	0.4
18.3	16.5	83	18.9		49	0.5
18.4	16.6	83	18.7	72	45	0.3
18.7	16.7	82	18.8	72	45	0.1
18.7	16.7	82	18.7	72	44	0.0
18.4	16.6	83	18.8	72	45	0.5
18.4	16.6	83	18.8	72	45	0.4
18.7	16.7	82	18.9	72	45	0.2
18.9	16.8	81	19.1	71	53	0.1
18.7	16.7	82	19.2	70	54	0.4

## 2.4. PRESSURE

The average refractive index used to correct a measured length is obtained from an integrated average of the refractive index at the "midpoint" of adjacent temperature-humidity readings. The air pressure readings are not made by the aircraft flying the line, instead they are calculated from the pressure at the instrument end of the line. The procedure uses the total air pressure readings at the instrument station, the station elevations, the estimated beam curvature, and the temperature and humidity profiles to construct a profile of the air pressure; details are discussed in Appendix B. The calculated average pressure, and the resulting refractive index scale correction is then somewhat dependent on the station elevations. Incorrect station elevations produce a scale error in a

measured distance of 0.03 ppm/m of error. This error has no effect on the calculated strain based on observed distance changes, provided that the same relative elevation difference is used to reduce each of the measurements.

Pressure readings made at the reflector end of the line are not used in the refractive index calculation, but are used only to check the calculated value. A difference between the observed and calculated pressure at the reflector end may arise from imprecise station elevations, instrumental error, or modeling error.

During the 1982 Gold River survey, pressure readings at the instrument end of a line were made with two Bell and Howell Model 4-461 digital pressure transducers, and a Wallace and Tiernan FA-181 0-7,000 ft altimeter. Pressure readings at the reflector end were made with a Wallace and Tiernan altimeter. The mean of corrected readings taken at the beginning, middle, and end of each line measurement was used in the refractive index calculation.

Corrections for the pressure instruments were obtained from calibrations performed by the Division of Mechanical Engineering of the National Research Council in April of 1982. Calibration curves for the pressure instruments used in the Gold River survey may be obtained from the GSC.

The pressure instruments were compared at the end of each day that distance measurements were made in the Gold River survey. These intercomparisons are listed in Table 2.7. The pressures agree well with the spread of all readings being less than 0.03 inch (0.09 kPa or 0.9 mb) in any given day.

Field measurements are also used to compare the instruments. Table 2.8 lists actual and corrected pressure readings from the instrument and reflector barometers, and the calculated reflector pressures computed from the instrument pressure readings (see Appendix B). The instrument and reflector altimeter pressures are in good agreement with the corresponding pressures from B&H transducer 2130. Pressures from B&H transducer

**Table 2.7.** Motel Pressure Comparisons During the 1983 Gold River Survey

Date mo/da	B&H #2145	B&H #2130	Alt #59-13	Alt #301038	Alt #765
7/15	29.55	29.57		29.58	
7/17	29.49	29.52	29.55	29.55	29.54
7/18	29.59	29.61		29.63	29.62
7/19	29.60	29.59	29.62	29.62	29.61
7/20	29.59	29.61		29.61	29.61
7/21	29.79	29.79	29.85	29.81	29.80
7/22	29.97	29.97		29.99	29.99

All reading given in inches of Hg the unit of the B&H transducers.

2145 are generally about 0.03 inch lower than those from the other barometers. For that reason, pressures from B&H transducer 2130 were used exclusively to reduce the measured distances.

The agreement between the calculated and measured pressure at the reflector indicates that relative elevation control is good and that the algorithm used to calculate the pressure profile provides a good approximation of the actual pressure.

**Table 2.8.** Observed and Calculated Pressures\* during the Gold River survey

Instrument Station					Reflector Station		
Line No. **	Date mo/da	B&H ID #2145	B&H ID #2130	Alti-meter #765	Alti-meter #30138	Calcu-lated #2145	Calcu-lated #2130
1	7/17	24.72	24.73	24.77	25.33	25.34	25.35
2	7/17	24.73	24.77	24.77	24.33	24.29	24.33
3	7/17	24.74	24.77	24.77	24.37	24.33	24.37
4	7/17	24.75	24.78	24.78	24.40	24.37	24.39
5	7/17	25.33	25.37	25.36	24.32	24.30	24.32
6	7/18	25.33	25.37	25.37	24.38	24.35	24.39
7	7/18	25.33	25.37	25.38	24.41	24.37	24.41
8	7/18	25.35	25.38	25.39	25.41	25.37	25.40
9	7/18	25.35	25.39	25.40	26.48	26.43	26.47
10	7/18	25.36	25.40	25.40	26.29	26.25	26.28
11	7/18	24.79	24.82	24.82	26.29	26.26	26.29
12	7/18	24.78	24.81	24.81	26.48	26.44	26.46
13	7/18	24.77	24.79	24.81	26.09	26.04	26.07
14	7/18	24.77	24.79	24.80	25.41	25.37	25.39
15	7/20	24.32	24.35	24.35	24.33	24.30	24.33
16	7/20	24.26	24.28	24.29	24.33	24.31	24.33
17	7/20	24.27	24.30	24.30	24.36	24.33	24.36
18	7/22		25.62	25.62	24.61		24.61
19	7/22		25.64	25.64	26.33		26.33
20	7/22		25.66	25.65	26.73		26.74
21	7/22		25.64	25.64	26.53		26.52
22	7/22		26.69	26.71	26.50		26.50
23	7/22		26.69	26.69	26.29		26.30

\* All pressures given in inches of Hg the units of the B&H transducers.

\*\* Line number refers to the sequential order that observations were made during the Gold River survey.

## 2.5. THE ACCURACY AND PRECISION OF A DISTANCE

The theoretical error in a distance measurement may be estimated from the contributions to the constant and scale error. The major components of the constant error are pointing error, zero error, non-linearity in the phase detector, receiver noise, zero-crossing error due to signal level, and centering. Scale error results from short and long term drift

in the modulation frequency and error in the calculated mean refractivity.

### 2.5.1. CONSTANT ERROR

It is assumed that pointing error is not a factor in long line measurements, and that error from the zero crossing detector is minimized by careful adjustment of the signal level during range measurements. No tests were made to determine the non-linearity in the phase detector (cyclic error), and a value of  $\pm 3.5$  mm is used based on the manufacturers specification  $\pm 5$  mm amplitude cyclic error (the RMS error is used). Zero error, or error in the instrument and reflector constants, is estimated from the standard deviation of the Victoria baseline measurements to be  $\pm 4$  mm. Receiver noise (see section 2.2) is given by *Berg et. al.*, [1981] to be  $\pm 2$  mm. Extreme care taken in centering both the instrument and reflectors reduce centering error to less than 0.5 mm. Assuming that these error are random, the theoretical constant error is

$$\sigma = \sqrt{(3.5 \text{ mm})^2 + (4 \text{ mm})^2 + (2 \text{ mm})^2 + (0.5 \text{ mm})^2} = \pm 5.7 \text{ mm}$$

Careful calibration might reduce the contributions of non-linearity and zero error to as little as 1 mm.

### 2.5.2. SCALE ERROR

The tests of the short and long term stability of the modulation frequency show drift to be less than 0.05 ppm. Error in the average refractivity arise from temperature, water vapor pressure, and total pressure error. The partial derivatives of the group refractive index with respect to the desired meteorological parameter defines the error limits on the measurement for a desired accuracy (see equation A.12). *Savage and Prescott* [1973] estimate  $\pm 0.1^\circ\text{C}$  and  $\pm 0.3$  kPa for the standard deviation of the mean temperature and water vapor pressure for atmospheric profiles measured with the USGS probe. The resulting scale error in a distance is 0.1 ppm due to temperature and 0.1 ppm due to the water vapor pressure.

The standard error in the average pressure is estimated from the agreement between the altimeter and B&H digital barometers to be  $\pm 0.03$  kPa (0.01 in Hg). It is noted, however, that the B&H units differed by as much as 0.12 kPa (0.04 in. Hg) during the Gold River survey, but this difference is attributed to the malfunction of one of the units. The resulting theoretical scale error for lines reduced with the USGS probes, assuming random values for the components, is

$$\sigma = \sqrt{(0.1 \text{ ppm})^2 + (0.1 \text{ ppm})^2 + (0.1 \text{ ppm})^2 + (0.1 \text{ ppm})^2} = \pm 0.2 \text{ ppm}$$

The scale error using the GSC probes is not as well defined. The uncertainty about the airspeed correction makes any comparison with the USGS probes tentative. In addition, no tests were made to check the linearity or stability of the readout unit for the Weathermeasure probe. The absolute temperature calibration for the probe is not known, but the agreement with the USGS thermistor in the U.B.C. wind tunnel suggests that at room temperature it is within the  $\pm 0.1^\circ\text{C}$  error of the USGS thermistor. If we assume the airspeed correction for the GSC probe is the same as that used for the USGS probe, the average temperatures from the simultaneous profiles differ by  $0.3^\circ\text{C}$ . Weathermeasure lists accuracy of  $\pm 0.2^\circ\text{C}$  for the temperature sensor used in the GSC probe. The scale error in a distance due to a  $0.2^\circ\text{C}$  error in temperature is  $\pm 0.2$  ppm. The difference in the average water vapor pressure from the simultaneous profiles is less than 0.3 kPa, within the possible error of the USGS probe. The scale error in a distance due to a 0.3 kPa error in the water vapor pressure is  $\pm 0.1$  ppm. Taken together, the estimated standard error in the scale correction for lines reduced with the CGS probes is

$$\sigma = \sqrt{(0.2 \text{ ppm})^2 + (0.1 \text{ ppm})^2 + (0.1 \text{ ppm})^2 + (0.1 \text{ ppm})^2} = \pm 0.26 \text{ ppm}$$

Combining the constant and scale error, the standard error of a distance  $L$  (m) reduced with the USGS probe is estimated to be

$$\sigma(\text{m}) = \sqrt{(0.0057)^2 + (0.2 \times 10^{-6})^2 L^2} \quad (2.7)$$



For distances reduced with the CGS probe, the scale factor is increased to  $0.26 \times 10^{-6}$ .

The residuals obtained from the adjustment for station positions provide an estimate for the precision of a measurement, but yields no information concerning the accuracy of the survey. If we include only lines with aircraft-flown refractivity and weight all measurements equally, the residuals give 5 mm as the standard deviation of a length. With an average length of 24 km, 5 mm is less than the estimated standard error of 7.5 mm from equation 2.7. The estimated standard error, however, must be modified to make the comparison valid. The instrument and reflector constants are not likely to change during a single survey, reducing the constant error in equation 2.7 to 4.1 mm. The resulting estimated standard error in a 24-km length is 6.3 mm, in better agreement with that obtained from the adjustment.

## 2.6. RECOMMENDATIONS

### 2.6.1. DISTANCE METER

The following simple field tests described by *Berg et al.* [1981] to check the instrument sensitivity, the zero-crossing detector, and the pointing error should be made to verify instrument operation.

1. To test instrument sensitivity, place an ND6 neutral density filter on the collimator, and range to a single reflector at short range. (Take note of the maximum signal meter deflection for future reference.) When sensitivity is normal, it should be possible to obtain ranges.
2. To test the zero-crossing detector, take measurements at the upper and lower limits of acceptable signal level as indicated by the panel meter. A span of more than 5 mm indicates a need for readjustment of the zero-crossing detector.
3. To test the pointing error, the returned beam is rotated through six positions in the receiving optics, and the distance measurements compared. The position of the

returned beam may be found by inserting a piece of paper in front of the receiver. A span of greater than 10 mm indicates optical misalignment.

4. The instrument calibration at the Victoria baseline should include measurements for the linearity. This requires establishing a linearity baseline of 10 monuments spaced 1 m apart. In addition, more of the distances in the baseline should be observed. To reduce refractivity error, the baseline rangings should be made, if possible, on overcast, light or moderately windy days.
5. All baseline calibrations should be made to a calibrated single reflector and mount. All other reflector-mount constants are referenced to this standard. This allows separation of the instrument and reflector constants. The physical arrangement of the reflectors in the 16-reflector mount makes its use on short baseline calibrations difficult, since at least two of the center positions have to be filled to obtain axial symmetry.
6. If possible, the modulation frequency should be checked prior to and immediately after each measured line.

### **2.6.2. PROBES**

Additional tests are needed to establish the accuracy of the CGS probe. It is recommended that:

1. The voltage output from the Weathermeasure probe be checked over a range of battery voltages and ambient temperatures. The calibration box provides a convenient constant input.
2. The response-time delay of the probe should be checked with the filter caps on and off. The filters should be cleaned often.
3. The recovery factor (airflow velocity related temperature rise) for the probe unit should be measured at the Rosemount Inc. wind tunnel. Rosemount Inc. manufactures total temperature probes and has a wind tunnel equipped with reference thermometers

for use in high airflow velocities. Additional tests, possibly with a total temperature probe, should be made in the field to determine possible corrections due to mounting location or type of aircraft used. *Berg et al.* [1981] use slightly different airspeed corrections for different models of helicopters.

4. The effect of airspeed on the GSC probe humidity sensors needs to be determined. The GSC probe measured the relative humidity about 10% lower than the USGS probe (Figure 2.6) and a psychrometer (Table 2.6).

Other alternatives to the above tests are to use a USGS design probe, or to build a probe incorporating a Rosemount total temperature thermometer. Use of the Rosemount thermometer would eliminate the uncertainty in the airspeed correction, increase the long term stability, and reduce the size of the externally mounted equipment. Use of the USGS probe complicates the recording and reduction of the readings, but its stability is established.

### **2.6.3. PRESSURE**

1. A pressure-transfer standard that does not go into the field should be used to calibrate the pressure devices at the end of the working day. This standard should be calibrated frequently with an Hg barometer, or some other pressure reference device.
2. A more transportable and field worthy pressure sensor, such as an AIR-HB-1A barometer, should be obtained to replace the B&H digital barometer. The B&H unit, however, would make a good pressure transfer standard.

Atmospheric Instrumentation Research, Inc.  
1880 South Flatiron Court  
Boulder, CO 80301 USA

(303) 443-7187

3. Intercomparisons between the altimeters and field barometers should continue.

## 2.7. STRAIN RESOLUTION

Remeasurement of a trilateration network can be used to determine deformation within the area covered by the network. The relative displacement of stations within the network results in a change in the distance between the stations. The ratio of the change in the length of a repeated distance measurement to its length ( $dL/L$ ) defines its extension. The extension of a line with the approximate azimuth  $\theta$  (measured clockwise from north) is related to the surface strain tensor  $\epsilon_{k,l}$  through the tensor transformation law

$$\frac{dL}{L} = e = \epsilon_{k,l} \beta_{k,l} \beta_{l,k} \quad k, l = 1, 2 \quad (2.8)$$

where  $\beta_{k,l}$  are the direction cosines of the line relative to a geographic coordinate system with the 1-axis east and the 2-axis north. The full expression of this equation for  $e_i$ , the extension of the  $i^{th}$  line with azimuth  $\theta_i$ , is

$$e_i = \epsilon_{11} \sin^2 \theta_i + 2\epsilon_{12} \sin \theta_i \cos \theta_i + \epsilon_{22} \cos^2 \theta_i \quad (2.9)$$

Three or more measured extensions allow solution for the average surface strain tensor components  $\epsilon_{11}$ ,  $\epsilon_{12}$ , and  $\epsilon_{22}$ . Assuming uniform strain within a network with  $n$  measured extensions that have with the standard deviation  $\sigma$ , the standard deviation in  $\epsilon_{11}$  and  $\epsilon_{22}$  are about [Savage, 1983]

$$\sigma \sqrt{4/N} \quad (2.10)$$

and the standard deviation in  $\epsilon_{12}$  is about

$$\sigma \sqrt{2/N} \quad (2.11)$$

The extensions are derived from the comparison of two surveys, and miscalibration of the instrument or meteorological sensors in either survey will result in a systematic error. A systematic error distorts the derived strain field, producing an apparent dilatational

strain ( $\Delta = \epsilon_{11} + \epsilon_{22}$ ) about twice as large as the scale error. The standard deviation of the normal components  $\epsilon_{11}$  and  $\epsilon_{22}$  would need to be increased to compensate for such an error, but any calculated shear strain would be unaffected. A constant error, such as an incorrect zero constant, produces a similar effect if the lines used in the calculation are about the same length.

Assuming no systematic error, the standard deviation of a measured extension for an average line (24 km) in the Gold River network is 10.5 mm or 0.44 ppm (*i.e.*,  $\sqrt{2}\sigma$  from equation 2.7). Assuming uniform strain, the strain resolution of the Gold River network is estimated by (2.10) and (2.11) to be 0.18  $\mu$ strain in the normal strains and 0.13  $\mu$ strain in the tensor shear strain. Accumulated extensional strain exceeding 0.4  $\mu$ strain or accumulated tensor shear exceeding 0.3  $\mu$ strain is detectable at a 95% confidence level. If the deformation of the network is reasonably uniform in time, a resurvey after 2 years will resolve the rate of strain accumulation at the 0.2  $\mu$ strain level, and after 5 years at the 0.1  $\mu$ strain level. A typical rate of strain accumulation in tectonically active areas is 0.2  $\mu$ strain/yr [Savage, 1983]. As will be shown later, the rate of strain accumulation in the Gold River network appears to be at or below 0.2  $\mu$ strain/yr. A resurvey of the Gold River network after a five-year interval could determine whether strain is accumulating at the 0.2  $\mu$ strain/yr level in this area.

### 3. 1947 TRIANGULATION

Baseline measurements for the Gold River network are from a triangulation survey conducted by Slocomb and Swinnell of the B.C. Ministry of Surveys in 1946 and 1947. The angles were probably observed with an early T2 (a 1" direction theodolite), but the field procedures are not known [G.A. Wilkenson, B.C. Ministry of Surveys, personal communication]. I extracted the angles from copies of the field notebooks provided by Herb Draggert of the Department of Energy, Mines, and Resources, and from abstracts provided by G.A. Wilkenson. A typical angle measurement was comprised of 10 sets of forward and reverse pointings. Angles appear to have been measured individually, rather than in a round. Sightings were to both targets and cairns, with all measurements apparently made during daylight hours.

The subset of the 1946-47 triangulation survey that includes all monuments common to the 1982-83 trilateration survey is shown in Figure 3.1. An abstract of the observed angles is given in Table 3.1. This subset contains 57 angles between 10 stations. Most of the angles in Table 3.1 were directly observed, but because the survey includes several stations outside of the Gold River network some are derived from the sum or difference of angles to an intermediate station. These angles are identified by a dual number in the columns for "sets" and "spread" in Table 3.1. As can be seen in the "σ" column, the standard deviation of the mean of 10 sets of pointings varies between 1.2" and 6.4", with a mean value of  $4.5 \pm 1.2''$ . Assuming random error and a standard error of 4.5" in a single set, the standard error of the mean of  $n$  sets is  $4.5''/\sqrt{n}$  or 1.4" for 10 sets. The standard error of an angle derived from the sum or difference of angles is the square root of the sum of the squares of the individual standard errors. The actual standard error in an observed angle is likely to be larger than this estimate, because the principal source of error in a horizontal angle is lateral refraction [Bomford, 1980, p. 32]. The mean of a

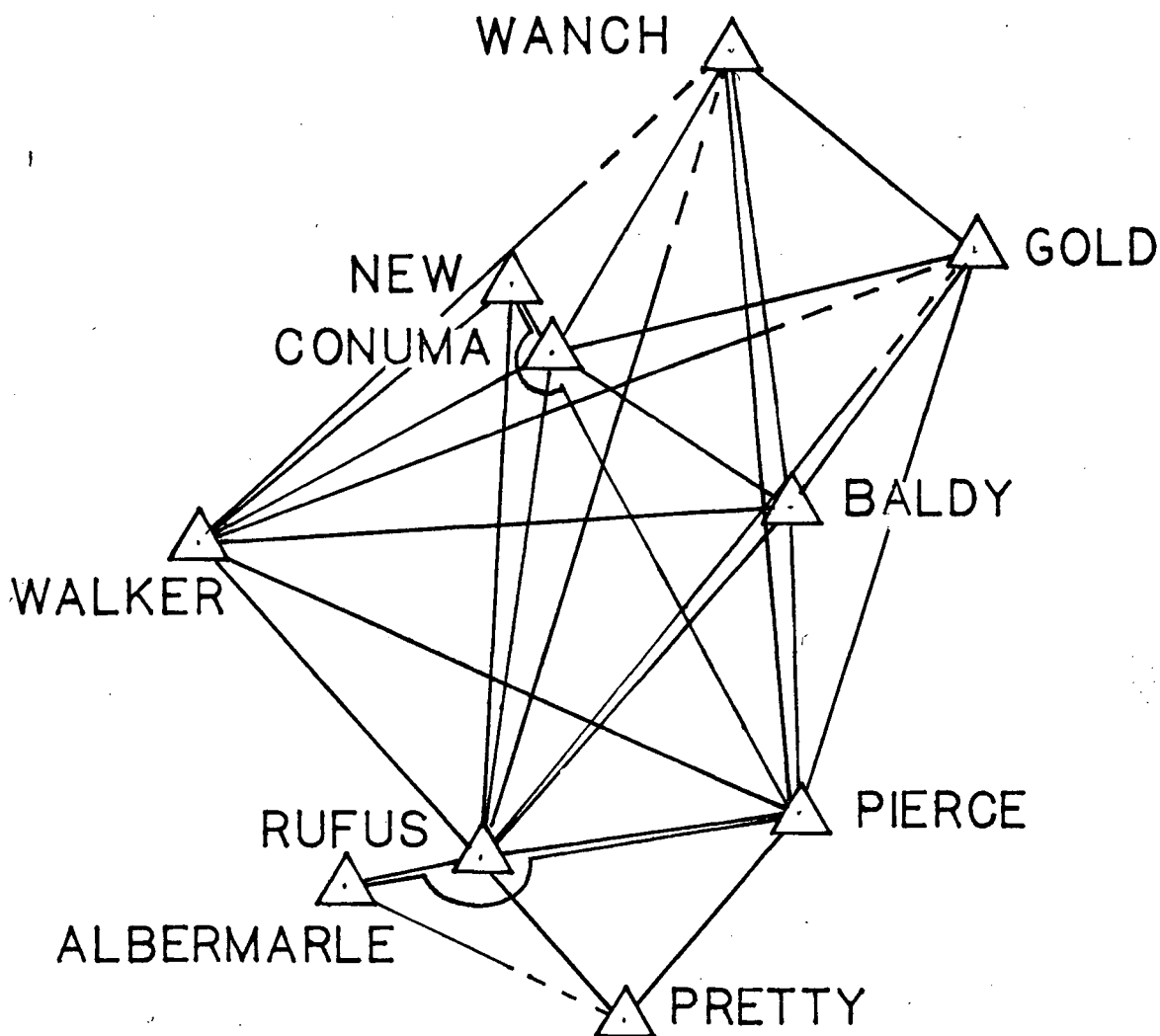


**Figure 3.1.** Sketch showing directions enclosing horizontal angles observed by the B.C. Ministry of Surveys during the 1946-47 triangulation survey. The solid line indicates that the directions were observed from both stations. The line is dashed at the end near the station measured for one way direction observations.

number of sets that are observed within a relatively short time might have a small standard deviation, but the error due to horizontal refraction may be much greater. The effects of horizontal refraction can be reduced by making the observations at night or by spacing the observations evenly over the day. An estimate of the standard error of an observation that includes possible error from horizontal refraction is obtained from the geometrical constraints inherent in a triangulation survey.

**Table 3.1. 1947 Triangulation**

Instrument Station	Target Station 1	Target Station 2	Angle ° ' "	Sets	Spread "	$\sigma$ "	Change 82-47	
Albermarle	Rufus	Pretty G	36 37 42.3	10	15	5.0	-1.5	
Baldy H	Pierce	Rufus	45 04 18.5	10	17	5.1	5.2	
	Rufus	Walker	44 59 07.1	10	9	2.6	1.0	
	Walker	Conuma	33 44 28.5	10	22		0.2	
	Conuma	Wanch	49 36 26.4	10	17	6.4	-3.3	
	Wanch	Gold	44 51 28.7	10	18	6.3	1.8	
	Gold	Pierce	141 44 09.5	10	16	5.4	-3.6	
	Conuma	Gold	94 27 52.8	10	11	4.2	0.9	
Conuma	Wanch	Gold	47 30 11.7	10	10	3.2	-0.6	
	Gold	Baldy H	45 07 54.8	10	18	6.0	1.9	
	Baldy H	Pierce	29 03 14.6	10	17	4.7	0.7	
	Pierce	Rufus	38 12 08.5	10	17	5.4	-1.7	
	Rufus	Walker	54 58 25.8	10	14	4.5	-0.8	
	Walker	New	92 18 27.1	10/5*	9/5*	2.8	-3.3	
	Walker	Wanch	145 08 12.2	10/10	12/9	5.2	-7.0	
Gold	Pierce	Baldy H	18 51 53.0	5	3	1.2	0.4	
	Baldy H	Conuma	40 24 10.5	10	12	4.7	-0.2	
	Conuma	Wanch	52 43 46.8	10	15	4.5	-6.3	
New	Conuma	Walker	75 40 15	5	8		6.4	
	Pierce	Rufus	32 54 42.8	7	25		3.6	
	Rufus	Walker	47 29 01	5	8		2.8	
Pierce	Pretty G	Albermarle	42 16 22.9	10		4.6	2.8	
	Pretty G	Rufus	42 59 16.9	10		3.9	-1.0	
	Rufus	Walker	32 03 40.6	10	12	4.6	3.0	
	Walker	Conuma	35 40 42.0	10	7	2.5	0.9	
	Rufus	Conuma	67 44 24.4	10	10		2.1	
	Conuma	Baldy H	27 08 48.5	10	9		-3.8	
	New	Baldy H	26 23 14.0	5	11		-3.4	
	Baldy H	Gold	19 24 01.8	10	12		-0.7	
	Conuma	Wanch	23 09 15.4	10	12		2.2	
	Wanch	Gold	23 23 31.1	10	10		-2.9	
Pretty G	Rufus	Pierce	80 21 35.6	10	12	4.5	-1.5	
Rufus	Albermarle	Walker	59 14 59.2	5	17		-2.1	Rej.
	Walker	New	44 29 42.6	5	11		-2.0	
	Walker	Conuma	49 01 31.5	10/10	9/14		2.8	
	Walker	Pierce	123 05 05.4			6.1	-3.3	
	Conuma	Wanch	8 19 43.8	10/10	14/15		-0.9	
	Conuma	Gold	31 18 10.1	10	15		0.4	



**Table 3.1.** 1947 Triangulation (continued)

Obs Sta	Sta 1	Sta 2	Angle ° ' "	Sets	Spread (s)	$\sigma$ (s)	Change 82-47	
Rufus	Conuma	Baldy H	34 01 02.9	10	12	3.8	-0.9	
	Baldy H	Pierce	40 02 30.1	10	19	5.0	-4.2	
	Gold	Pierce	42 45 12.8	10	16		4.5	
	Pierce	Pretty G	56 39 10.9	10	12	4.8	0.2	
	Pretty G	Albermarle	121 00 54.0	10/10	13/14	6.3	-4.4	
	Albermarle	Pierce	182 19 56.0	10/10	11/17		3.2	
Walker	Wanch	Conuma	16 36 17.7	10	13		-6.7	Rej.
	Wanch	New	4 34 56.0	10/5	7/17		-0.1	
	Conuma	Rufus	75 59 59.2	10	13	3.8	2.6	
	Conuma	Pierce	51 08 45.2	15	20		1.6	
	Conuma	Baldy H	24 01 45.5	15	27		-0.7	
	Baldy H	Pierce	27 07 03.7	10	16	5.0	-1.8	
	Pierce	Rufus	24 51 16.1	15	17		-1.0	
	Gold	Pierce	44 26 45.6	10	14		2.7	
Wanch	Gold	Baldy H	42 00 40.7	10	7	2.6	-1.3	
	Baldy H	Conuma	37 45 28.2	10	10	3.9	1.7	
	Pierce	Rufus	23 22 39.6	5	18		-6.9	Rej.
	Pierce	Conuma	35 09 22.3	10	9		-1.9	
	Conuma	Walker	18 15 41.3	15	12		3.1	

\* Two values indicate the angle was derived from the sum or difference of angles to an intermediate station.

The standard error of an observed angle may be approximated from the root-mean-square triangle closure (see *Bomford*, [1980])

$$\sigma = \left( \frac{\Sigma \epsilon^2}{3n} \right)^{1/2} = 0.72\epsilon_m \quad (3.1)$$

where  $\epsilon$  is the individual triangle closure corrected for spherical excess and  $n$  is the number of closures;  $\epsilon_m$  is the mean triangle closure without regard to sign. The 18 triangle closures listed in Table 3.2 give 1.9" for the standard error in an observed angle. Some of the angles are actually the sum of two adjacent angles and the standard error from the root-mean-square triangle closure may be overestimated.

**Table 3.2.** 1947 Triangle Closure

Sta 1	Sta 2	Sta 3	Spherical Excess "	Observed Closure "	Cor. Closure
Wanch	Gold	Baldy H	0.7	6.7	6.0
Wanch	Baldy H	Conuma	0.7	1.1	0.4
Wanch	Gold	Conuma	0.8	7.4	6.6
Conuma	Gold	Baldy H	0.6	-1.9	-2.5
Conuma	Baldy H	Walker	0.6	2.9	2.3
Baldy H	Pierce	Walker	1.2	2.8	1.4
Conuma	Baldy H	Pierce	0.4	-2.8	-3.2
Conuma	Pierce	Walker	1.4	1.5	0.1
Conuma	Baldy H	Rufus	0.9	1.6	0.7
Baldy H	Rufus	Walker	1.4	1.3	-0.1
Conuma	Rufus	Walker	1.1	-3.5	-4.6
Baldy H	Pierce	Rufus	0.7	1.5	0.8
Conuma	Pierce	Rufus	1.1	4.4	3.3
Pierce	Pretty G	Rufus	0.4	2.5	2.1
Gold	Pierce	Baldy H	0.4	4.3	3.9
Gold	Conuma	Pierce	1.5	-0.2	-1.7
Pierce	Rufus	Walker	0.8	2.1	1.3
Walker	Conuma	Wanch	0.6	11.2	10.6

The closure of three triangles in Table 3.2 exceeds 5", and a survey blunder or transcription error is suspected. The geometrical constraint of triangle closure provides no clues to determine which angle is in error. On the other hand, if the positions of the survey stations are overdetermined by the observations, a network adjustment will identify particular angles that do not fit the geometrical constraints. A weighted, variation-of-coordinates adjustment [Bomford, 1980] determines the most probable position of the stations. The residuals from the adjustment (*i.e.*, the difference between an observed and an adjusted angle) give an estimate of the standard deviation of an observed angle and aid in identifying possible blunders. Assuming random error, the standard deviation of an

angle is given by

$$\sigma_a = \left( \frac{\sum wx^2}{w_m c} \right)^{1/2} \quad (3.2)$$

where  $w$  is the weight of each angle (the weight is the inverse square of the standard error),  $x$  is the residual,  $w_m$  the mean of the weights, and  $c$  the number of degrees of freedom [Bomford, 1980, p. 188]. In the Gold River adjustments the weights are based on the number of sets and are normalized by the estimated standard error in a measurement with 10 sets. An angle that is the mean of 10 sets has a weight of 1.0, one that is the mean of 5 sets has a weight of 0.5, and angle that is derived from the sum or difference of two angles that are the mean of 10 sets has a weight of 0.5.

The unknowns in the adjustment are the latitude and longitude of each survey station. The solution requires constraints to locate the network relative to the geographic coordinate system and to fix the scale of the network, because the observations consist solely of angles. A "free" adjustment, that is, one with the minimum of constraints, for a network with only angle measurements is obtained by fixing the latitude and longitude of two stations within the network. The total number of unknowns for a network with  $n$  stations is then  $2(n - 2)$ . The number of degrees of freedom ( $c$  in equation 2.2) is the number of observed angles minus the total number of unknowns.

The adjustment program used is *Anderson's* [1969], which requires directions instead of angle measurements. This is a subtle point, but it is important in the analysis. Adjacent angles are correlated when directions are observed in a round because they have one direction in common. With the method of angles each angle is independent. To make the observations compatible with the adjustment program, each angle is treated as one round, that is, the 57 angle measurements are represented as 57 pairs of directions. Possible blunders will generally be revealed by a large residual.

The residuals from the adjustment including all 57 angles gave a 2.8" standard

**Table 3.3.** Statistics from Adjustments of the 1947 Triangulation

No. of Angles	Degrees of Freedom	Std. Dev.	Max. Residual	Angle with Max. Residual
All Ten Stations				
57	41	2.8"	7.6"	Wanch to Pierce and Rufus
56	40	2.6"	6.2"	Walker to Wanch and Conuma
55	39	2.4"	4.9"	Rufus to Albermarle and Walker
54	38	2.3"	4.4"	Conuma to Walker and Wanch
53	37	2.2"	4.5"	Baldy to Pierce and Rufus
52	36	2.1"	4.0"	Rufus to Baldy and Pierce
51	35	2.0"	4.4"	Pierce to Conuma and Wanch
50	34	1.8"	4.4"	Rufus to Walker and Conuma
49	32	1.7"	3.4"	Walker to Baldy and Pierce
48	31	1.6"	2.8"	Wanch to Gold and Baldy
Seven Second-Order Stations				
40	30	2.5"	4.6"	Rufus to Baldy and Pierce
39	29	2.3"	4.7"	Pierce to Conuma and Wanch
38	28	2.2"	4.3"	Rufus to Walker and Conuma
37	27	2.1"	4.1"	Baldy to Pierce and Rufus
36	26	1.9"	3.8"	Conuma to Walker and Wanch
35	25	1.9"	3.8"	Walker to Baldy and Pierce
34	24	1.7"	2.8"	Wanch to Gold and Baldy
33	23	1.5"	3.0"	Pierce to Wanch and Gold
Northern Subnet				
9	5	2.1"	3.0"	Wanch to Gold and Baldy
8	4	0.9"	1.2"	Baldy to Conuma and Gold
Southern Subnet				
19	13	2.3"	3.9"	Baldy to Pierce and Rufus
18	12	2.0"	3.2"	Pierce to Conuma and Baldy
17	11	1.5"	3.2"	Rufus to Walker and Conuma

deviation for an angle with 10 sets and a maximum residual of 7.6". This error is greater than that derived from the root-mean-square triangle closure (1.9"), and that from the mean of 10 sets (1.4" assuming a 4.5" standard error for a single set). I assumed that the angle with the largest residual was a "blunder", and deleted it from the observations,

and then repeated the adjustment. To reduce the standard deviation of an angle with 10 pointings to  $1.6''$ , nine angles had to be rejected. The standard deviation and maximum residual for each adjustment is listed in Table 3.3.

Some of the angles with large residuals may be blunders, while others may arise from random error. The first two angles, Wanch to Pierce and Rufus and Walker to Conuma and Wanch, clearly have the largest residuals and are likely to be blunders. The third largest residual is in Rufus to Albermarle and Walker, an angle that has a  $17''$  spread with just 5 sets of pointings (Table 3.1). Note that the triangle with the  $10''$  misclosure, Walker-Conuma-Wanch, has two angles with large residuals. The other triangles with large misclosures, Wanch-Gold-Baldy and Wanch-Gold-Conuma, however, have only the common angle Wanch to Gold and Baldy with a relatively large residual. The three angles with the largest residuals are considered to be blunders and are deleted from the data set.

The positions of stations Albermarle and Pretty (see Figure 3.1) are not as well determined as those of the other stations because there are relatively few angles measured to or from them. The position of New is overdetermined, but the observations to or from it are generally less precise because they have only five sets of pointings. The subset of the network that includes the seven remaining, well-determined stations was put through the same adjustment-rejection process used for the entire network. The three angles identified as blunders earlier were not included in these adjustments. The results from adjustments of the seven second-order stations are also listed in Table 3.3. The angles with large residuals in the subnet comprised of the seven second-order stations correspond well with those in the main network.

The subnet was further subdivided into a northern section comprised of the stations Wanch, Gold, Baldy, and Conuma, and a southern section with the stations Conuma, Baldy, Pierce, Rufus, and Walker. The results from the adjustments for these two sections are also listed in Table 3.3. The northern section is not very redundant with only 5 degrees

of freedom, but the angle Wanch to Gold and Baldy has the largest residual even if other angles are deleted. This angle is suspect because it is common to two triangles that have misclosures of  $6.0''$ , Wanch-Gold-Baldy and Wanch-Gold-Conuma. In the southern section, the angle with the largest residual is Baldy to Pierce and Rufus.

Summarizing, the adjustments reveal 10 angles with relatively large residuals. At least 3 of these angles are blunders, and the remaining 7 may be blunders or just random errors. Two of the seven are within triangles with larger than expected misclosure and might be eliminated for that reason. One of the two, however, has the tenth largest residual in the adjustment of the entire network, and eliminating it implies that the other angles with larger residuals should also be deleted. The standard deviation of an observed angle with 10 sets of pointings from the adjustment, excluding the 3 angles identified as blunders, is  $2.3''$ .

The different levels of accuracy in triangulation surveys is referred to as the "order" of the survey. First-order work is the most accurate, while fourth-order work is the least accurate. The guidelines for second-order horizontal directions from Survey and Mapping Branch [*Dept. of Energy, Mines, and Resources, 1973*] specify a minimum of 6 sets with the standard deviation of a direction being  $2.0''$ , and triangle closure less than  $5.0''$ . The angle measurements from the subnet comprised of the 7 second-order stations all have at least 10 sets of pointings, with the standard deviation of a typical angle being  $2.5''$  (equivalent to a standard deviation of  $1.8''$  in a direction). There are, however, two triangles in the northern section with triangle closures greater than  $5.0''$ .

#### 4. HORIZONTAL DEFORMATION IN THE GOLD RIVER NETWORK

The horizontal deformation of the Gold River network, in terms of the shear components of surface strain accumulation, is calculated from the change in the angles between stations common to the 1947 and 1982 surveys. Angles from the 1982 trilateration that correspond to those measured in 1947 are deduced from adjusted positions. The precision of the trilateration is such that errors introduced by the adjustment are negligible. Use of strain components to describe the accumulated deformation offers several advantages over station displacement vectors, because displacement vectors are derived from adjusted positions. Adjusted positions depend on scale and azimuth control for each survey and choice of fixed origin in the individual adjustments. The shear, dilatational, and rotational components of surface strain are independent; the derived shear strain, therefore, is not affected by the scale or azimuth control. Strain is calculated from the change in distance or angles, which are not altered by the choice of fixed origin. The most accurate and direct measure of the deformation within a triangulation network is provided by the shear strain accumulation.

Angle changes do not provide the dilatational component of surface strain accumulation. Dilatation could be computed from the change in the adjusted positions [Bruener, 1979; Welsch, 1979; Bibby, 1982; Snay et al., 1983], but scale control in the 1947 survey was not sufficiently accurate to allow resolution of accumulated low-level dilatational strain. The scale control in early triangulation was generally from a short ( $\approx 1$  km), taped baseline that is measured to an accuracy of about 1–4 ppm. Much of the accuracy is lost in the extension of the short base through the network; length closures as large as 200 ppm are allowed for surveys similar to the 1947 triangulation [Federal Geodetic Control Committee, 1980].

#### 4.1. CALCULATION OF SHEAR STRAIN FROM ANGLE CHANGES

Under the assumption of uniform strain, the shear strain in an individual triangle [Frank, 1966], or in any collection of angles [Prescott, 1976] may be computed from the change in paired angle observations. Prescott's extension of Frank's method has the additional assumption of uniform strain in time whenever repeated surveys covering different periods are included. The strain is given in terms of the independent shear components  $\gamma_1$  and  $\gamma_2$ . The shear components defined in terms of the tensor components with the 1-axis east and the 2-axis north are

$$\gamma_1 = \epsilon_{11} - \epsilon_{22} \quad \text{and} \quad \gamma_2 = 2\epsilon_{12} \quad (4.1)$$

A positive  $\gamma_1$  corresponds to pure shear with a north-south axis of compression, and a positive  $\gamma_2$  corresponds to a pure shear with a northwest-southeast axis of compression. In combination with an equal and opposite rotation a positive  $\gamma_1$  corresponds to a simple shear with right-lateral motion across a northwest-southeast line or left-lateral motion across a northeast-southwest line. Similarly, a positive  $\gamma_2$  corresponds to a simple shear with right-lateral motion across an east-west line or left-lateral motion across a north-south line. Following the convention of Savage [1983b], the engineering shear strain components,  $\gamma_1$  and  $\gamma_2$  and the related total shear  $\gamma$ , are given in units of  $\mu\text{rad}$ , whereas tensor shear,  $\epsilon_{12}$ , is given in  $\mu\text{strain}$ .

The magnitude and orientation of a shear strain that is a combination of the shear components is described by the total shear,  $\gamma$ , and the azimuth of the axis of maximum compression,  $\zeta$ , where

$$\gamma = (\gamma_1^2 + \gamma_2^2)^{\frac{1}{2}} \quad (4.2)$$

$$\zeta = \frac{1}{2} \tan^{-1} \left( -\frac{\gamma_2}{\gamma_1} \right) + \frac{\pi}{2} \quad (4.3)$$



An alternative representation uses the magnitude and directions of the principal deviatoric strains, which are related to the total shear by

$$\gamma = \epsilon_1 - \epsilon_2 \quad (4.4)$$

where  $\epsilon_1$  is the maximum extensional strain and  $\epsilon_2$  is the maximum compressional strain. The orientation of the compression axis is given by  $\zeta$ . As can be seen in equation 4.4 the dilatational strain, which is equal to  $\epsilon_1 + \epsilon_2$ , is undetermined by angle changes; therefore, the principal strains are given their deviatoric values ( $\epsilon'_i = \epsilon_i - \Delta/2$ ; where  $\Delta =$  dilatation). The deviatoric principal strains are those corresponding to a pure shear strain, and are equal in magnitude but opposite in sign. Strain accumulation will be given in terms of an average rate to allow comparison with the deformation in other areas.

The change in an angle is related to the shear components of strain [*Frank*, 1966] by

$$\delta\phi = \frac{1}{2}\gamma_1(\sin 2\theta_2 - \sin 2\theta_1) + \frac{1}{2}\gamma_2(\cos 2\theta_2 - \cos 2\theta_1) \quad (4.5)$$

where  $\theta_1$  and  $\theta_2$  are the azimuths ( $^\circ$  from north) of the sides that enclose the angle  $\phi$ . There is one equation of the form (3.5) for each angle change, and two or more angle changes determine  $\gamma_1$  and  $\gamma_2$ . The angle changes, however, could be due to observational error. The standard deviation of the shear components from a set of  $n$  angle changes with a standard error of  $\sigma$  (in radians) is about [*Savage*, 1983b, p. 14]

$$\sigma\sqrt{8/n} \quad (4.6)$$

For example, if we assume a standard error of 2.3'' for a 1947 observed angle and 0.6'' for a 1982 adjusted angle, then standard deviation of the shear components from the 54 angle changes in the Gold River Network is about 2.4'' or 11.5  $\mu$ rad. Assuming uniform strain in time, the standard deviation of the average rate of strain accumulation in the 35-year interval between surveys is 0.13  $\mu$ rad/yr.

The most probable values for the shear strain components are calculated with the least-squares solution described by *Prescott* [1976]. Uniform strain in space and time was assumed within the portion of the network included in the input data set. Angle changes were derived from paired direction lists, one for the initial survey and the other for the resurvey. The angle changes were weighted by the inverse square of their standard deviation. The covariance term in the weight matrix given by *Prescott* [1976] to account for the correlation between adjacent angles in a round of directions was not included because the observations consisted of angle measurements.

#### 4.2. SHEAR STRAIN ACCUMULATION BETWEEN 1947 AND 1982

The accumulated shear strain is derived from the comparison of the observed 1947 angles with adjusted angles from the 1982 survey. In the least-squares calculation, each angle of each pair is weighted by the inverse square of its standard error. The standard error in an 1947 angle with 10 sets of readings is assumed to be  $2.3''$ , the value obtained from the adjustment of the network with 54 angles. For angles with more or less than 10 sets, the standard error is altered by the  $\sqrt{10}/\sqrt{n}$ , where  $n$  is the number of sets. The standard error in an adjusted angle in the 1982 survey is more difficult to determine, because the error in an adjusted angle depends on the error in the station positions. The adjustment program that I used, *Anderson's* [1969], does not provide the error in an adjusted angle. I arbitrarily assigned an error of  $0.6''$  for an angle derived from the 1982 adjusted positions. This estimate is probably conservative, as the precision of the distance measurements is better than 3 ppm ( $0.6'' = 3$  ppm; the 1982 adjustment includes both standard and high-precision distance measurements). The primary source of error in an angle change is the error in a 1947 angle.

The change in the angles between 1947 and 1982 are listed in the last column of Table 3.1. Most of the angle changes are less than  $3''$  and only three are greater than

twice the standard error in an angle change (4.8"). The individual angle changes could be due solely to random observational error. Systematic patterns in the angle changes are investigated by calculating the average shear strain accumulation in the network and in subsets of the network.

Average shear strain accumulation rates were calculated for the entire network, the northern section, and the southern section. The northern section is comprised of the 2<sup>nd</sup> order stations Wanch, Gold, Baldy High, and Conuma. The southern section is comprised of the 2<sup>nd</sup> order stations Conuma, Baldy High, Pierce, Rufus, Walker and, the 3<sup>rd</sup> order stations Pretty Girl, New, and Albermarle (see Figure 3.1 for locations). Strain was calculated from the angle changes between all the stations and from those between the 2<sup>nd</sup> order stations only; in addition, strain was calculated using all of the angle changes between the stations in an area and for a data set in which the angles with the largest residuals (see Table 3.3) were deleted. The average shear strain accumulation rates,  $\gamma_1$ ,  $\gamma_2$ , and  $\gamma$ , the azimuth of the maximum extension axis,  $\zeta$ , and the ratio of observed to theoretical error,  $r$ , for each of the calculations is listed in Table 4.1.

In all areas and for all data sets, the average rate of shear strain accumulation given by  $\gamma$  in Table 4.1 is either not significant or only marginally significant at the two standard deviation (95% confidence) level. The highest average rate of strain accumulation is  $0.46 \pm 0.23 \mu\text{rad/yr}$  in the northern section of the network. There is nearly a 90° difference in the axis of maximum compression,  $\zeta$ , between the northern and southern sections; this seems to indicate a spatially non-uniform strain field. This difference is graphically illustrated by the variation in the average principal deviatoric strain rates shown in Figure 4.1. The shear strain accumulation in the entire network, however, is consistent with a spatially uniform strain field; that is, the residuals from the uniform strain calculation are about the same as the expected error in an angle change. The values of the ratio of the average residual to the expected error is shown by "r" value listed in

**Table 4.1.** Shear Strain Accumulation in the Gold River Network Between 1947 and 1982

Area	No. Angles	$\dot{\gamma}_1$ $\mu\text{rad/yr}$	$\dot{\gamma}_2$ $\mu\text{rad/yr}$	$\dot{\gamma}$ $\mu\text{rad}$	$\zeta$ ° from N	r
Entire Network						
All Stations	54	$-0.09 \pm 0.10$	$-0.22 \pm 0.11$	$0.23 \pm 0.12$	$56 \pm 12$	1.1
All Stations	47	$-0.17 \pm 0.10$	$-0.21 \pm 0.13$	$0.27 \pm 0.13$	$64 \pm 11$	1.0
2 <sup>nd</sup> Order Stations	39	$-0.06 \pm 0.11$	$-0.10 \pm 0.13$	$0.12 \pm 0.13$	$61 \pm 26$	1.1
2 <sup>nd</sup> Order Stations	34	$-0.19 \pm 0.12$	$-0.15 \pm 0.14$	$0.25 \pm 0.14$	$71 \pm 14$	1.0
Southern Section						
All Stations	31	$-0.15 \pm 0.13$	$0.05 \pm 0.16$	$0.16 \pm 0.16$	$100 \pm 30$	1.0
All Stations	27	$-0.33 \pm 0.14$	$-0.03 \pm 0.17$	$0.33 \pm 0.17$	$87 \pm 40$	0.8
2 <sup>nd</sup> Order Stations	20	$-0.14 \pm 0.16$	$0.12 \pm 0.18$	$0.19 \pm 0.19$	$111 \pm 30$	1.0
2 <sup>nd</sup> Order Stations	17	$-0.22 \pm 0.18$	$0.22 \pm 0.19$	$0.31 \pm 0.19$	$113 \pm 20$	0.7
Northern Section						
2 <sup>nd</sup> Order Stations	9	$0.29 \pm 0.20$	$-0.35 \pm 0.23$	$0.45 \pm 0.23$	$26 \pm 13$	1.0
2 <sup>nd</sup> Order Stations	8	$0.30 \pm 0.21$	$-0.33 \pm 0.24$	$0.44 \pm 0.24$	$24 \pm 14$	1.0

Table 4.1. In fact, the “r” value is close to 1 in all of the strain calculations. There are marginally significant variations in the strain field within different parts of the network, but a good fit to a uniform strain field in the entire network; this apparent inconsistency shows that the strain field is not well determined by the observations.

The possibility that a few “bad” angles account for the variation in the strain was investigated by calculating the strain from data sets in which the angles with the largest residuals in the 1947 adjustment were eliminated. The resulting average strain accumulation rates are listed below the rates based on all the angle changes in Table 4.1. There is little change in the strain resolution because only a few angles were eliminated from each data set. The strain rates for the “cleaned up” data are generally greater, but the directions of maximum contraction and the fits to the uniform strain field change very little. The largest changes are in the southern section, where the average rate of shear increases from about  $0.2 \mu\text{rad/yr}$  to about  $0.3 \mu\text{rad/yr}$  and the ratio of observed to theoretical error

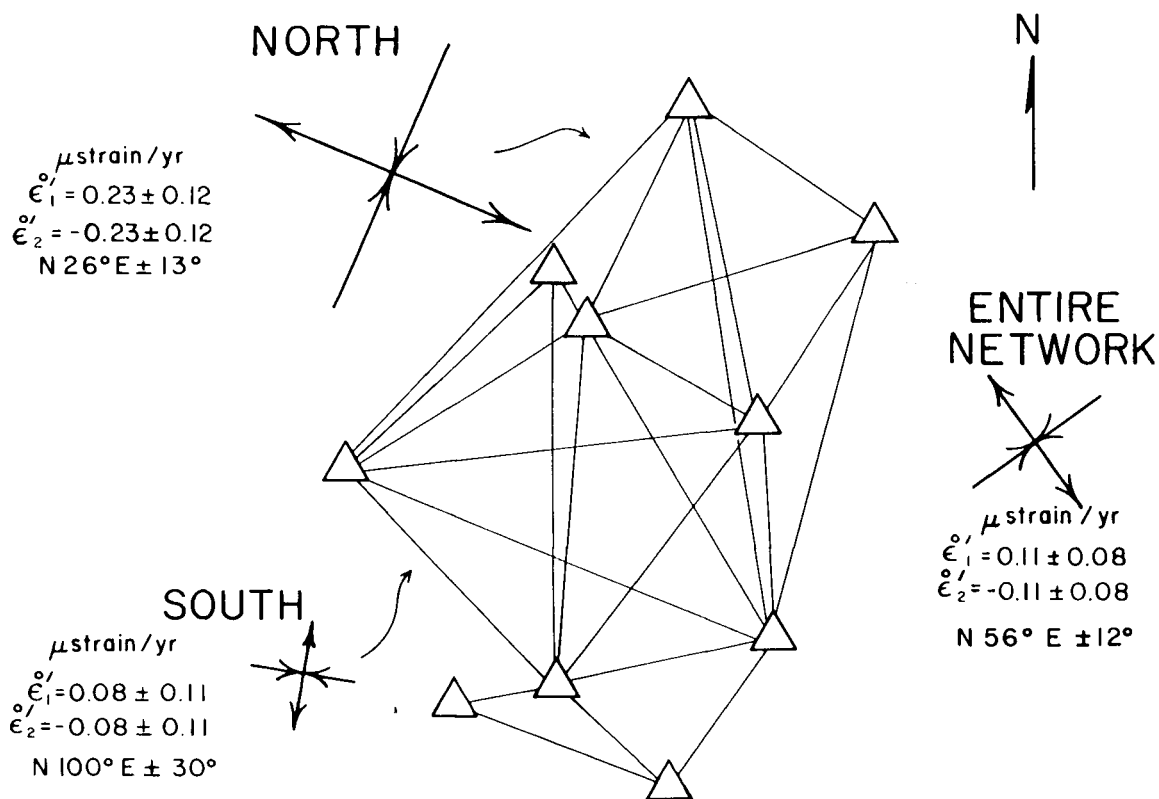


**Figure 4.1.** Map showing diagrams of the average principal deviatoric strain rates from angle changes within different areas in the Gold River network. The northern section includes the four stations making a quadrilateral in the northeast end of the network, the southern section includes the eight stations in the southwest end of the network, and the entire network includes all ten stations. The difference of the deviatoric principal strains is equal to the total shear  $\gamma$ .

decreases to about 0.7. The variation in the pattern of strain accumulation is not explained by a few poor angle observations. On the contrary, the elimination of some suspected bad angles tends to increase the average strain rates without altering the direction of maximum contraction.

The variation in the shear strain across areas smaller than those covered by the north and south subsections of the network was investigated by calculating the strain in individual triangles. The small number of angles increases the uncertainty in the calculated strain accumulation. Using equation 4.6, the 2.4" (11.6 $\mu$ rad) estimated error in an individual angle change gives an uncertainty of about 19 $\mu$ rad (average rate of 0.5 $\mu$ rad/yr) in the shear components for a triangle with all three included angles. The uncertainty is also related to the shape of the triangle; a narrow triangle has its sides in about the same direction, and the resulting shear components are not well determined. Some 1947 angles are derived from the sum of two adjacent angles. The standard error for these angles is increased by a factor of  $\sqrt{2}$  relative to the error for typical angle.

The average rate of shear strain accumulation within the individual triangles is listed in Table 4.2. Significant strain accumulation (95% confidence limit) is found in only one triangle, Baldy-Pierce-Rufus, with an average rate of shear strain of  $1.43 \pm 0.52\mu$ rad/yr. The strain in this triangle is suspect despite a triangle closure of 0.8" and a good fit to uniform strain, because two of the angles in this triangle (Baldy to Pierce and Rufus and Rufus to Baldy and Pierce) have large residuals in the 1947 network adjustment (see Table 3.3). Other triangles with possible systematic error are Conuma-Wanch-Gold and Wanch-Gold-Baldy, which have triangle closures of 6" or greater. These two triangles have the worst fit to a uniform strain field with errors being 1.4 and 1.2 times greater than the expected. Several triangles show an average rate of shear greater than 1 $\mu$ strain/yr, but they also have some of the largest standard deviations.

The spatial distribution of strain accumulation is shown in Figure 4.2 with diagrams of the average principal deviatoric strain rates for each triangle plotted at the centroid of the triangle. The highest average rates of deformation are seen in the southeastern and northwestern subsections of the network. In many of the triangles shear strain accumulation is not significant at one standard deviation. The deviatoric principal strain

**Table 4.2.** Shear Strain Rates Within Individual Triangles in the Gold River Network.

Triangle	No. An- gles	$\dot{\gamma}_1$ $\mu\text{rad/yr}$	$\dot{\gamma}_2$ $\mu\text{rad/yr}$	$\dot{\gamma}$ $\mu\text{rad/yr}$	$\zeta$ $^\circ$ from N	r	Clo- sure "
Con-Wanch-Gold	3	$0.59 \pm 0.29$	$-0.64 \pm 0.47$	$0.87 \pm 0.44$	$24 \pm 11$	1.4	6.6
Wanch-Gold-Baldy	3	$0.59 \pm 0.34$	$-0.29 \pm 0.49$	$0.66 \pm 0.41$	$13 \pm 9$	1.2	6.0
Gold-Baldy-Con	4	$-0.17 \pm 0.30$	$0.26 \pm 0.49$	$0.31 \pm 0.51$	$119 \pm 23$	0.5	-2.3
Baldy-Con-Wanch	3	$0.20 \pm 0.42$	$-0.71 \pm 0.45$	$0.73 \pm 0.50$	$37 \pm 14$	0.1	0.4
Walker-Con-Baldy	4	$-0.07 \pm 0.44$	$0.25 \pm 1.0$	$0.26 \pm 0.98$	$127 \pm 63$	0.4	2.3
Rufus-Con-Pierce	4	$-0.31 \pm 0.42$	$0.42 \pm 0.33$	$0.52 \pm 0.26$	$117 \pm 25$	0.7	3.3
Con-Baldy-Pierce	3	$-1.60 \pm 1.00$	$0.03 \pm 0.62$	$1.65 \pm 1.00$	$96 \pm 11$	0.6	-3.2
Walker-Baldy-Rufus	3	$0.25 \pm 0.39$	$-0.45 \pm 0.48$	$0.51 \pm 0.48$	$31 \pm 22$	0.1	-0.1
Baldy-Pierce-Rufus	3	$1.42 \pm 0.51$	$0.21 \pm 0.38$	$1.43 \pm 0.52$	$176 \pm 07$	0.2	0.8
Con-Pierce-Walker	4	$-0.08 \pm 0.30$	$0.31 \pm 0.50$	$0.32 \pm 0.47$	$128 \pm 31$	0.8	0.1
Pierce-Rufus-Walker	5	$-1.13 \pm 0.68$	$-0.61 \pm 0.76$	$1.28 \pm 0.92$	$76 \pm 10$	0.3	1.3
Baldy-Rufus-Con	3	$-0.23 \pm 0.41$	$0.05 \pm 0.50$	$0.23 \pm 0.45$	$96 \pm 60$	0.2	0.7
Rufus-Walker-Con	4	$0.08 \pm 0.28$	$0.31 \pm 0.41$	$0.32 \pm 0.44$	$142 \pm 20$	0.9	-4.6
Baldy-Walk-Pierce	3	$0.39 \pm 0.68$	$-0.74 \pm 0.36$	$0.84 \pm 0.45$	$31 \pm 21$	0.3	1.4
Rufus-P Girl-Pierce	3	$-0.17 \pm 0.29$	$0.11 \pm 0.44$	$0.21 \pm 0.33$	$107 \pm 58$	0.7	2.1
Gold-Baldy-Pierce	3	$-0.18 \pm 1.34$	$-1.35 \pm 2.20$	$1.36 \pm 2.30$	$35 \pm 23$	0.8	3.9

rates in these triangles are plotted with dashed arrows. The three triangles that may be subject to systematic error are marked by dotted arrows, while the triangles with shear greater than one standard deviation are marked by solid arrows. The patterns of strain accumulation in the north and south sections differ on the scale of individual triangles, although the strain is not entirely consistent in either area. The northern section has only four triangles, two of which may contain a bad angle measurement, and this raises doubts about the calculated strain accumulation. All the triangles that show an average rate of shear strain greater than  $1\mu\text{rad}$  and that are not suspected to be contaminated by systematic error have standard deviations near  $1\mu\text{rad/yr}$ . Consistently small rates of strain accumulation are observed in the northwestern section of the network the area closest to the epicenter of the 1957  $M=6.0$  earthquake (Figure 2.1); thus, deformation from the earthquake does not appear to contaminate the strain accumulation.

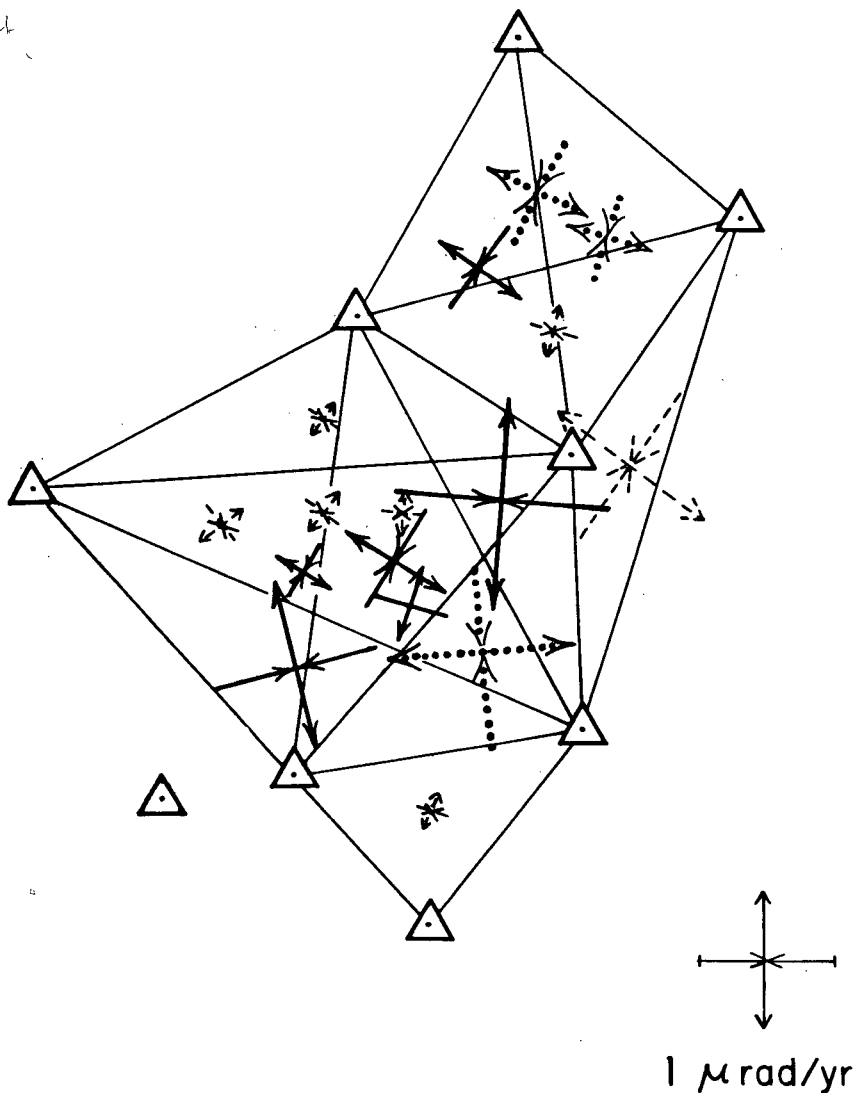


**Figure 4.2.** Map of the Gold River network showing diagrams of the average principal deviatoric strain rates within individual triangles. The strain rates are plotted at the centroid of each triangle. The solid arrows indicate that the average shear strain accumulation is greater than one standard deviation, the dashed arrows indicate it is less than one standard deviation, and triangles that may be contaminated by systematic error are shown with dotted arrows. The highest average rates of strain accumulation marked by the solid arrows are also the triangles with the largest standard deviations.

Summarizing, the strain accumulation in the Gold River network is not well determined by the angle changes between 1947 and 1982. The average rate of engineering shear ( $\gamma$ ) within the network is  $0.23 \pm 0.12 \mu\text{rad}$  with the axis of maximum compression bearing  $N56^\circ E \pm 12^\circ$ . Even though the angle changes are consistent with uniform strain,



there is a marginally significant difference in the average rate of shear and in the direction of maximum compression between the northern and southern subsets of the network. The average rate of shear in the northern subsection from 9 angle changes is  $0.45 \pm 0.23 \mu\text{rad/yr}$ , with the maximum compression axis bearing  $N26^\circ E \pm 13^\circ$ , compared to  $0.16 \pm 0.16 \mu\text{rad/yr}$  and  $N100^\circ E \pm 30^\circ$  in the southern subsection. There is a possibility that a few "bad" angles contaminate these results. In the northern subsection there are two triangles that have closures greater than or equal to 6". Eliminating one of the suspect angles, however, has no effect on the calculated strain field. Deleting suspect angles in the southern subsegment increases the calculated strain accumulation, and improves the uniform strain fit. Strain accumulation within individual triangles is poorly determined, but it appears to be extremely variable. In the northern subsection, strain rates and orientations appear to be similar with shear averaging about about  $0.6 \mu\text{rad/yr}$  in three of four triangles. In the southern subsection there is very little strain to the west and extreme variability to the east.

These results differ from those given in the preliminary reports for the study [*Lisowski and Slawson, 1983a; Lisowski and Slawson, 1983b*] . The rates of strain accumulation reported in May of 1983 at the G.A.S.C. meeting in Victoria were derived from a set of angles used as input for a B.C. Ministry of Survey's adjustment for central Vancouver Island. The angles were not a complete set and contained some adjusted angles, possibly from a local adjustment. The next set of results were reported at the Pacific Northwest A.G.U. meeting in Bellingham in October of 1983. These results are from the correct set of angles observations, but they were treated as rounds of directions rather than independent angles.

The average rate of strain accumulation in the Gold River network is roughly comparable with rates measured in Japan. Japan has experienced a number of large earthquakes and it is necessary to correct the observed strains for the coseismic motions.

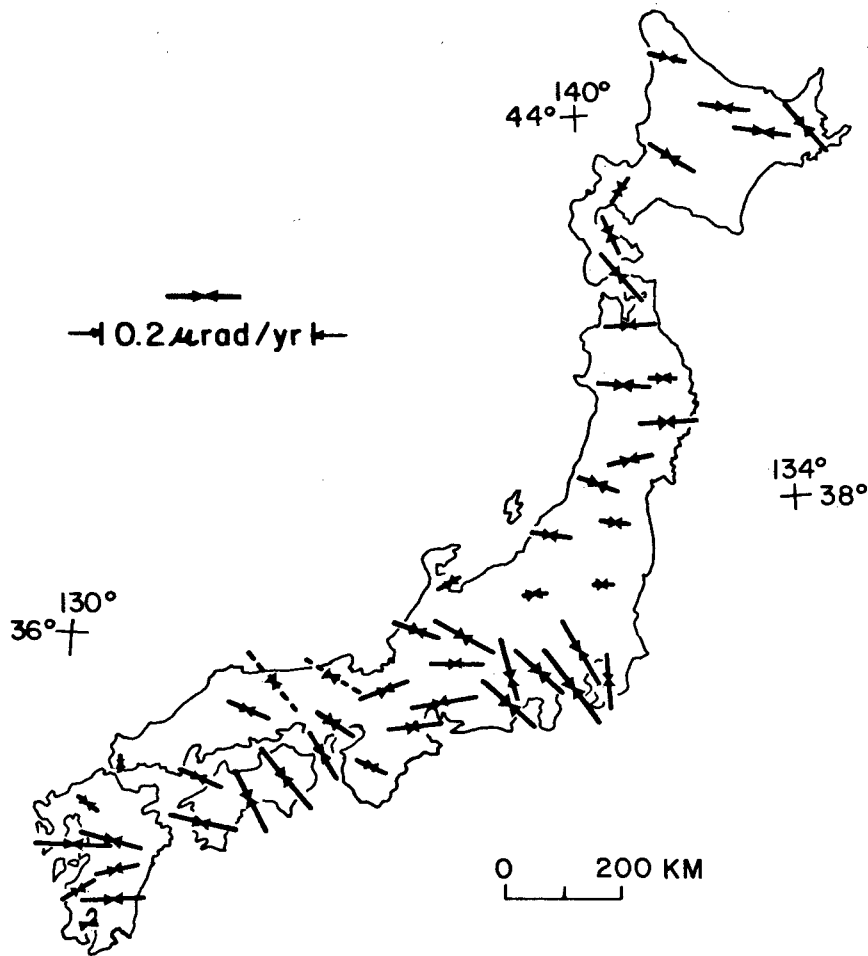


**Figure 4.3.** The average rate of tectonic shear strain corrected for earthquakes in Japan (modified from *Nakane* [1973]). The direction and size of the arrows show the principal axis of compression and the average yearly rate of shear strain accumulation.

The strains shown in Figure 4.3 are believed to represent the average rate of secular strain accumulation in Japan [*Nakane*, 1973]. Compression is generally in the direction of plate convergence, and shear strain rates average between 0.1 and 0.2  $\mu\text{rad/yr}$ .

## 5. SURFACE DEFORMATION FROM SUBDUCTION ZONE MODELS

Contemporary horizontal and vertical surface deformation from geodetic studies along the Cascadia subduction zone is summarized in Figure 1.1. The overall pattern of deformation appears to be a gentle tilting of the outer coast toward the land and low rates of strain accumulation with maximum contraction in a southwest-northeast direction. Actual compressional strain has been measured only in the Seattle and Olympic networks, where the deformation is computed from distance changes. In the other networks compression is inferred from shear strains. This is indicated in Figure 1.1 by using the principal strain rates for the Seattle and Olympic networks and principal deviatoric strain rates for the Gold River, Juan de Fuca, and Johnstone Strait Networks.

A relation between the horizontal deformation and the interaction of the Juan de Fuca and North America plates is indicated by the general alignment of the compression strain with *Riddihough's* [1977; 1984] proposed east-northeast direction of convergence between the Juan de Fuca and North America plates (Figure 1.1). *Savage et al.* [1981] proposed that locking the shallow interface between the plates could explain the compression observed in the Seattle network between 1972 and 1979. They point out, however, that the resulting east-northeast compression is not consistent with the north-south regional compressive stress indicated by the focal mechanisms of shallow earthquakes in the Puget Lowlands [*Crossen, 1972; 1979*]. *Sbar* [1983] suggested that the strain measurements may sense short-term strain fluctuations, whereas the earthquakes, which release a large amount of strain, respond to the total strain accumulation. Several workers (*e.g., Crossen, 1972; Yelin, 1984*) have proposed that the north-south compressive stress may arise from a dominant stress related to the interaction of the Pacific and North American plates. Spatial variation in the tectonic stress is also possible [*Weaver and Smith, 1983*].

A similar inconsistency exists in central Vancouver Island, where north-south

compressive stress is indicated by the focal mechanism solutions [Rogers, 1979] and northeast-southwest compression by the strain measured in the Gold River network. These observations may not be as inconsistent as they appear, because the strain accumulation in the Gold River network is not well-determined and many of the focal mechanism solutions have a NNE axis of compressive stress.

The oceanic Nootka fault zone may be important in the contemporary tectonics of central Vancouver Island. Differential motion between the Explorer and Juan de Fuca plates is believed to be accommodated by left-lateral slip across the Nootka fault zone [Hyndman *et al.*, 1979]. The central Vancouver Island earthquakes occur along the general trend of the fault zone (see Hyndman *et al.* [1979], Figure 2), and the preferred focal mechanism solutions [Rogers, 1979] are consistent with left lateral slip across a northeast trending vertical plane. Hyndman *et al.* [1979] speculated that the stresses responsible for the earthquakes may arise from the fault displacements being coupled to the overlying continental lithosphere.

Rogers [1979; 1983b] suggested that the Nootka fault marks the boundary between oceanic lithospheres that interact differently with the overlying continental lithosphere. He believes that the earthquakes are due to coupling between the Explorer and North American plates. He assumes weak or no coupling between the Juan de Fuca and North America plates. In his 1979 paper, the north-south compressive stresses indicated by the focal mechanisms were ascribed to rigid coupling between the Explorer and North America plates due to the extreme oblique angle of convergence. This oblique angle of convergence from Riddihough's [1977] model is not supported by Riddihough's [1984] plate motion model, which shows a northeast convergence direction for the Explorer plate. In his thesis, Rogers [1983] gave an alternate mechanism. The slowing of the motion of the Explorer plate in the last 3 Ma [Riddihough, 1977] results in the phase change equilibrium point in the upper crust moving to a shallower depth, producing a volume increase in the

affected portion of the upper crust. The resulting upward pressure increases the coupling with the overlying continental lithosphere. This mechanism would also seem to require north-south convergence (oblique subduction) between the Explorer and North American plates to produce a north-south compressional stress.

The landward tilt observed along the outer coasts adjacent to the Cascadia subduction zone remains unexplained. No tectonic mechanism, other than aseismic subduction was given by *Ando and Balasz* [1979] or *Riddihough* [1982]. To support their contention that such deformation is typical of aseismic subduction zones they used the long-term behavior of seismic subduction zones. Imbricate thrust faulting is a possible source of long-term uplift in seismic subduction zones. The deformation observed adjacent to a known aseismic subduction zone would have provided a better analog. The landward tilt is not consistent with some of the other tectonic hypotheses such as a regional north-south compressive stress, shear coupling above the Nootka fault zone, or coupling only between the Explorer and North America plates.

Summarizing, the various hypotheses to explain either the shallow continental earthquakes or the observed contemporary surface deformation are:

1. Coupling of the subducting Juan de Fuca and Explorer plates with the overriding North America plate along their shallow interface.
2. Coupling of the subducting and overriding plates around the Nootka fault zone.
3. Partial or full Coupling of the Explorer and North America plates and a north-south direction of convergence.
4. Secular movements associated with aseismic subduction.
5. Interactions between the Pacific and North American plates.

Surface deformation for hypotheses involving coupling between plates can be estimated with a dislocation model. I will present simple two-dimensional models for deformation due to coupling between the subducting and overriding plates. No attempt is made to calculate

deformation due to three-plate interactions such as along the subducting Nootka fault zone. The modeled deformation is based on many assumptions and simplifications, and, at best, will provide only a rough approximation of possible deformation. The computed deformation is dependent on the earth model, fault geometry, and fault displacements. Plate motions given by *Riddihough* [1984] will be used in the models. As pointed out in the introduction, the motions of the Explorer plate are not well determined and may vary along the plate margin. The geometry of the Cascadia subduction zone is approximated using published seismic studies.

The Gold River network is along the projection of the Nootka fault zone and may straddle several possible tectonic settings. The simple two-dimensional dislocation models that I use provide estimates of the deformation for a particular setting, but they make no account of possible variations along the strike of the subduction zone.

## 5.1. SUBDUCTION ZONE GEOMETRY

The Cascadia subduction zone lacks a topographic trench, but there is little doubt that the base of the continental slope (depth  $\approx 2.5$  km) marks the plate boundary [*Riddihough and Hyndman*, 1976]. The strike of the plate boundary changes from north-south along the Northern California and Oregon coasts to northwest-southeast along the coast of Vancouver Island (Figure 1.1). This change in strike requires some internal deformation in the subducted plate near the bend to accommodate changes in the dip of the subducted plate.

An active subduction zone is generally identified by earthquakes that occur along the plate interface (interplate earthquakes) and within the subducting and overriding plates (intraplate earthquakes). The Cascadia subduction zone lacks detectable shallow thrust (interplate) earthquakes [*Tobin and Sykes*, 1968; *Chandra*, 1974; *Milne et al.*, 1976; *Hyndman and Wiechert*, 1983]. There are, however, both deep and shallow intraplate

earthquakes. The hypocenters and focal mechanisms of the intraplate earthquakes provide important constraints on the geometry used for the subduction models. I will assume that the subduction geometry is about the same along the plate margin, and studies in Washington and southern Vancouver Island will be used to infer the geometry for central Vancouver Island.

The seismicity in Washington and southern British Columbia is rather diffuse, but in the central Puget Sound Lowlands there is a concentration of both deep and shallow earthquakes that continues in a relatively narrow band northward to the Gulf Islands. *Crossen* [1979] describes the seismicity in the Puget Sound region as follows: The earthquakes fall into two groups, those shallower than 30 km and those deeper than 40 km. Very few earthquakes occur in the 30-40 km depth range. The shallow earthquakes are not concentrated along lineations but are spread rather uniformly over a broad area. Shallow earthquakes have a bimodal depth distribution with a concentration at depths from 5 to 10 km and a larger concentration at depths from 15 to 25 km. The composite focal mechanisms available for these shallow earthquakes are generally consistent with north-south compression. Earthquakes at depths greater than 40 km show an alignment on a plane that dips  $10^{\circ}$  to  $20^{\circ}$  N $60^{\circ}$ E. Focal mechanisms for most of these deep earthquakes are ambiguous. The mechanism for the largest recent earthquake ( $M_s = 6.5$ ; 29 April 1965; located 63 km beneath Seattle) suggests normal slip on a fault striking north-northwest and dipping steeply to the east [*Langston and Blum*, 1977]. *Rogers* [1979 and 1983] reports a similar pattern of seismicity along the inner coast of southern British Columbia with the deeper seismicity concentrated along the northern extension of the Puget Lowlands. There is an abrupt decrease in the shallow and deep seismicity near the 49th parallel, which persists to central Vancouver Island.

The top of the subducted plate is best defined in the Olympic Peninsula of Washington where moderately deep earthquakes ( $>20$  to 30 km) define a shallowly dipping (minimum of

11°) Benioff zone [Taber and Smith, 1984]. Focal mechanism solutions for the earthquakes generally have the maximum compressive stress normal to the subducting slab and the tension axis in the plane of the slab with azimuths ranging between 0° and 120°. Taber and Smith believe these earthquakes are intraplate earthquakes, located beneath the Moho in the upper part of the oceanic lithosphere, and that they represent down-dip tension possibly from viscous drag as the slab sinks under its own weight. Reyners [1980] interpreted similar focal mechanisms from earthquakes in the subducted Pacific plate beneath North Island, New Zealand, to represent loading by the overlying plate. Shallow seismicity extends to a depth of about 20 km near the coast and this zone thickens to 30 km on the eastern edge of the Olympic Peninsula. Shallow earthquakes are sparse and of low magnitude and no focal mechanisms are available. The number of shallow earthquakes increases abruptly at the boundary with the western edge of the Puget Sound depression. This concentration of earthquakes occurs above the axis of a possible downward bend in the subducted plate as the dip appears to steepen to between 20° and 30° [Crossen, 1983, Figure 8]. Because of the change in the orientation of the dip azimuth of the subducted plate, the bending of the plate may involve complex internal deformation beneath Puget Sound such as a tear [Keen and Hyndman, 1979] or a warping [Rogers, 1983a]. The downward flexure in the subducted plate is sufficient to explain the focal mechanism (down-dip tension) of the 29 April 1965 Seattle earthquake.

A cross section of the Cascadia subduction zone in southern Vancouver Island is similar to that given for the Olympic Peninsula. The refraction model given by Ellis *et al.* [1983] has the Juan de Fuca plate dipping shallowly ( $\approx 10^\circ$ ) from the break in the continental slope for about 200 km to a depth of about 22 km where it makes a downward bend.

A cross section of the subduction zone in the vicinity of the Explorer plate has not been published. There is no volcanic arc adjacent to this portion of the subduction zone, which may indicate that the plate does not make a downward bend. I use cross-sectional



geometry similar to that given for southern Vancouver Island to model the subduction zone adjacent to the Explorer plate.

In the terminology of *Davies and House* [1979] the shallow-dip segment of the plate interface from the base of the continental slope to the flexure beneath Puget Sound and Georgia Strait is the main thrust zone. Although the subducted plate extends well into the asthenosphere beyond this flexure, only an abbreviated Benioff zone exists due to a combination of the low rate of subduction and the relative youth of the subducted material [*Riddihough and Hyndman*, 1976]. Presumably, the top of the subducted plate lies at a depth of about 100 km beneath the Cascade-Garibaldi volcanic arc.

The specific geometry used in the models is shown in the top of Figure 5.1. The Juan de Fuca plate dips at about  $10^\circ$  from the break in the continental slope for about 150 km to an axis at roughly 30 km depth in the central part of the Island. The strike of the subduction zone is taken to be  $N40^\circ W$  and convergence at a rate of 47 mm/yr is assumed to be perpendicular to this boundary. The same geometry is assumed for the subduction zone adjacent to the Explorer plate, but the perpendicular convergence is altered to a rate of 20 mm/yr.

## 5.2. SUBDUCTION MODELS

The process of strain accumulation and release at a subduction zone is described by *Savage* [1983a] as a superposition of steady-state subduction and a repetitive cycle of slip on the main thrust zone. In steady-state subduction the subducting plate slips steadily along its own length into the asthenosphere. Locking of the main thrust zone is represented by adding virtual slip of the same rate but with opposite sense to that occurring during steady-state subduction. The details of the deformation then depend upon the earth model employed. I will discuss the results for a purely elastic earth model [*Savage*, 1983a] and an elastic-viscoelastic earth model in which the viscoelastic element represents flow in the

asthenosphere [Thatcher and Rundle, 1984].

The calculation of the model deformation is particularly simple where the earth can be represented as an elastic half-space [Savage, 1983a]. In this case there is no transient postseismic relaxation, and the interseismic deformation is due solely to the virtual "backward" slip on the locked portion of the main thrust zone. Profiles of deformation across the Cascadia subduction zone adjacent to the Juan de Fuca plate in central Vancouver Island are shown for the elastic half-space model ( $H = \infty$ ) in Figure 5.1. Uplift is concentrated directly above the down-dip end of the locked section of the main thrust zone, decreasing uniformly to the south-southwest and east-northeast. No subsidence is produced by the model east-northeast of the end of the profile. Low rates of uplift on the outer and inner coastlines are obtained by locating the down-dip end of the locked zone about 20 km inland from the coastline (Figure 5.1). The profile of  $\dot{\epsilon}'_{22}$  (extension rate in the direction of plate convergence) shows contraction everywhere, except directly above the down-dip end of the locked zone where surface flexure has apparently counteracted the contraction. A smearing out of the displacement discontinuity at the down-dip end of the locked zone will smooth out the deformation profiles. In this model convergence is taken to be normal to the plate boundary resulting in no shear parallel to the strike of the subduction zone.

The observed deformation profiles for central Vancouver Island are shown schematically by dotted line segments in Figure 5.1. The uplift profile is shown as a queried line segment extending from the coastline landward across to the Johnstone Strait. This observed uplift is based on sea-level changes recorded at Tofino and Campbell River [Riddihough, 1982]. A profile of elevation change across the Island is not available. The extension rate in the direction of plate convergence ( $\dot{\epsilon}'_{22}$ ) is shown by the dotted segment, representing the average strain rate observed across the Gold River network. The average extension rate for the Gold River network was calculated from the observed shear strain rate by

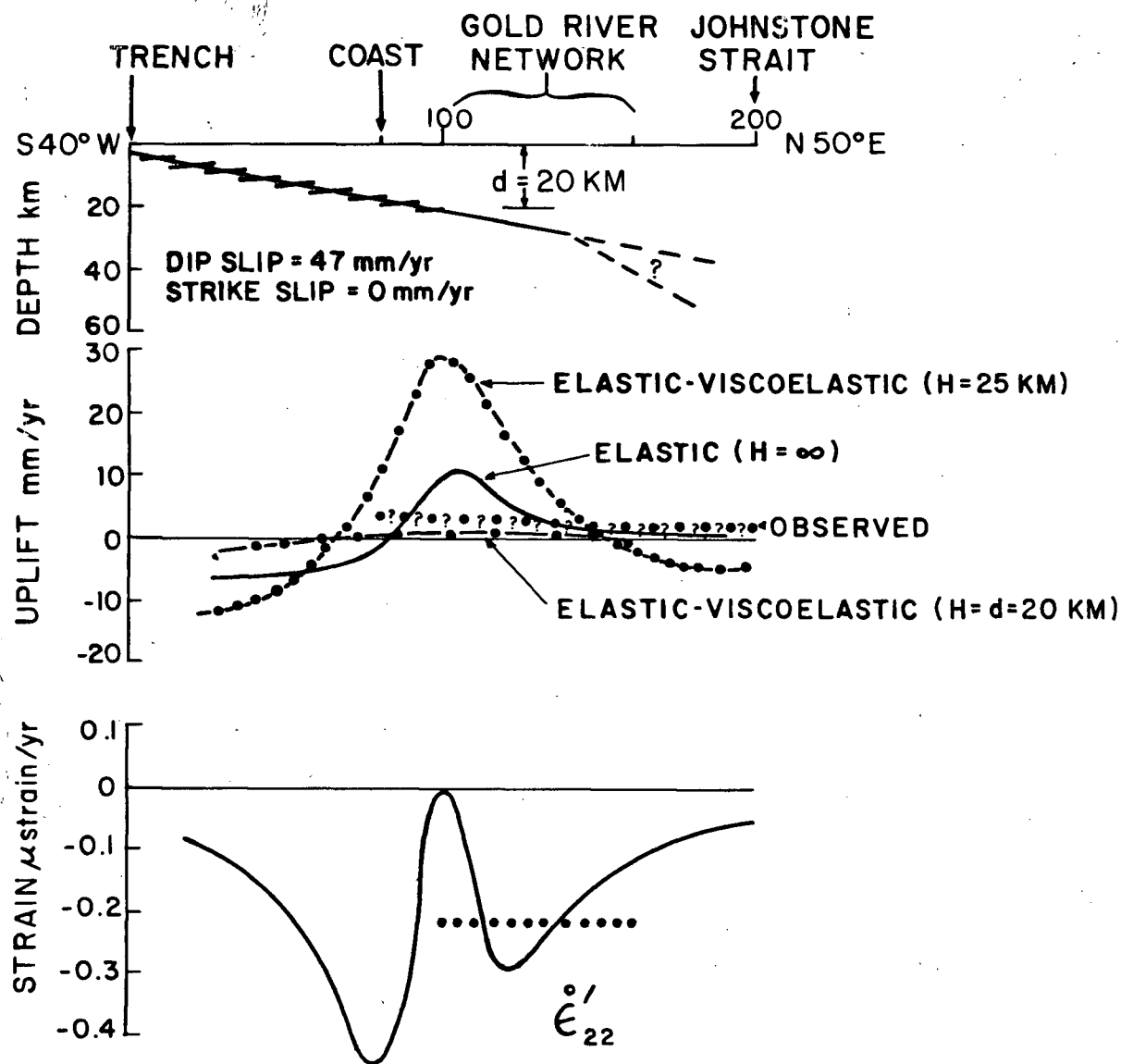


**Figure 5.1.** The rate of uplift and strain at the free surface from elastic dislocation models of the Cascadia subduction zone. The top figure shows the model geometry with the main thrust zone dipping  $10^\circ$  and locked to a depth of 20 km. The dip-slip component of motion is 47 mm/yr and the strike-slip component of motion is 0 mm/yr. Tensor strain component  $\epsilon'_{22}$  is extension parallel to N50°E. The dotted lines in the uplift and strain profiles represent the observed deformation. The observed vertical deformation is queried across the Island because it is based on tide gauges on opposite ends of the Island. Uplift profiles for the elastic-viscoelastic models with the thickness of the elastic plate,  $H$ , of 25 and 20 km are shown for comparison with the purely elastic dislocation model.

assuming that the total strain rate corresponds to a uniaxial contraction in the direction of plate convergence.

The elastic half-space model furnishes a reasonable qualitative explanation of the observed deformation, but the quantitative fit is not very good. The predicted contraction rate in the direction of plate convergence is about the same as observed in the Gold River network, but the decrease in strain from the coast inland is opposite of that observed within the network. Strain accumulation across the Johnstone Strait indicates north-south contraction [Slawson and Savage, 1979], whereas east-northeast contraction is predicted by the model. The model approximates the low rates of uplift of the coasts, but it cannot reproduce the subsidence expected to the east-northeast of Johnstone Strait.

A more realistic earth model involves an elastic plate (lithosphere) of thickness  $H$  overlying a viscoelastic (Maxwell) substrate (asthenosphere). The locked portion of the main thrust zone is represented by a cut in the elastic plate extending to a depth  $d$ . The deformation during the seismic cycle for the model has been discussed by Thatcher and Rundle [1984]. I presume that the time-dependent strain rates (postseismic relaxation) associated with this model have died out in the Cascadia subduction zone, where it has been at least 150 years (length of the historic record) since a major interplate earthquake has occurred. Thus, the present deformation in central Vancouver Island is presumably the steady motion associated with strain accumulation. On that assumption, the uplift profiles for two elastic-viscoelastic earth models (Figure 5.1) have been calculated. Attention is confined to thin-lithosphere models because thick-lithosphere ( $d/H \ll 1$ ) models are essentially equivalent to the elastic half-space model ( $H = \infty$ ). The two models with  $H = 20$  km and  $H = 25$  km have uplift profiles that seem to bracket the observed uplift profile (Figure 5.1). (The uplift profiles were calculated using the approximate equations of Savage and Gu [1985] rather than the more precise formulation of Rundle [1982].) A smooth uplift profile is given by the model  $H = 20$  km, but the model  $H = 25$  km is of

interest because it produces horizontal strains closer to the observed value.

The fit of the elastic-viscoelastic models to the strain data is better for the  $H = 25$  km model than for the  $H = 20$  km model, contrary to the fit found for the uplift profile. For thin-lithosphere models the extension rate  $\dot{\epsilon}'_{22}$  is related to the uplift rate  $\dot{w}$  by

$$\dot{\epsilon}'_{22} = -(H/2)(\partial^2 \dot{w} / \partial y^2) \quad (5.1)$$

for steady motions (relaxed-asthenosphere solution) [Savage and Gu, 1985]. As can be seen from the uplift profile for the  $H = 20$  km model, the strain rate  $\dot{\epsilon}'_{22}$  will not only be very small landward of the coastline, but it will also be extension rather than contraction. Thus, the elastic-viscoelastic model  $H = 20$  km (rupture penetrating the entire lithosphere) does not furnish an appropriate fit to the observed strain rates. The strain-rate profile for the elastic-viscoelastic model with  $H = 25$  km is not shown, but it is very similar to the strain-rate profile for the elastic half-space (Figure 5.1).

The same model with a lower rate of convergence (20 mm/yr) can be used to estimate the deformation for a locked subduction zone between the Explorer and North American plates. The effect of variation in the rate of convergence along the plate margin, such indicated by Riddihough [1984] is not included in the two-dimensional model. In addition, no attempt is made to include the effect of possible three-plate interactions along the subducting Nootka fault zone. Convergence of the Explorer and North American plates is assumed to be normal to the plate boundary. The character of the uplift and strain accumulation curves shown in Figure 5.2 do not change with the lower convergence rate, but they are scaled down by the ratio of the convergence velocities (0.4). The maximum uplift rate would then be about 5 mm/yr for the elastic half-space model, and the maximum rate of contraction would be about  $0.2 \mu\text{strain}$ .

A similar model was presented by Lisowski and Savage [1986] for western Washington. They were able to roughly reproduce the landward tilting revealed by the sea-level changes

and level lines and the horizontal strain accumulation by locking the model fault to the coastline of the Olympic Peninsula. Their model is better constrained by a profile of the elevation change from level lines across the Olympic Peninsula. The elastic half-space model provided the best fit to the observed surface deformation, but it failed to reproduce the subsidence of the Puget Lowlands.

Summarizing, the elastic half-space model furnishes the best fit to the observed deformation data. The subduction models employed involve gross oversimplifications of the actual subduction process, and one should not conclude that the apparent better fit by the elastic half-space model implies that a thick lithosphere is involved in the Cascadia subduction. A better conclusion is that simple models of subduction offer a qualitative explanation of most of the features of the observed deformation, but the quantitative fit of those models to the observed deformation is not good.

A better understanding of how the elastic half-space model differs from the elastic-viscoelastic coupling model can be obtained by studying Figure 5.2. Shown are profiles of the total uplift experienced during the coseismic, postseismic, and background (relaxed-asthenosphere) stages of the earthquake cycle calculated using the approximate equations of *Savage and Gu* [1985]. The background uplift given for the elastic model ( $H = \infty$ ) is accumulated at a constant rate during the entire interseismic interval, whereas the total background uplift (relaxed asthenosphere) for the elastic-viscoelastic models represents the deformation that occurs after the post-seismic deformation has decayed to a very low level. The uplift profiles for the elastic model are compared with those from two extremes in the elastic-viscoelastic model; one with the depth of faulting extending halfway through the elastic plate ( $H = 2d$ ) and the other with the faulting breaking through the elastic plate ( $H = d$ ).

Coseismic uplift is the same in all models. The elastic model has no transient postseismic uplift and accumulated vertical strain during the interseismic interval is equal

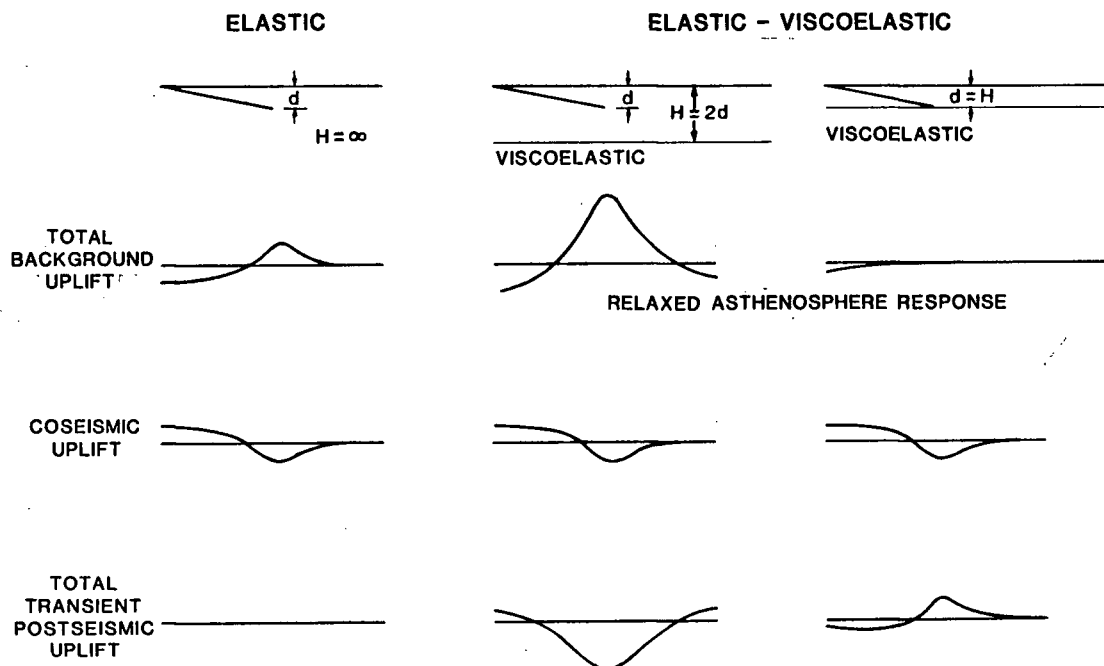


**Figure 5.2.** Model geometry and uplift profiles for three different subduction zone models. One represents the earth as an elastic half-space, and the other two use an elastic plate over a visco-elastic half-space. The portion of the main thrust zone subject to periodic slip events is indicated by the dipping line extending to a depth  $d$ . Profiles of the total uplift are given for the background (interseismic for the elastic half-space model; relaxed-asthenosphere response for the elastic-viscoelastic models), coseismic, and postseismic stages of the seismic cycle.

and opposite to the coseismic uplift. The interseismic vertical strain accumulation in the elastic-viscoelastic models depends on the depth of faulting relative to the thickness of the elastic plate ( $d/H$ ). For  $d = H/2$ , the stress locked into the elastic plate by the earthquake produces postseismic uplift in the same general sense as the coseismic. When these stresses are finally relaxed by flow in the asthenosphere ( $\approx 1$  to 100 years [Savage and Gu, 1985]), a relatively large amount of deformation is needed to reload the fault. In contrast, if the entire elastic plate is ruptured during the earthquake, flow in the asthenosphere causes postseismic uplift that reloads the fault (*i.e.*, uplift is the opposite of coseismic). The background uplift for this case is much smaller than that for the elastic model.

The profile of horizontal surface strain for the elastic half-space model is similar to

that given in Figure 5.1, whereas that for the elastic-viscoelastic models is approximated by the curvature of the uplift profile (equation 5.1). Little horizontal strain is indicated by the smooth uplift profile for  $d = H$ , whereas a relatively large amount of surface strain is indicated for  $d = H/2$ .

One feature is common to the background uplift in all of the models: the surface tilt on the portion of the profile up-dip of the base of the locked zone is away from the land. Profiles of elevation change across a suspected locked subduction zone may thus constrain the base of the locked segment of the main thrust zone. Another important observation is that surface deformation above a locked subduction zone late in the seismic cycle can be very small.



## 6. SUMMARY OF CONCLUSIONS

A 23-line trilateration network spanning a 30- by 50-km-wide area of central Vancouver Island was established in 1982 by the Geodetic Survey of Canada. The Gold River network extends over an area that is seismically active and tectonically complex. Distances were measured with a high-precision, electro-optical distance meter, and corrected for refractivity with aircraft-flown, temperature-humidity profiles and end-point air pressures. An error analysis based on calibration tests, manufacturer's specifications, and field comparison with a proven meteorological sensor system gave the standard error in a length  $L$  (m) measured with the GSC measurement system to be

$$\sigma(m) = \sqrt{(0.0067)^2 + (0.26 \times 10^{-6})^2 L^2}$$

or about 0.4 ppm in a 24-km-long distance. This estimate does not include possible error in the airspeed-dependent temperature correction.

A future resurvey of the Gold River network will provide the extensions ( $dL/L$ ), which can be used to calculate the three components of the incremental surface strain tensor. Assuming uniform strain and no systematic distance errors, the strain resolution at a one standard deviation level should be about 0.24  $\mu$ strain for the extensional components and 0.17  $\mu$ strain for the tensor shear.

A 1947 triangulation survey provided measurements to compute the historic surface deformation in Gold River area. Network adjustments and triangle closures indicated a standard error of about 2.3'' in a 1947 angle measurement. Several of the survey monuments occupied during the 1982 survey were common with the 1947 triangulation network, and other nearby 1947 monuments were tied into the 1982 trilateration network with angle and distance measurements. The angle changes between 1947 and 1982 were used to calculate the accumulated shear strain, with the standard error in an angle change estimated to be 2.4''. Between 1947 and 1982 the average rate of engineering shear

( $\gamma$ ) calculated from the change in 54 angles was  $0.23 \pm 0.12 \mu\text{rad/yr}$  with the axis of maximum contraction bearing  $N56^\circ E \pm 12^\circ$ . Within estimated measurement error the angle changes fit a uniform strain field. The pattern of strain accumulation within subsections of the network, however, appeared to vary systematically. To test if a few "bad" angles contaminated the average strain, the calculations were repeated with more restrictive data sets. In every case the modified data set indicated a the same or a higher average rate of shear strain accumulation and a better fit to a uniform strain field, but very little change in the orientation of the maximum compression axis. The average rate of shear strain accumulation in the Gold River network was shown to be similar to the 0.1 to 0.2  $\mu\text{rad/yr}$  average rates reported for Japan.

The orientation and average rate of strain accumulation in the Gold River network was found to be similar to that observed in geodetic networks in western Washington. The east-northeast maximum compressional strain in these networks was aligned with the direction of convergence between the Juan de Fuca and North American plates proposed by *Riddihough* [1984]. Compression in this direction could be the result a locked shallow interface between the subducting and overriding plates. Simple, two-dimensional models representing a locked subduction zone can roughly reproduce the observed deformation in central Vancouver Island and western Washington. The modeled deformation varied considerably depending upon details of the earth model: elastic half-space representations provided the best agreement with the observed surface deformation, but elastic-viscoelastic representations could account for inland subsidence. Free parameters in the elastic-viscoelastic model are not sufficiently constrained to produce useful results, but the large range of surface deformation that may result from a locked subduction zone was demonstrated.

The 1982 Gold River survey has extended studies of horizontal crustal deformation into central Vancouver Island. The careful measurements made by the Geodetic Survey of

Canada may someday yield information that will aid in determining the plate interactions responsible for the earthquakes of central Vancouver Island. Strain accumulation between 1947 and 1982 was not significant at the 95% confidence level. The hypothesis of a locked subduction zone was pursued because of the general agreement in pattern of strain accumulation along the coast, but this hypothesis is highly speculative given the uncertainty in the strain rates. Additional horizontal and vertical geodetic surveys are needed to define the pattern of surface deformation in central Vancouver Island. The simple, two-dimensional models for surface deformation are probably inadequate to describe the plate interactions in this area. The inconsistency between the east-northeast maximum compressional strain deduced from the geodetic networks and the north-south maximum compressional stress indicated by the earthquake focal mechanisms might be resolved by a three-dimensional model that accounts for interactions between the Pacific, Explorer, Juan de Fuca, and North America plates.

The first important steps in determining the pattern of contemporary surface deformation in central Vancouver Island have been detailed in this thesis: A high-precision strain network was established and the paleogeodetic deformation was examined.

## REFERENCES

- Adams, J., Active deformation of the Pacific Northwest continental margin, *Tectonics*, **3**, 449-472, 1984.
- Anderson, W.L., Weighted triangulation adjustment, *U.S. Geol. Sur. Open-file report Computer Contribution number 1*, U.S. Geological Survey Computer Center Division, Washington D.C., 52 pp, 1969.
- Ando, M., and E. I. Balazs, Geodetic evidence for aseismic subduction of the Juan de Fuca plate, *J. Geophys. Res.*, **84**, 3023-3028, 1979.
- Atwater, T., Implications of plate tectonics for the Cenozoic tectonic evolution of western North America, *Geol. Soc. Amer. Bull.*, **81**, 3513-3536, 1970.
- Berg, E., D. Harris, and C.A. Fisher, High precision single color laser distances, techniques and procedures to approach 0.3 ppM. Maui, Lanai, and Molokai network, *Hawaii Institute of Geophysics*, 209 pp, 1981.
- Bibby, H. M., Geodetically determined strain across the southern end of the Tonga-Kermadec-Hikurangi subduction zone, *Geophys. J. R. Astr. Soc.*, **66**, 513-533, 1981.
- Bibby, H. M., Unbiased estimate of strain from triangulation data using the method of simultaneous reduction, *Tectonophysics*, **82**, 161-174, 1982.
- Bomford, G., *Geodesy*, Oxford University Press, New York, 1980.
- Brunner, F. K., On the analysis of geodetic networks for the determination of the incremental strain tensor, *Surv. Rev.*, **25**, 56-67, 1979.
- Chandra, U., Seismicity, earthquake mechanisms, and tectonics along the western coast of North America from 42°N to 61°N, *Bull. Seism. Soc. Amer.*, **64**, 1529-1549, 1977.
- Chinnery, M.A., Deformation of the ground around surface faults, *Bull. Seismol. Soc. Amer.*, **51**, 355-372, 1961.
- Crossen, R.S., Small earthquakes, structure, and tectonics of the Puget Sound region, *Bull. Seismol. Soc. Am.*, **62**, 1133-1171, 1972.
- Crossen, R. S., Seismicity and tectonics of the Puget Sound region: results from the regional seismograph network, *Earthquake Notes*, **50**, 58-59, 1979.
- Crossen, R. S., Review of seismicity in the Puget Sound region from 1970 through 1979, *U.S. Geological Survey Open-file Report 83-19*, 6-18, 1983.
- Davies, J. N., and L. House, Aleutian subduction zone seismicity, volcano-trench separation, and their relation to great thrust-type earthquakes, *J. Geophys. Res.*, **84**, 4583-4591, 1979.
- Dept. of Energy, Mines, and Resources, Specifications and recommendations for control surveys and survey markers, *Survey and Mapping Branch misc. ser. 73/3*, 17 pp, 1973.

- Ellis et al., The Vancouver Island Seismic Project; a CO-CRUST onshore-offshore study of a convergent margin, *Can. Journ. Earth Sci.*, **20**, 719-741, 1983.
- Federal Geodetic Control Committee, *Classification, standards of accuracy, and general specifications of geodetic control surveys*, U.S. Dept. of Commerce, Maryland, 1980.
- Frank, F. C., Deduction of earth strains from survey data, *Bull. Seism. Soc. Am.*, **56**, 35-42, 1966.
- Fukao, Y., Tsunami earthquakes and subduction processes near deep-sea trenches, *J. Geophys. Res.*, **84**, 2303-2314, 1979.
- Greene, J.R., Accuracy evaluation in electro-optic distance measuring instruments, *Surveying and Mapping*, **37**, 247-256, 1977.
- Gutenberg, B., and C.F. Richter, *Seismicity of the Earth and Associated Phenomena*, 2<sup>nd</sup> ed., Princeton University Press, Princeton, N.J., 1954.
- Heaton, T. H., and H. Kanamori, Seismic potential associated with subduction in the northwestern United States, *Bull. Seism. Soc. Am.*, **74**, 933-941, 1984.
- Hilton, W.F., Thermal effects on bodies in an airstream, *Proc. Roy. Soc. London, Ser. A*, **168**, 43-56, 1938.
- Holdahl, S. R., and R. L. Hardy, Solvability and multiquadric analysis as applied to investigations of vertical crustal movements, *Tectonophysics*, **52**, 139-156, 1979.
- Hyndman, R. D., R. P. Riddihough, and P. Herzer, The Nootka fault zone—A new plate boundary off western Canada, *Geophys. J. R. Astron. Soc.*, **58**, 667-683, 1979.
- Hyndman, R. D., and D. H. Weichert, Seismicity and rates of relative motion on the plate boundaries of western North America, *Geophys. J. R. Astr. Soc.*, **72**, 59-82, 1983.
- Keen, C. E., and R. D. Hyndman, Geophysical review of the continental margins of eastern and western Canada, *Can. J. Earth Sci.*, **16**, 712-747, 1979.
- Langston, C. A., and D. E. Blum, The April 29, 1965 Puget Sound earthquake and the crustal and upper mantle structure of western Washington, *Bull. Seismol. Soc. Am.*, **67**, 693-711, 1977.
- Laurila, S.M., *Electronic Surveying and Navigation*, John Wiley & Sons, New York, 1976.
- Lay, T., H. Kanamori, and L. Ruff, The asperity model and the nature of large subduction zone earthquakes, in *Earthquake Prediction Research*, Terra Scientific Publishing Co., Tokyo, Japan, 3-71, 1982.
- Lisowski, M. and J.C. Savage, Strain accumulation in western Washington, manuscript, 1986.
- Lisowski, M., and W.F. Slawson, Horizontal strain network established near Gold River, Vancouver Island, *Program with Abstracts G.A.C., M.A.C., and C.G.U. Joint Annual Meeting*, Victoria, B.C., A43, 1983.

- Lisowski, M., and W.F. Slawson, Strain accumulation in Vancouver Island and Washington, Program with Abstracts Pacific Northwest Regional Meeting of the A.G.U., Western Washington University, 1983.
- Menard, H.W., Fragmentation of the Farallon plate by pivoting subduction, *J. Geol.*, **86**, 1978.
- Milne, W.G., G.C. Rogers, R.P. Riddihough, G.A. MacMechan, and R.D. Hyndman, Seismicity of western Canada, *Can. J. Earth Sci.*, **15**, 1170-1192, 1978.
- Minster, J.B., and T.H. Jordan, Present-day plate motions, *J. Geophys. Res.*, **83**, 5331-5334, 1978.
- Mura, T., The continuum theory of dislocations, *Adv. Mater. Res.*, **3**, 1-108, 1968.
- Nakane, K., Horizontal tectonic strain in Japan (II), *J. Geodetic Soc. Japan*, **19**, 200-208, 1973.
- Nishimura, C., D. S. Wilson, and R. N. Hey, Pole of rotation analysis of present-day Juan de Fuca plate motion, *J. Geophys. Res.*, **89**, 10283-10290, 1984.
- Omega Engineering, 1984 Complete Temperature Handbook and Encyclopedia , Omega Engineering Inc., Samford Ct., 1984.
- Owens, J.C. Optical refractive index of air: dependence on pressure, temperature and composition, *Appl. Opt.*, **6**, 51-59, 1967.
- Peterson, E.T., and T. Seno, Factors affecting seismic moment release rates in subduction zones, *J. Geophys. Res.*, **89**, 10,233-10,248, 1984.
- Prescott, W. H., An extension of Frank's method for obtaining crustal shear strains from survey data, *Bull. Seism. Soc. Am.*, **66**, 1847-1853, 1976.
- Prescott, W. H., J. C. Savage, and W. T. Kinoshita, Strain accumulation rates in the western United states between 1970 and 1978, *J. Geophys. Res.*, **84**, 5423-5435, 1979.
- Reid, H.F., Permanent displacements of the ground in the California earthquake of April 18, 1906, in *Report of the State Earthquake Investigation Commission*, vol. 2, 16-28, Carnegie Institution of Washington, Washington, D.C., 1910.
- Reilinger, R. E., and J. Adams, Geodetic evidence for active landward tilting of the Oregon and Washington coastal ranges, *Geophys. Res. Lett.*, **9**, 401-403, 1982.
- Reyners, M., A microearthquake study of the plate boundary, North Island, New Zealand, *Geophys. J. R. Astron. Soc.*, **63**, 1-22, 1980.
- Riddihough, R. P., A model for recent plate interactions off Canada's west coast, *Can. J. Earth Sci.*, **14**, 384-396, 1977.
- Riddihough, R. P., Contemporary vertical movements and tectonics on Canada's west coast: A discussion, *Tectonophysics*, **86**, 319-341, 1982.

- Riddihough, R. P., Recent movements of the Juan de Fuca plate system, *J. Geophys. Res.*, **89**, 6980-6994, 1984.
- Riddihough, R. P., M. E. Beck, R. L. Chase, E. E. Davis, R. D. Hyndman, S. H. Johnson, and G. C. Rogers, Geodynamics of the Juan de Fuca plate in "Geodynamics of the eastern Pacific region, Caribbean and Scotia Arcs," edited by Ramon Cabre, S. J., *Geodynamics Series*, **9**, Amer. Geophys. Union, 5-21, 1983.
- Riddihough, R. P., and R. D. Hyndman, Canada's active western margin: the case for subduction, *Geoscience Canada*, **3**, 269-278, 1976.
- Rikitake, T., Earthquake forecasting and warning, D. Reidel Publishing Company, Boston, 1982.
- Rinner, K., Distance measurements with the aid of electromagnetic waves, *Geophys. Surveys*, **1**, 459-479, 1974.
- Rogers, G. C., Earthquake fault plane solutions near Vancouver Island, *Can. J. Earth Sci.*, **16**, 523-531, 1979.
- Rogers, G. C., Some comments on the seismicity of the northern Puget Sound southern Vancouver Island region, *U.S. Geol. Surv. Open-File Rep.*, **83 19**, 19-39, 1983a.
- Rogers, G.C., Seismotectonics of British Columbia, Ph.D. Thesis, Univ. of British Columbia, 1983b.
- Rogers, G.C., and H.S. Hasegawa, A second look at the British Columbia earthquake of June 23, 1946, *Seismol. Soc. Am. Bull.*, **68**, 653-675, 1978.
- Rundle, J. B., Viscoelastic-gravitational deformation by a rectangular thrust fault in a layered earth, *J. Geophys. Res.*, **87**, 7787-7796, 1982.
- Savage, J. C., A dislocation model of strain accumulation and release at a subduction zone, *J. Geophys. Res.*, **88**, 4984-4996, 1983a.
- Savage, J. C., Strain accumulation in western United states, *Ann. Rev. Earth Planet. Sci.*, **11**, 11-43, 1983b.
- Savage, J. C., and Gu Guohua, A plate-flexure approximation to postseismic and interseismic deformation, *submitted to J. Geophys. Res.*, 1985.
- Savage, J. C., M. Lisowski, and W. H. Prescott, Geodetic strain measurements in Washington, *J. Geophys. Res.*, **86**, 4929-4940, 1981.
- Savage, J. C., and W. H. Prescott, Precision of Geodolite distance measurements for determining fault movements, *J. Geophys. Res.*, **78**, 6001-6008, 1973.
- Savage, J.C., W.H. Prescott, M. Lisowski, and N. King, Strain accumulation in southern California, 1973-1980, *J. Geophys. Res.*, **86**, 6991-7001, 1981.
- Sbar, M. L., An explanation for contradictory geodetic strain and fault plane solution data in western North America, *Geophys. Res. Lett.*, **10**, 177-180, 1983.

- Slawson, W. F., and J. C. Savage, Geodetic deformation associated with the 1946 Vancouver Island, Canada, earthquake, *Bull. Seismol. Soc. Am.*, **69**, 1487-1496, 1979.
- Snively, P. D., Jr., and H. C. Wagner, Geologic cross section across the continental margin off Cape Flattery, Washington and Vancouver Island, B.C., *U.S. Geological Survey Open-file Report 81-978*, 5 p., 1981.
- Stickney, T.M., M.W. Shedlov, D.I. Thompson, F.T. Yakos, Rosemount total temperature sensors, *Technical Report 5755 Revision A*, Rosemount Inc, Minnesota, 1981.
- Taber, J. J., and S. W. Smith, Seismicity of the Cascadia subduction zone, Olympic Peninsula, Washington, *submitted to Bull. Seism. Soc. Am.*, 1984.
- Thatcher, W., Crustal deformation studies and earthquake prediction, *Earthquake Prediction - an International Review*, Maurice Ewing Series, A.G.U., 394-410, 1981.
- Thatcher, W., Nonlinear strain buildup and the earthquake cycle on the San Andreas fault, *J. Geophys. Res.*, **88**, 5893-5902, 1983.
- Thatcher, W., and J. B. Rundle, A viscoelastic coupling model for the cyclic deformation due to periodically repeated earthquakes at subduction zones, *J. Geophys. Res.*, **89**, 7631-7640, 1984.
- Tiffin, D.L., Cameron, B.E.B., and J.W. Murray, Tectonic and depositional history of the continental margin off Vancouver Island, B.C., *Can. J. Earth Sci.*, **9**, 280-296, 1972.
- Tobin, P.G., and L.R. Sykes, Seismicity and tectonics of the northeast Pacific Ocean, *Geophys. Res.*, **73**, 3821-3846, 1968.
- Trenkle F. and M. Reinhart, In-flight temperature measurements, in Volume 2 of *AGARD Flight Test Instrument Series*, AGARD-AG-160-Vol 2, 1973.
- Weaver, C. S., and S. W. Smith, Regional tectonic hazard implications of a crustal fault zone in southwestern Washington, *J. Geophys. Res.*, **88**, 10371-10383, 1983.
- Welsch, W., A review of the adjustment of free networks, *Survey Review*, **XXV**, 167-180, 1979.
- Yelin, T. S., The Cascadia and other Pacific-rim subduction zones: A seismologic comparison, *submitted to Tectonics*, 1984.
- Yonekura, N., and K. Shimizaki, Uplifted marine terraces and seismic crustal deformation in arc-trench systems: a role of imbricated thrust faulting (abstract), *EOS Trans. Am. Geophys. Un.*, **61**, 1111, 1980.



## Appendix A General theory of EDM measurements

Some of the rudimentary concepts of an electronic distance meter (EDM) measurement are explained, the scale correction to a measured length due to atmospheric conditions is discussed, and the form of the equation for the group refractive index is expressed.

The EDM transmits an intensity modulated laser beam that is returned to the instrument by retro-reflector prisms. The returned signal is focused on a photo-detector by the receiving telescope. Comparison of the outgoing and incoming modulations gives the phase shift, or delay due to the transit time for the two-way path between the instrument and retro-reflector. This shift varies with the distance of the two-way travel path and the modulation length. Thus, the distance  $L$  is resolved into an unknown number of whole modulation lengths,  $M$ , plus a known fractional modulation length

$$L = \frac{1}{2} \left( M + \frac{\theta}{2\pi} \right) \lambda_m \quad (A.1)$$

where  $\theta/2\pi$  is the phase shift, and  $\lambda_m$  is the modulation length. Moving the reflector 1 m toward the instrument will shorten the path length by 2 m. The two-way travel path makes the effective modulation length equal to  $\frac{1}{2}$  wavelength.

The modulation length is equal to the ratio of the group velocity,  $v_g$ , with which the modulation is transmitted to the modulation frequency,  $f_m$ .

$$\lambda_m = \frac{v_g}{f_m} \quad (A.2)$$

The group velocity of the modulated light varies with the average group refractive index of the air it passes through  $n_{GA}$

$$v_g = \frac{c}{n_{GA}} \quad (A.3)$$

where  $c$  is the velocity of light in a vacuum.

Accurate formulae for the group refractive index of air as a function of composition, pressure, temperature, water vapor pressure, and carrier wavelength are known [Owens, 1967].

Distance measurements are actually made using a nominal modulation wavelength  $\lambda_n$  and later corrected for the difference between the nominal refractive index,  $n_{GN}$ , and the measured value,  $n_{GA}$ . The modulation wavelength is expressed as

$$\lambda_m = \lambda_n \left( \frac{n_{GN}}{n_{GA}} \right) \quad (A.4)$$

where the nominal modulation length  $\lambda_n$  is found by

$$\lambda_n = \frac{c}{f_m n_{GN}} \quad (A.5)$$

Fixing the nominal wavelength to a whole number distance, *e.g.*,  $\lambda_n = 20$  m, specifying a nominal refractive index,  $n_{GN} = 1.000310$ , and using  $c = 299,792.5$  km/s yields a nominal modulation frequency of 14,984,979.7 Hz. Substituting for  $\lambda_m$  in (A.1) from (A.4) gives

$$L = \frac{1}{2} \left[ \left( M + \frac{\theta}{2\pi} \lambda_n \right) \frac{n_{GN}}{n_{GA}} \right] \quad (A.6)$$

Resolving the length ambiguity by using several different and well-chosen nominal modulation lengths we can write

$$L = L_m \left( \frac{n_{GN}}{n_{GA}} \right) \quad (A.7)$$

where  $L_m$  is the measured length.

The ratio of the nominal refractive index to the measured refractive index is the refractive index scale correction to a distance measurement. This scale correction is generally much less than the shortest modulation length and not important in the coarse

distance calculation. An additional scale correction may be necessary if the modulation frequency drifts from the nominal value. This correction is merely the ratio of the nominal modulation frequency to the actual modulation frequency.

Only the refractive index of the air remains to be determined. The *Owens'* [1967] formula for the group refractive index of air is of the form

$$n_{GA} = 1 + R_s D_s + R_w D_w \quad (A.8)$$

where  $R_s$  and  $R_w$  are constants dependent on the carrier wavelength in a vacuum (For the Rangemaster IH the carrier wavelength is  $0.6328 \mu\text{m}$  and  $R_s = 8087.6$  and  $R_w = 6909.7$ ).  $D_s$  is the density factor of dry air containing 0.03%  $\text{CO}_2$  of temperature  $T$  (K) and with partial pressure  $P_s$  (mb)

$$D_s = \frac{P_s}{T} \left[ 1 + P_s \left( 57.90 \times 10^{-8} - \frac{9.3250 \times 10^{-4}}{T} + \frac{0.25844}{T^2} \right) \right] \quad (A.9)$$

and  $D_w$  is the density factor of moist air at temperature  $T$  with partial pressure  $P_w$  (mb)

$$D_w = \frac{P_w}{T} \left\{ 1 + P_w \left[ 1 + (3.7 \times 10^{-4}) P_w \right] \left[ -2.37321 \times 10^{-3} + \frac{2.23366}{T} - \frac{710.792}{T^2} + \frac{7.75141 \times 10^4}{T^3} \right] \right\} \quad (A.10)$$

Ignoring factors such as the curvature of the light path and additive constants, the accuracy of a distance measurement depends on the stability of the modulation frequency and the accuracy of the average refractive index. The sensitivity of the atmospheric parameters  $T$ ,  $P_s$ , and  $P_w$  is investigated by differentiating a simplified and slightly less precise form of equation (A.8) given by *Laurila* [1976]

$$N = \frac{N_g P_s - 41.8 P_w}{3.709 T} \quad (A.11)$$

where  $N = (1 - n_{GA}) \times 10^6$ ,  $N_g = (1 - n_{GN}) \times 10^6$ ,  $P_s$  is the partial pressure of dry air (mb),  $P_w$  the water vapor pressure (mb), and  $T$  the temperature (K).

The partial derivatives are

$$\begin{aligned} dN_T &= \frac{1}{T^2} \left( -\frac{N_g}{3.709} P_s + \frac{41.8}{3.709} P_w \right) dT \\ dN_{P_s} &= \frac{N_g}{3.709T} dP_s \\ dN_{P_w} &= -\frac{41.8}{3.709T} dP_w \end{aligned} \tag{A.12}$$

About a 1 ppm increase in length is produced by any of the following:

- a 1°C increase in the average temperature;
- a 0.34 kPa decrease in the average pressure (equivalent to a 3.4 mb, 2.5 mm, or 0.1 in decrease);
- at 20°C a 100% increase in the relative humidity or
- at 35°C a 50% increase in the relative humidity.

With oven-controlled, quartz-crystal oscillators stable to about 0.1 ppm, the principal limitation to the accuracy of a distance measurement is the uncertainty of the average temperature, pressure, and humidity of the air along the path.

## Appendix B Calculation of the average index of refraction

The following quantities are known prior to beginning the calculation:

- $n$  – the number of temperature and humidity readings recorded in a profile.
- $t_i$  –  $i=1,2,3,\dots,n$  temperature readings (K), corrected for airspeed.
- $e_i$  –  $i=1,2,3,\dots,n$  water vapor pressure readings (mb) calculated from the humidity, temperature, and the total air pressure.
- $P_1$  – the total air pressure (mb) at the instrument station.
- $h_1$  – the elevation (m) of the instrument station.
- $h_n$  – the elevation (m) of the reflector station.
- $L$  – the approximate slope distance (m) between the instrument and the reflector station.
- $\lambda$  – the latitude of the instrument station.

### An outline of the procedure

The  $n$  temperature and humidity readings recorded in a profile define  $n-1$  segments.

1. Calculate the elevation increment for a segment from the assumed curvature of the path, the curvature of the earth, the approximate slope distance, and the station elevations.
2. Find the mean temperature and water vapor pressure for each segment.
3. Use the total pressure at the beginning of the segment, the mean temperature and water vapor pressure within the segment, and the elevation increment to calculate the total pressure at the end of the segment. Then find the mean total pressure for the segment.
4. Calculate the index of refraction for the segment from the mean temperature, vapor pressure, and the total pressure.
5. Repeat the above steps for each of the  $n - 1$  segments.

6. Average all of the segment indices of refraction.

### Formulation

The formulation is divided into steps as defined in the procedural outline.

Step 1. For a path of length  $L$  with radius of curvature  $\sigma$  and divided into  $n - 1$  segments, the  $j^{th}$  elevation increment  $\Delta h_j$  is derived from the geometric relationships shown in Figure B.1.

Assume  $\sigma = R/2k$ , where  $R$  is the approximate radius of the earth and  $k = 0.07$ , an average value for the coefficient of refraction (see *Bomford* [1980], Table 1.1, or for a more precise value of  $\sigma$  use his formula 3.47).

The angle  $\Theta$  subtended by the arc  $L$  is  $L/\sigma$  and for small  $\Theta$  the length of the cord  $C \approx L$ .

We seek  $a$ , the distance from  $O_c$  to  $O_e$ , that is, the distance from the center of the radius of curvature of the path to the center of the earth. In addition, we need  $\phi$ , the angle at  $O_c$  between the instrument station and  $O_e$ .

Let  $R_1 = R + h_1$  and  $R_2 = R + h_n$ .

To find  $a$  and  $\phi$  we first use the law of cosines to calculate  $\zeta$ , the angle at the instrument station between rays to the reflector station and the center of the earth. That is

$$\zeta = \arccos \left( \frac{R_1^2 - R_2^2 + L^2}{2LR_1} \right) \quad (B.1)$$

The equal angles in a isocles triangle are formed by  $\zeta + \beta$  with the third angle being  $\Theta$  and  $2(\zeta + \beta) + \Theta = \pi$ , then

$$\beta = \frac{\pi - 2\zeta - \Theta}{2} \quad (B.2)$$

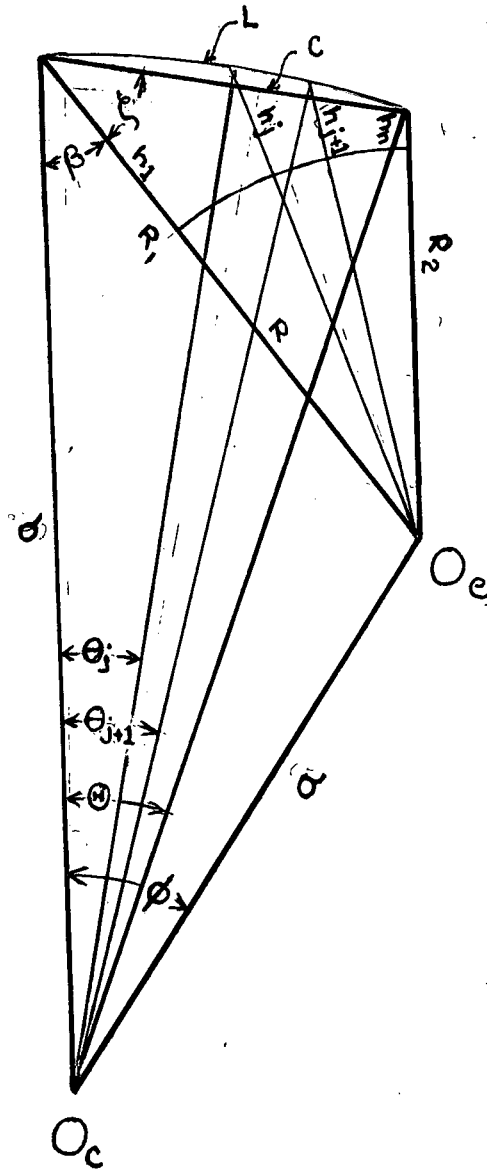


**Figure B.1.** Distances and angles used in to determine the average pressure from end-point pressure readings and a profile of the temperature and humidity along the measured length  $L$ .

The distance  $a$  from  $O_c$  to  $O_e$  is then calculated with the law of cosines in the triangle  $O_c-O_e-IS$

$$a = \sqrt{R_1^2 + \sigma^2 - 2R_1\sigma \cos \beta} \quad (B.3)$$

and  $\phi$  is calculated with the law of sines

$$\phi = \arcsin \left( \frac{R_1 \sin \beta}{a} \right) \quad (B.4)$$

Step 1a. For a path divided into  $n - 1$  arc segments,  $\theta_j$ , the angle at the center of the radius of curvature between rays to the instrument station and the end of the  $j^{th}$  segment is

$$\theta_j = \Theta \frac{j}{n-1} \quad n > 1 \quad (B.5)$$

The distance from the center of the earth to the end of the  $j^{th}$  segment,  $R + h_{j+1}$ , is calculated with the law of cosines

$$R + h_{j+1} = \sqrt{\sigma^2 + a^2 - 2\sigma a \cos(\phi - \theta_j)} \quad (B.6)$$

and the  $j^{th}$  elevation increment is

$$\Delta h_j = h_{j+1} - h_j \quad (B.7)$$

where  $h_1$  is the elevation of the instrument station, and  $h_n$  is the elevation of the reflector station.

Step 2. The mean temperature and water vapor pressure for the  $j^{th}$  segment is

$$\bar{t}_j = \frac{t_j + t_{j+1}}{2} \quad \text{and} \quad \bar{e}_j = \frac{e_j + e_{j+1}}{2} \quad (B.8)$$



Step 3. To find the mean total pressure for the  $j^{th}$  segment, given the total pressure at the beginning of the segment,  $P_j$ , we calculate the pressure at the end of the segment and then take the mean. The increment of pressure within the segment is  $\Delta P = \rho g \Delta h$ . The pressure at the end of the segment is

$$P_{j+1} = P_j \exp(\sum \rho_j g_j \Delta h_j) \quad (B.9)$$

where  $\Delta h_j$ , the elevation change within the  $j^{th}$  segment is given by Step 1, and  $\rho_j$ , the average density of the air within the  $j^{th}$  layer, defined by the elevation change is found using

$$\rho_j = \frac{Ds_j}{\bar{t}_j} \left[ 1 - \left( 1 - 216.582 \times 10^{-6} \frac{Dw_j}{Ds_j} \right) \frac{\bar{e}_j}{P_j} \right] \quad (B.10)$$

where  $Ds_j$  and  $Dw_j$  are the density factors for dry air and for water vapor within the segment from the following formula by *Owens* [1967]

$$Ds_j = \left( P_j - \frac{\bar{e}_j}{\bar{t}_j} \right) \left[ 1 + (P_j - \bar{e}_j) \left( 57.98 \times 10^8 - \frac{9.32 \times 10^{-4}}{\bar{t}_j} + \frac{0.25844}{\bar{t}_j^2} \right) \right] \quad (B.11)$$

$$Dw_j = \frac{\bar{e}_j}{\bar{t}_j} \left\{ 1 + \bar{e}_j \left[ 1 + 3.7 \times 10^{-4} \left( \frac{-2.23366 \times 10^8}{\bar{t}_j} - \frac{710.792}{\bar{t}_j^2} + \frac{7.75141 \times 10^4}{\bar{t}_j^3} \right) \right] \right\}$$

The mean gravity  $\bar{g}_j$  within a segment is

$$\bar{g}_j = \frac{g_j + g_{j+1}}{2} \quad (B.13)$$

where

$$g_{j+1} = g_j - 3.086 \times 10^{-8} \Delta h_j \quad (B.14)$$

with  $g_1$  being the gravity at the instrument station caculated from the latitude of the station with the International gravity formula and corrected for the elevation of the station,  $EI$ . That is

$$g_1 = 980.616 - 2.5928 \cos(2\lambda) + 0.0069 \cos^2(2\lambda) - 3.086 \times 10^{-8} h_1 \quad (B.14)$$

The mean total pressure,  $\bar{P}_j$ , is then

$$\bar{P}_j = \frac{P_j + P_{j+1}}{2}$$

Step 4. With the mean pressure, temperature, and water vapor pressure the group refractive index  $nG_j$  for the segment is calculated using *Owens'* [1967] formulation

$$(nG_j - 1) \times 10^8 = RsDs_j + RwDw_j \quad (B.17)$$

where  $Rs$  and  $Rw$  are constants that depend on the carrier wavelength (for a helium-neon laser with a wavelength of 0.6328,  $\mu\text{m}$ ,  $Rs = 8087.6$  and  $Rw = 6909.7$ ).  $Ds_j$  and  $Dw_j$  are the density factors for dry air and water vapor as used in Step 3, but here the mean total pressure,  $\bar{P}_j$ , is used in place of  $P_j$  in the calculation for  $Ds_j$ . That is

$$Ds_j = \left( \bar{P}_j - \frac{\bar{e}_j}{\bar{t}_j} \right) \left[ 1 + (PM_j - \bar{e}_j) \left( 57.98 \times 10^8 - \frac{9.32 \times 10^{-4}}{\bar{t}_j} + \frac{0.25844}{\bar{t}_j^2} \right) \right]$$

Step 5. The segment refractive index is added to the sum of the previous values,  $j$  is incremented, and Steps 1a through 5 are repeated until  $j = n - 1$ .

Step 6. The average refractive index  $nG$  is

$$nG = \frac{\sum nG_j}{n - 1} \quad (B.19)$$

- Lisowski, M., Prescott, W. H., and Savage, J. C., 1979, Geodetic tilt observed near the epicenter of the Saint Elias, Alaska, earthquake of February 28, 1979: Bulletin of the Seismological Society of America, v. 69, p. 2121-2123.
- Lisowski, M., and Savage, J. C., 1979, Strain accumulation from 1964 to 1977 near the epicentral zone of the 1976-1977 earthquake swarm southeast of Palmdale, California: Bulletin of the Seismological Society of America, v. 69, p. 751-756.
- Lisowski, M., and Thatcher, W., 1981, Geodetic determination of horizontal deformation associated with the Guatemala earthquake of February 4, 1976: Bulletin of the Seismological Society of America, v. 71, p. 845-856.
- Lisowski, M., and Prescott, W. H., 1981, Short range distance measurements along the San Andreas fault system in Central California 1976 to 1979: Bulletin of the Seismological Society of America, v. 71, p. 1607-1624.
- Lisowski, M., and Burford, R. O., 1986, Horizontal deformation across the Fairweather fault near Yakutat, Alaska, from geodetic surveys in 1967 and 1983, submitted to Journ. Geophys. Res.